Aus der Klinik für Radiologie
der Medizinischen Fakultät Charité – Universitätsmedizin Berlin

DISSERTATION

Development of multifrequency magnetic resonance elastography for biophysical property quantification of human brain tissue

Entwicklung der multifrequenten Magnetresonanz-Elastographie zur Quantifizierung der biophysikalischen Eigenschaften von menschlichem Hirngewebe

zur Erlangung des akademischen Grades
Doctor of Philosophy (PhD)

vorgelegt der Medizinischen Fakultät
Charité – Universitätsmedizin Berlin

von

Helge Herthum

Datum der Promotion: 03.03.2023

Table of contents

List of tables

List of figures

List of abbreviations

1D	One-dimensional
2D	Two-dimensional
3D	Three-dimensional
BH-ex	Expiration and breath-hold
BH-in	Deep inspiration and breath-hold
CBF	Cerebral blood flow
CV	Coefficient of variation
CSF	Cerebrospinal fluid
dSNR	Displacement SNR
ECM	Extracellular matrix
EPI	Spin-echo echo-planar imaging
FDO	Finite difference operator
FEM	Finite element method
FFT	Fast Fourier transformation
FLAIR	Fluid attenuation inversion recovery
FWHM	Full width at half maximum
IA MRE	Intrinsic activated MRE
ICP	Intracranial pressure
ISMRM	International Society for Magnetic Resonance in Medicine
k-MDEV	Wavenumber-based multi-frequency dual elasto-visco inversion
LMM	Linear mixed-effects model
MDEV	Multi-frequency dual elasto-visco inversion
MEG	Motion-encoding gradient
MRE	Magnetic resonance elastography
MRI	Magnetic resonance imaging
MS	Multiple sclerosis
NAWM	Normal-appearing white matter
ROI	Region of interest
RRMS	Relapsing-remitting multiple sclerosis
rtMRE	Real-time magnetic resonance elastography
SNR	Signal to noise ratio
ssMRE	Steady-state magnetic resonance elastography
SWS	Shear wave speed
VM	Valsalva maneuver
WM	White matter

Abstract

Magnetic resonance elastography (MRE) is an emerging technique for the quantitative imaging of the biophysical properties of soft tissues in humans. Following its successful clinical application in detecting and characterizing liver fibrosis, the scientific community is investigating the use of viscoelasticity as a biomarker for neurological diseases. Clinical implementation requires a thorough understanding of brain tissue mechanics in conjunction with innovative techniques in new research areas. Therefore, three in vivo studies were conducted to analyze the inherent stiffness dispersion of brain tissue over a wide frequency range, to investigate real-time MRE in monitoring the viscoelastic response of brain tissue during the Valsalva maneuver (VM), and to study mechanical alterations of small lesions in multiple sclerosis (MS).

Ultra-low frequency MRE with profile-based wave analysis was developed in 14 healthy subjects to determine large-scale brain stiffness, from pulsation-induced shear waves (1 Hz) to ultra-low frequencies (5 – 10 Hz) to the conventional range (20 – 40 Hz). Furthermore, multifrequency real-time MRE with a frame rate of 5.4 Hz was introduced to analyze stiffness and fluidity changes in response to respiratory challenges and cerebral autoregulation in 17 healthy subjects. 2D and 3D wavenumber-based stiffness reconstruction of the brain was established for conventional MRE in 12 MS patients. MS lesions were analyzed in terms of mechanical contrast with surrounding tissue in relation to white matter (WM) heterogeneity.

We found superviscous properties of brain tissue at large scales with a strong stiffness dispersion and a relatively high model-based viscosity of $\eta = 6.6 \pm 0.3$ Pa·s. The brain's viscoelasticity was affected by perfusion changes during VM, which was associated with an increase in brain stiffness of 6.7% ± 4.1% ($p<.001$), whereas fluidity decreased by -2.1 ± 1.4% ($p<.001$). In the diseased brain, the analysis of 147 MS lesions revealed 46% of lesions to be softer and 54% of lesions to be stiffer than surrounding tissue. However, due to the heterogeneity of WM stiffness, the results provide no significant evidence for a systematic pattern of mechanical variations in MS. Nevertheless, the results may explain, for the first time, the gap between static ex vivo and dynamic in vivo methods. Fluidity-induced dispersion provides rich information on the structure of tissue compartments. Moreover, viscoelasticity is affected by perfusion during cerebral autoregulation and thus may be sensitive to intracranial pressure modulation. The overall heterogeneity of stiffness obscures changes in MS lesions, and MS may not exhibit sclerosis as a mechanical signature.

In summary, this thesis contributes to the field of human brain MRE by presenting new methods developed in studies conducted in new research areas using state-of-the-art technology. The results advance clinical applications and open exciting possibilities for future in vivo studies of human brain tissue.

Zusammenfassung

Die Magnetresonanz-Elastographie (MRE) ist ein Verfahren zur quantitativen Darstellung der viskoelastischen Eigenschaften von Weichgewebe. Nach der erfolgreichen klinischen Anwendung in der Leberdiagnostik wird versucht, Viskoelastizität als Biomarker für neurologische Krankheiten zu nutzen. Hierzu bedarf es einer genauen Analyse der Gewebemechanik und innovativen Anwendungsgebieten. Daher, wurden drei Studien durchgeführt, um die Steifigkeitsdispersion von Hirngewebe zu analysieren, das viskoelastische Verhalten während des Valsalva Manövers (VM) abzubilden, und die mechanischen Veränderungen in Läsionen bei Multipler Sklerose (MS) zu untersuchen.

Niedrigfrequenz-MRE mit profilbasierter Wellenanalyse wurde in 14 Probanden entwickelt, um die Steifigkeit des Gesamthirns von pulsationsinduzierten Scherwellen (1 Hz) über ultraniedrige Frequenzen (5 – 10 Hz) bis hin zum konventionellen Bereich (20 – 40 Hz) zu bestimmen. Außerdem wurde die multifrequente Echtzeit-MRE mit einer Bildfrequenz von 6.4 Hz eingeführt, um die viskoelastische Antwort des Gehirns auf respiratorische Herausforderungen bei 17 gesunden Probanden zu untersuchen. Neue 2D- und 3D-Wellenzahl-basierte Steifigkeitsrekonstruktionen für das Gehirn wurden in 12 MS Patienten und konventioneller MRE entwickelt. Die Steifigkeitsänderungen in MS-Läsionen wurden mit umliegender weißer Substanz und dessen Heterogenität verglichen.

Wir fanden superviskose Eigenschaften des Hirngewebes mit einer starken Dispersion und relativ hohen, modellbasierten Viskosität von η = 6,6 ± 0,3 Pa·s. Die mechanischen Gewebeeigenschaften wurden durch Perfusionsänderungen während VM beeinflusst und die Hirnsteifigkeit erhöhte sich um 6,7 ± 4,1% ($p<.001$) wobei sich die Fluidität um -2,1 ± 1,4% ($p<.001$) verringerte. Die Analyse von 147 MS-Läsionen ergab, dass 54% bzw. 46% der Läsionen steifer bzw. weicher sind als das umgebende Gewebe. Aufgrund der Heterogenität der WM-Steifigkeit konnte jedoch kein Hinweis auf ein systematisches Muster mechanischer Veränderungen in MS-Läsionen gefunden werden.

Die Ergebnisse können zum ersten Mal die Lücke zwischen statischen ex vivo und dynamischen in vivo Methoden erklären. Die fluiditätsinduzierte Dispersion liefert interessante Informationen über die zugrundeliegende Gewebestruktur. Darüber hinaus wird die Viskoelastizität durch die Perfusion während der zerebralen Autoregulation beeinflusst und kann daher empfindlich auf intrakranielle Druckschwankungen reagieren. Die allgemeine Heterogenität der Steifigkeit überschattet die Veränderungen in MS-Läsionen, und somit ist Sklerose möglicherweise kein prominentes Merkmal von MS. Zusammenfassend lässt sich festhalten, dass diese Dissertation einen Beitrag zum Gebiet der MRE leistet, indem neue Methoden und Anwendungen in neuen Forschungsgebieten mit modernster Technologie dargestellt werden. Hierdurch wird die klinische Translation gefördert und spannende Möglichkeiten für zukünftige Studien eröffnet.

1 Introduction

1.1 Why soft tissue mechanics matters

The in vivo mechanical properties of biological soft tissues are defined by their basic structure. Physical quantification has long been of interest to the scientific community.[1] The complex architecture of soft tissues determines the environment in which cells live, and as such influences their proliferation and homeostasis as studied in the field of mechanobiology.[2,3] The theory of biomechanics describes, among other things, how living tissue reacts and deforms when exposed to forces. In general, biological tissues are characterized by viscoelastic behavior, meaning that they have properties of an elastic solid and a viscous fluid.[1,4] Both normal tissue function and disease progression are affected by biophysical parameters, and pathological processes often alter the mechanical properties of a soft tissue.[4]

Manual palpation is a well-known diagnostic procedure that uses tissue elasticity (resistance to deformation) to diagnose many superficially located diseases, thus illustrating the long clinical history of exploiting mechanical parameters for diagnostic purposes.[5] Prominent applications, to name just a few, include examination of the breast or prostate to detect cancer.[5] However, accurate diagnosis is only possible with many years of experience, as the mechanical clues need to be identified in relation to healthy reference tissue, making the assessment subjective and qualitative in nature. Further limitations arise when the region of interest is not easily palpable, such as the brain or liver tissue. In the liver, tissue mechanics is important for the diagnosis and staging of fibrosis.[6] Progressive scarring of liver tissue in response to inflammatory injury leads to tissue stiffening[6] and correlates with disease severity. Therefore, an early diagnose may have a positive impact on the outcome of treatment with anti-inflammatory medication.[7]

These examples illustrate that the viscoelastic properties of various soft tissues are of great clinical relevance. Current research aims at quantitatively measuring such physical properties.[4] Various imaging modalities are being developed that allow viscoelastic parameter mapping of non-palpable organs, replacing otherwise invasive approaches.[4] Further research is needed to establish mechanical parameters as biomarkers in other clinical areas for accurate diagnosis, outcome prediction, and treatment monitoring.[4,8]

1.2 Magnetic resonance elastography

As emerging technologies, ultrasound elastography and magnetic resonance elastography (MRE) seek to overcome the limitations of palpation by providing quantitative images of the tissue's elastic modulus and viscosity.[4] This allows, for the first time, the noninvasive assessment of in vivo tissue mechanical parameters of previously inaccessible organs.[4] Elastography is based on the principle that the speed of mechanical wave propagation increases with the stiffness of the material and that the damping of the waves or the lag between the applied strain and resultant stress relates to viscosity.[4] Wave speed and viscosity are measured by imaging the deformation of tissue under load in time and space using clinical imaging modalities such as ultrasound and magnetic resonance imaging (MRI).[4] In MRE, time-harmonic vibrations are introduced into the tissue to be examined using external actuators.[4] The response of the tissue is recorded using appropriate MRI sequences that employ motion-sensitive magnetic gradient fields to encode the displacement in the phase of the complex MRI signal, similar to diffusion imaging.[4] The viscoelastic properties of the biological tissue can then be reconstructed in a voxel-wise fashion from the encoded deformations using mathematical algorithms, normally based on physical models.[4] To date, several techniques have been developed that differ in the three main steps of an MRE examination: (i) mechanical excitation of harmonic deformations in the region of interest (e.g., driver arrangement and vibration frequencies), (ii) the imaging of the tissue response (type and parameters of the pulse sequence), and (iii) reconstruction of the viscoelastic properties (mathematical algorithms).[4]

1.3 Current state of research

The principles of MRE were first formulated by Muthupillai *et al.*[9] in 1995 and have been continuously developed over the last three decades. The greatest advances in human studies were achieved in the liver, as reflected by the approval of a commercial MRE device by the US Food and Drug Administration as early as 2009.[10] Many studies have demonstrated the reliability of MRE in noninvasively assessing the stiffness of the fibrotic liver compared with the highly invasive 'gold standard' of liver biopsy.[11] Not being amenable to manual palpation, the human brain is of particular interest to the MRE research community.[3,8,12-14] Apart from its paramount importance to human life, invasive techniques for mechanical testing carry significant risks.[4] One focus of recent research

has been on the healthy and unaltered mechanical properties of in vivo human brain tissue with the aim of establishing mechanical atlases for reference.[8,15-20] Another focus has been on the in vivo viscoelastic changes caused by various physiological effects and diseases in humans.[4,8,13,14] Softening of the brain occurs during normal aging[21-23] and has been observed in pathological processes associated with neuronal disorders such as Parkinson's disease[24,25], Alzheimer's disease[26-28], multiple sclerosis[29,30], and normal pressure hydrocephalus[31-33]. Stiffening of brain tissue is seen in the presence of increased intracranial pressure (ICP)[34,35], perfusion pressure[36], and neuronal activity[37] while brain tumors can show either higher or lower stiffness, depending on their entity[38,39]. Further studies reported in the literature investigated various aspects of neuronal tissue in animal models including demyelination[40-42], Alzheimer's disease[43,44], neuronal activity[45], aging[46], physiology[47], and death[48]. Fast MRE sequences, which have become available recently, allow the observation of mechanical alterations on short time scales[49-51] such as those that occur during functional activation.[37] Fast MRE sequences are particularly useful for capturing nonperiodic modulations that cannot be synchronized with a slow acquisition scheme, such as occur upon physiological challenges.[4]

A major challenge is the lack of 'ground truth' values for in vivo human brain tissue.[4] Accordingly, phantom experiments that mimic the in vivo scenario are very valuable for comparing different methods.[52] Preclinical research in animal models is also useful as reference values are more readily available.[47,53,54] An important step towards clinical application of brain MRE is to assess its consistency in terms of both between-subject and within-subject variability, which can occur over time for both technical and biological reasons.[52,55] Although a relatively wide range of values has been reported for brain tissue viscoelasticity[8,13], variation should be minimal when the same MRE technique is used repeatedly. Efforts have been made to provide reference values in atlases of brain mechanics[15,16] and to test the reliability (or reproducibility, precision) and accuracy (or validity) of brain MRE.[17,55-58] In general, MRE can be easily integrated into routine clinical workflow as it is performed as an additional sequence during an MRI examination and is therefore well suited for clinical implementation. However, the MRE method requires the use of a mechanical actuation system, which can be perceived as uncomfortable by certain patient groups.[4]

1.4 Objective of this work

The aim of this scientific project is to further develop and apply brain MRE to answer new research questions on the mechanical properties of the in vivo human brain. The project has resulted in improvements to the actuation system, imaging sequence, and reconstruction algorithm, and three studies[59-61] of in vivo brain MRE have been successfully conducted. The improved actuation system allows conducting highly reproducible brain MRE studies. For this purpose, the actuators were embedded in a custom-made holder with a transmission plate and a fixed position in the head coil.[59,60] Optimal frequencies and corresponding driving pressures were defined to achieve very good repeatability between serial experiments and experiments conducted by different users. Subsequently, MRE studies of the brain were successfully performed on three different MRI scanners with consistent results. Moreover, previously published imaging sequences of steady-state MRE (ssMRE)[49], real-time MRE (rtMRE)[50], and single-shot, spin-echo MRE[62] were adapted and customized to improve performance and image quality in the individual studies. This new acquisition scheme was combined with developments in wavenumber-based parameter reconstruction[63] for the human brain. Reconstruction from brain MRE data used to suffer from numerous heterogeneities and solid-fluid interfaces, which was overcome by the development of brain-specific data processing prior to reconstruction.[59] The novel algorithm was developed for both slice-wise two-dimensional (2D) and fully three-dimensional (3D) reconstruction.[61] These technical improvements were important for the studies[59-61]. The studies further addressed research questions of great interest to the scientific community. The viscoelasticity of healthy brain tissue[59] in response to physiological challenges[60] was studied, as well as abnormally altered brain tissue stiffness induced by multiple sclerosis (MS)[61]. In summary, the following studies were conducted:

- **Study 1:** Superviscous properties of the in vivo brain at large scales[59]
- **Study 2:** Real-time multifrequency MR elastography of the human brain reveals rapid changes in viscoelasticity in response to the Valsalva maneuver[60]
- **Study 3:** In vivo stiffness of multiple sclerosis lesions is similar to that of normal-appearing white matter[61]

Simulations and phantom experiments were an integral part of study 1[59] and 3[61].

In the first study[59], the ssMRE sequence was used to encode harmonic tissue motion ranging from ultra-low stimulation frequencies induced by arterial pulsation at heart rate (~ 1 Hz, intrinsic activated MRE [IA MRE]) to externally induced frequencies (5 – 10 Hz) to the classical range of MRE frequencies (20 – 40 Hz).[4] It was thus possible for the first time to study cerebral viscoelastic dispersion of in vivo brain tissue over a wide range of frequencies in 14 healthy volunteers.[59] Covering such an unprecedented wide range of frequencies, ssMRE can be used to measure and analyze the transition of in vivo brain tissue from its fluid-driven poroelastic tissue response to viscoelastic-dominated material properties typically measured by MRE[4].[59] Superviscous properties of brain tissue on large scales were observed, resulting in a sharp increase in stiffness between quasi-static and high-frequency measurements.[59] The results may provide a first explanation for the fundamental discrepancy between stiffness derived from static mechanical tests and in vivo MRE, which differ by orders of magnitude.[59] This transition regime of brain mechanical properties might be particularly sensitive to neurovascular integrity and vascular neurological dysfunction.[59] Ultra-low frequencies in MRE could be sensitive to tissue fluidity and viscous dispersion, opening the door to imaging inflammatory processes involving the extracellular matrix (ECM).[59] These findings were preliminarily presented at the International Society for Magnetic Resonance in Medicine (ISMRM) Virtual Conference & Exhibition 2020 and awarded with the Summa Cum Laude Merit Award.

After this study of healthy brain tissue at rest, the recently introduced rtMRE[50] sequence was used to investigate healthy brain tissue in response to physiological challenges in study 2[60]. The rtMRE sequence allowed us to overcome the usual temporal limitations of conventional MRE, which prevent the detection of short-term processes such as brain autoregulatory functions[64]. The experimental setup was extended to allow simultaneous excitation of three different narrowband driving frequencies using multiple actuators, and the sequence parameters were adjusted accordingly.[60] This increased the robustness of the reconstruction algorithm and enabled quantification of in vivo human brain viscoelasticity during cerebral autoregulation associated with the Valsalva maneuver (VM) in 17 subjects.[60] VM was induced by the use of voluntary abdominal force during breath-holding at inspiration, which occurs naturally by attempting to exhale against a closed airway.[65] The induced physiological modulations also affect the viscoelastic properties of brain tissue, as shown by MRE.[66] Sampling rates for generation

of viscoelastic parameter maps of approximately 5.4 Hz without gating were achieved.[60] The data were analyzed over the course of the experiment and revealed, for the first time, the perfusion-dependent viscoelasticity changes of in vivo brain tissue on small time scales.[60] This could provide a quantitative imaging marker of impaired cerebral autoregulation in different clinical applications and may be sensitive to ICP variations.[60]

Finally, in study 3[61], brain MRE was used to investigate the viscoelastic properties of brain tissue under pathological conditions in twelve patients with multiple sclerosis (encephalomyelitis disseminata). MS is a disease of the central nervous system featuring inflammation and demyelination, by which the myelin sheaths of nerve cells in the spinal cord and brain are damaged.[67] Earlier investigators found whole brain stiffness to be reduced in MS patients, concluding that inflammation and demyelination compromise tissue integrity in the brain.[29,30,40,68] However, little is known about the stiffness of MS lesions. Neuropathologists have characterized MS lesions by manual palpation and report that acute active lesions have soft properties while chronic inactive lesions have firm properties[69], but this observation has never be confirmed in vivo. The aim of study 3 was to investigate the possibility of distinguishing MS lesions from surrounding tissue by MRE.[61] Therefore, the stiffness contrast of MS lesions was analyzed in MRE images of a total of 147 lesions.[61] The analysis included a comparison of the heterogeneous tissue properties of MS lesions with normal-appearing white matter (NAWM) heterogeneity in the contralateral hemisphere.[61] In vivo results were further compared with data acquired in phantom experiments and simulations.[61] This study received the QUEST Null Results Award from the Berlin Institute of Health at Charité to oppose negative publication bias and honor well-conducted studies in which the initial hypothesis is not confirmed.

Collectively, all three studies aimed at gaining new insights into the mechanical properties of human brain tissue in health and disease. The methodological and technical advances accomplished in these studies provide new research tools, which can be used to address new questions in the realm of brain mechanical properties.

2 Theory

2.1 Viscoelastic theory

Elasticity and viscosity are two physical concepts which describe the behavior e.g. the deformation (strain) of a solid in response to external forces (stress). In elastic materials, the deformation is stored as potential energy and can be released without loss of energy. The object returns to its original shape when forces are no longer acting. A common example is the ideal spring.[4] In viscous materials, the deformation is irreversibly converted to heat due to internal friction and the object is permanently deformed. Honey is a practical example of a highly viscous fluid. Materials that share both properties are described by viscoelastic concepts.[4]

Elasticity is denoted in Hooke's law where it linearly relates to the rank-two tensors of stress σ_{ij} and strain ε_{kl} in case of small deformations.[4] The proportionality is given by a 3D elasticity tensor with 81 elements C_{ijkl} which defines the resistance to deformation.[4]

$$\sigma_{ij} = \sum_{k,l=1}^{3} C_{ijkl}\varepsilon_{kl} \qquad (2.1)$$

Given a symmetric strain tensor (no rotations, $\varepsilon_{ij} = \varepsilon_{ji}$) the elasticity tensor reduces to 21 independent parameters C_{ij} which ultimately reduce to two parameters (Lamé parameters λ and μ) under the assumption of isotropy.[4] The stress-strain equation is then given by[4]

$$\sigma_{ij} = \lambda\theta\delta_{ij} + 2\mu\varepsilon_{ij} \qquad (2.2)$$

δ_{ij} is the Kronecker delta and θ the cubic dilation ($\theta = \varepsilon_{11} + \varepsilon_{22} + \varepsilon_{33}$), which defines the volume change relative to the undeformed volume. In general, incompressibility ($\theta = 0, \lambda \to \infty$) can be assumed for human soft tissues. Therefore, eq. (2.2) can be expressed using only the second Lamé parameter for the shear modulus μ in case of shear deformations. This gives the stress-strain equation for an isotropic and incompressible linearly elastic material[4]

$$\sigma_{ij} = 2\mu\varepsilon_{ij}\ (i \neq j) \qquad (2.3)$$

A high shear modulus indicates that large shear forces induce small shear deformations. The material exhibits a high shear resistance and is generally considered stiff.[4]

Viscosity η is defined in a similar fashion. Nevertheless, the stress is not proportional to strain but the strain rate $\dot{\boldsymbol{\varepsilon}} = \frac{d\boldsymbol{\varepsilon}}{dt}$ (change $d\varepsilon$ over time dt, or rate of change of deformation).[4] Viscosity does not resist deformation, but rather the process of being deformed and it is related to the absorption of mechanical energy. In case of time-harmonic stresses and resulting deformations $\boldsymbol{\varepsilon} = \boldsymbol{\varepsilon_0} \cdot e^{i\omega t}$ (static strain ε_0, angular frequency ω, imaginary unit $1i = \sqrt{-1}$), the strain rate becomes $\dot{\boldsymbol{\varepsilon}} = \frac{d\boldsymbol{\varepsilon}}{dt} = i\omega\boldsymbol{\varepsilon}$ and is frequency dependent.[4] A dashpot represents a purely viscous medium in theory.[4] Altogether, the stress-strain rate equation for shear stress for an isotropic and incompressible linearly viscous material is given by[4]

$$\sigma_{ij} = 2\eta\dot{\varepsilon}_{ij} = 1i \cdot 2\eta\omega\varepsilon_{ij} \qquad (2.4)$$

Soft biological tissues typically share properties of a purely elastic and purely viscous material and are thus called viscoelastic.[4] A single viscoelastic stress-strain equation can be derived by introducing the complex shear modulus *G**, defined as[4]

$$G^* = G' + iG'' = \mu + i\omega\eta \qquad (2.5)$$

The real part *G'* is the storage modulus while the imaginary part *G''* is the loss modulus. They reflect elastic and viscous properties, respectively and are non-negative quantities. The viscous properties are responsible for the frequency dependency of *G**, also called dispersion.[4] Now, *G** is equivalent to the second Lamé parameter for viscoelastic materials subjected to time-harmonic stresses. The stress-strain equation for shear deformation reads[4]

$$\sigma_{ij} = 2G^*\varepsilon_{ij}\ (i \neq j) \qquad (2.6)$$

As any complex number, *G** can be written in polar form using its absolute value |*G**| and its argument φ. |*G**| and φ are also named shear modulus magnitude and shear modulus

phase angle. The argument is restricted to the closed interval $[0, \pi/2]$, where 0 holds for $G'' = 0$ and $\pi/2$ holds for $G' = 0$.[4]

$$G^* = |G^*| \cdot e^{i\varphi} \tag{2.7}$$

$$|G^*| = \sqrt{G'^2 + G''^2} \tag{2.8}$$

$$\varphi = \tan^{-1}\frac{G''}{G'} \tag{2.9}$$

For a purely elastic material, *G** is real-valued ($G^* = \mu$) and φ equals zero. For a purely viscous material *G** is imaginary ($G^* = i\omega\eta$) and φ equals $\pi/2$.[4]

In the presence of time-harmonic mechanical shear waves, propagating trough an infinite, homogeneous, isotropic, viscoelastic and incompressible material, *G** can be linked to the respective shear wave speed (*SWS*) using the algebraic Helmholtz equation.[4] The relation can be derived by inserting the general Hooke's law from eq. (2.1) in Newton's second law, which gives the Navier equation (full wave equation for homogeneous, isotropic material). The Helmholtz decomposition can be further used to decouple compression (longitudinally polarized) and shear (transversely polarized) wave components.[4] The resulting wave equation is called Helmholtz equation and reads[4]

$$\rho\frac{\partial^2\tilde{\boldsymbol{u}}}{\partial t^2} = G^*\nabla^2\tilde{\boldsymbol{u}} \tag{2.10}$$

ρ is the density, $\tilde{\boldsymbol{u}}$ the displacement vector of the curl field and *t* is time.[4] In comparison to the general wave equation[4]

$$\frac{\partial^2\boldsymbol{u}}{\partial t^2} = c^2\nabla^2\boldsymbol{u} \tag{2.11}$$

with wave speed *c* and wave displacement vector **u**, *G** can be linked to *SWS* for shear waves by[4]

$$SWS = \frac{1}{Re\left(\sqrt{\frac{\rho}{G^*}}\right)} = \sqrt{\frac{2|G^*|}{\rho\cdot(1+\cos(\varphi))}} \tag{2.12}$$

Moreover, complex harmonic waves (in space $\boldsymbol{r}$ and time t) with angular frequency ω, complex wavenumber $\boldsymbol{k}$ ($\boldsymbol{k} = \boldsymbol{k}' + i\boldsymbol{k}''$) and amplitude u_0 can be described as follows[4]

$$\boldsymbol{u}(\boldsymbol{r}, t) = u_0 \cdot e^{\pm i(\boldsymbol{k}r - \omega t)} \qquad (2.13)$$

They present a general solution to the wave equation and describe propagating waves in time and space. Inserting eq. (2.13) in eq. (2.11) and solving the differentiations relates the wave speed to the wave length ($\lambda = 1/k'$) and the frequency ($f = \frac{\omega}{2\pi}$). This also holds for *SWS*.[4]

$$SWS = \lambda \cdot f \qquad (2.14)$$

Commonly, |*G**| and *SWS* are used as a surrogate marker for shear stiffness and φ for fluidity. The units are pascal, m/s and radian, respectively.[4]

The general dispersion of *G** in viscoelastic materials makes it necessary to study soft biological tissue at the same frequency to ensure comparability. However, when an object is studied at different frequencies, viscoelastic models can be used to derive frequency independent parameters for better characterization.[4] The model from eq. (2.5) is called Kelvin-Voigt model. A limitation of this model is that it does not predict a frequency dependence of *G'* as observed in biological tissue.[4] Another example is the Maxwell model, which has a higher viscosity (*G''*) at low frequencies and resembles a viscous fluid rather than a solid.[4] Models can also vary in the number of parameters or complexity, but fewer parameters are generally preferred. An overview of some viscoelastic models is given in Table 1.

Table 1: Viscoelastic models and equations. (edited table from Herthum *et al.*, 2021[59])

Model	Formula	
Kelvin-Voigt	$G^* = \mu + i\omega\eta$	No dispersion in μ
Viscous	$G^* = i\omega\eta$	Purely viscous
Maxwell	$G^* = \frac{\mu \cdot i\omega\eta}{\mu + i\omega\eta}$	Dispersion in μ and η
Spring-Pot	$G^* = \mu^{1-\alpha}(i\omega\eta)^{\alpha}$	3 Parameters, Power-law dispersion in μ and η

2.2 Magnetic resonance elastography

MRE can be used to noninvasively image the viscoelastic properties of soft biological tissues in humans.[4] Shear waves, imaging sequence and parameter reconstruction form the three basic elements for any MRE technique and are discussed in more detail in this section.

Harmonic shear waves are mostly generated by external actuation systems. However, the beating heart also resembles a harmonic actuation system, emitting pulse waves through the arterial tree and causing shear deformations in brain tissue.[4] The waves propagate through the tissue of interest and their respective *SWS* and its frequency dependency are related to the materials mechanical properties.[4] An illustration of the experimental setup for brain MRE is given in Figure 1. A common problem are frequency-matched compression wave components which must be suppressed to account for the assumptions leading to eq. (2.6) and the Helmholtz decomposition leading to eq. (2.10).[4] In recent years, various actuation systems have been developed and a comprehensive review can be found in Hirsch *et al.*[4]. Nowadays pneumatic actuators are commonly used for clinical studies as they are suitable for various tissues and organs. Common frequencies range from 20 to 100 Hz, and the induced displacements are typically on the order of a few micrometers.[4] Lower frequencies generally yield good wave amplitudes with low attenuation, making them advantageous for deeper organs. Higher frequencies suffer from stronger damping but the shorter wavelength results in a good spatial support (depending on image resolution and pixel size) even in smaller regions of interest. Naturally, multifrequency MRE can be applied at multiple frequencies to either determine dispersion curves or to account for standing wave and low wave amplitude issues for single frequencies.[4]

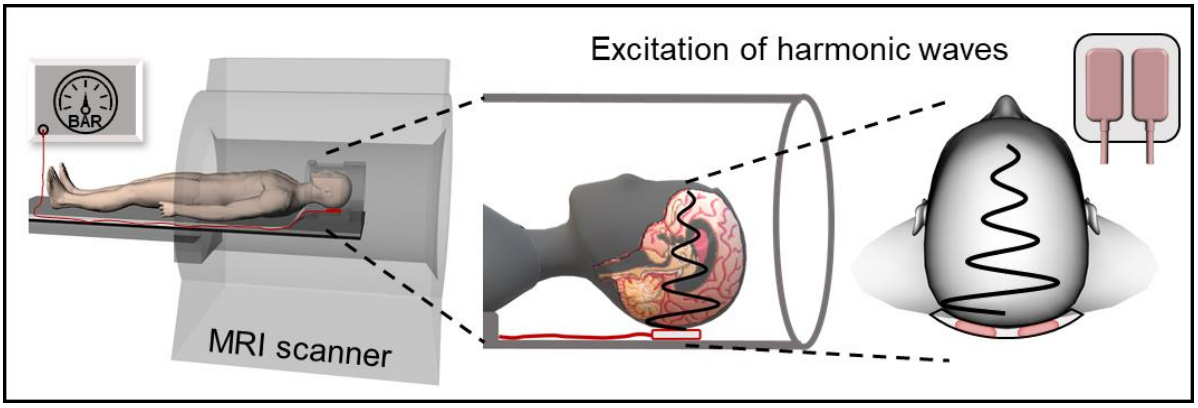

Figure 1: Illustration of the experimental setup for brain MRE examinations. The subject lays in the MRI scanner in supine position. Two actuators are positioned underneath the

head inside the head coil. Harmonic waves are induced into the brain tissue with prescribed pressure and frequency. (own figure)

MRE displacement encoding is generally performed with dedicated phase-contrast MRI sequences. The 2D displacement field is encoded slice-wise in the phase of the complex MRI signal using motion-sensitive, motion-encoding magnetic field gradients (MEGs) superimposed on the static magnetic field.[4] The phase of the MRI signal is limited to the half-open interval $(-\pi, \pi]$ and phase wraps (discontinuities) occur when the encoded phase exceeds these limits.[4] Various unwrapping algorithms exist to correct phase wraps and to resolve the discontinuities. The MEGs are shaped sinusoidal or approximately rectangular and alternate at a given frequency, duration and amplitude. Specific gradient patterns are used to suppress phase contributions from static spins (0^{th} order moment nulling), static and constant-velocity spins (1^{st} order moment nulling) or even higher order moments.[4] 1^{st} moment nulling is typically used to suppress laminar flow artifacts and rigid body motion.[4] Each MEG has a corresponding encoding efficiency ξ, given in μm/rad, which depends on the MEG parameters and the frequency of the imaged harmonic displacement.[4] In general, a good efficiency can be achieved if the frequency and duration of the MEG are within the range of the induced harmonic vibrations. If the efficiency is too high, signal dropouts may occur due to intravoxel phase dispersion. Only motion in the direction of the MEG can be encoded and encoding has to be repeated to cover a set of three orthogonal directions.[4] Typically, the encoding directions correspond to the imaging gradients in slice-selection, phase-encoding and readout directions. Since the induced deformations are time-harmonic, the fast Fourier transformation (FFT) can be used to separate unwanted signal and noise from the measurement. Therefore, the oscillation must be sampled with at least three or more equidistant sampling points. Normally, the sampling rate of the MRI is much smaller than the oscillation period and the data acquisition must be synchronized with the actuation system to sample the equidistant time points over an oscillation period.[4] Figure 2 illustrates the equidistant sampling of one wave period (T_{VIB}) over multiple sampling periods (T_{SMP}) with $T_{SMP} >> T_{VIB}$.

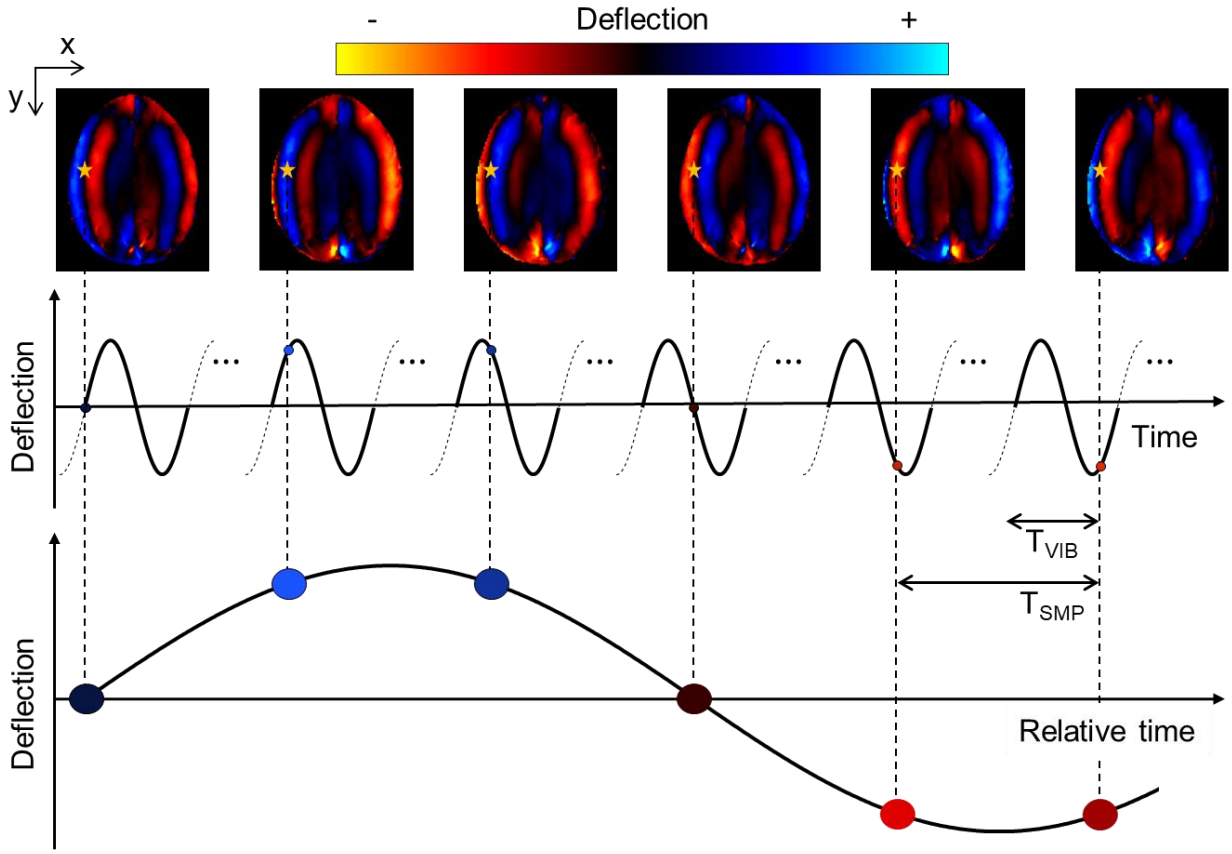

Figure 2: Illustration of the sampling pattern with six sampling points for one wave period of duration T_{VIB}. Top row shows an axial brain slice with wave deflection in y-direction and wave propagation in x-direction at 40 Hz vibration frequency. Sampling is done over multiple sampling periods with duration T_{SMP}. Since T_{SMP} >> T_{VIB}, the data acquisition needs to be synchronized with the wave period to combine the data points in such a way that one wave period is sampled with equidistant points. (own figure)

After the raw MRI/MRE data has been collected, further data processing is essential prior to the reconstruction of viscoelastic parameter maps. An illustration of MRE data processing is shown in Figure 3. As mentioned, phase wraps must be solved by dedicated unwrapping algorithms to remove phase discontinuities. Furthermore, the FFT is used to extract the signal at the induced vibration frequency and separate unrelated noise.[4] In addition, the encoded compression wave components should be removed by calculating the curl field, or at least be suppressed by any spatial highpass filter.[4] The resulting shear wavefield can be used to reconstruct the mechanical parameters of interest from the object under investigation. Hence, physical models of varying complexity exist (depending theoretical assumptions).[4] Common algorithms like multi-frequency dual elasto-visco inversion (MDEV[15,70]) and wavenumber-based MDEV (*k*-MDEV[63]) are based

on the physical model of the simplified Helmholtz equation given by eq. (2.10). MDEV is a direct inversion algorithm, which inverts the Helmholtz equation to solve for |*G**| and φ separately.[70]

$$|G^*| = \rho \frac{\sum_{j=1}^{J} \sum_{m=1}^{M} \omega_j^2 \left|\tilde{u}_m(\omega_j)\right|}{\sum_{j=1}^{J} \sum_{m=1}^{M} \left|\Delta \tilde{u}_m(\omega_j)\right|} \tag{2.15}$$

$$\varphi = arg\left(\sum_{j=1}^{J} \sum_{m=1}^{M} \tilde{u}_m(\omega_j) \cdot \tilde{u}_m^T(\omega_j)\right) \tag{2.16}$$

J is the number of frequencies, M is the number of MEG components, $\tilde{u}_m(\omega_j)$ denotes the complex-valued curl component (m = 1...M) at vibration frequency ω_j (j = 1…J) and $\tilde{u}_m^T$ denotes the complex conjugate. Δ is the 2D or 3D Laplace operator. Here several frequencies are averaged to increase robustness, however the frequency dispersion is neglected, which strictly only holds for pure elastic materials.[4] *k*-MDEV is an approach that determines wavenumbers based on the phase gradient of propagating plane waves described by eq. (2.13), including amplitude-weighting before averaging of components and frequencies.[63] The shear wavefield needs to be decomposed into N plane waves using directional filters ϑ_n for n = 1…N directions.[63] For each plane wave component $\tilde{u}_m$ the vector norm (k'_m) of the real part of the complex wavenumber is given by[63]

$$k'_m = \|\boldsymbol{k}'_m\| = \left\| \nabla \frac{\tilde{u}_m}{|\tilde{u}_m|} \right\| \tag{2.17}$$

The gradient ∇ can be in 2D or 3D. Eq. (2.14) can be used to determine the *SWS* by

$$SWS(\boldsymbol{r}) = \left(\frac{\sum_{j,m,n} \frac{k'_m(\boldsymbol{r}, \omega_j, \vartheta_n)}{\omega_j} w_m(\boldsymbol{r}, \omega_j, \vartheta_n)}{\sum_{j,m,n} w_m(\boldsymbol{r}, \omega_j, \vartheta_n)} \right)^{-1} \tag{2.18}$$

with j the frequency index, m the MEG component index and n the direction index.[63] The empirical weight function $w_m(\boldsymbol{r}, \omega_j, \vartheta_n) = \left|\tilde{u}_m(\boldsymbol{r}, \omega_j, \vartheta_n)\right|^p$ favors high amplitude signals to the power of p (p = 4 was proposed by Tzschätzsch *et al.*[63]). *k*-MDEV employs first-order

finite difference operators (FDOs) which have been widely used in abdominal MRE and were recently applied to mouse brain MRE.[71] In the human brain, however, inversion techniques such as MDEV are normally used, which invokes second-order FDOs.[46,62,72] FDO-based stiffness estimates are susceptible to underestimation due to noise and overestimation due to discretization.[73] Both over- and underestimation is more pronounced in second-order FDOs than in first-order FDOs, making *k*-MDEV more robust against noise than MDEV inversion.[63,71] However, *k*-MDEV has never been used for the human brain since heterogeneities and abundant solid-fluid interfaces degraded the results.

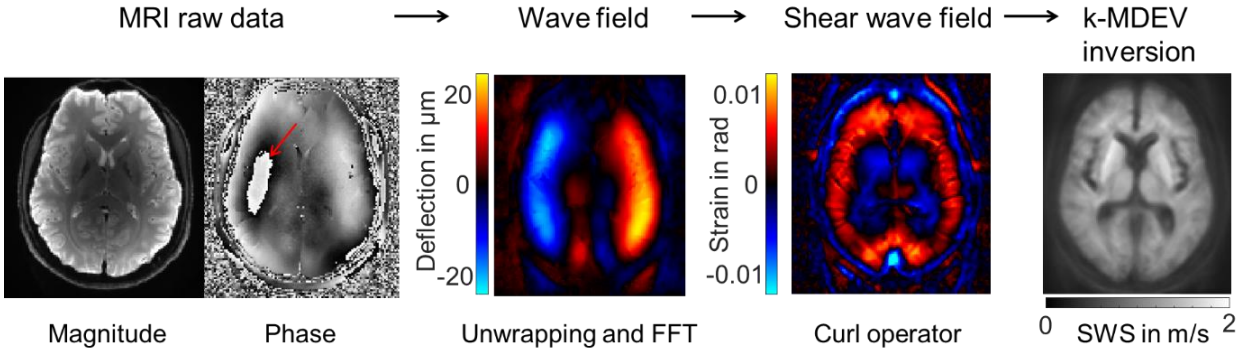

Figure 3: Illustration of MRE data processing for reconstruction of *SWS* map as a surrogate marker for tissue shear stiffness using the *k*-MDEV algorithm. The phase of the complex MRI signal is subjected to phase unwrapping (the red arrow indicates an area of high wave amplitude where the phase is wrapped from $-\pi$ to $+\pi$ and a phase discontinuity arises). The wavefield at the induced vibration frequency is extracted using the FFT. The shear wavefield is determined from the curl operator and the phase gradient from directionally filtered plane waves allows for reconstructing *SWS*. A brain adapted *k*-MDEV based inversion pipeline will be proposed in the following. (own figure)

3 Methods

3.1 Subjects

All studies[59-61] were approved by the ethics committee of the Charité – Universitätsmedizin Berlin in accordance with the World Medical Association Declaration of Helsinki, which defines the Ethical Principles for Medical Research Involving Human Subjects (study 1[59] and study 3[61]: EA1/085/17, study 2[60]: EA1/004/19). All participants were older than 18 years and had no risk factors related to the performed experiments.[59-61] Participants provided written informed consent.[59-61] Healthy volunteers had no history of neurological diseases and patients were stable relapsing-remitting multiple sclerosis (RRMS) patients receiving standard immunomodulatory treatment.[59-61] Age and sex of all participants were documented.[59-61]

In study 2[60], the body mass index of each participant was documented.[60] Blood pressure was recorded at rest (left arm, lying supine) and fingertip pulse was recorded throughout the experiment using an oximeter.[60] In study 3[61], months since disease onset and since last relapse were documented. Participant characteristics are given in Table 2.

Table 2: Participant characteristics for each study (data given in mean ± standard deviation).[59-61] (own table)

	Study 1	Study 2	Study 3
Number of participants	14 (3 women)	17 (5 women)	12 (5 women)
Age,	30 ± 5,	36 ± 13,	45 ± 14,
range (years)	24 – 44	25 – 81	25 – 64
Body mass index (kg/m^2)		23 ± 3	
Systolic blood pressure (mmHg)		122 ± 16	
Diastolic blood pressure (mmHg)		74 ± 10	
Heart rate (resting state; bpm)		71 ± 10	
Month since disease onset,			175 (134),
range			5 – 469
Month since last relapse,			56 (78),
range			2 – 289

3.2 Non-human experiments and simulations

In study 1[59] and 3[61], non-human experiments and simulations were used to test and validate data analysis strategies for the in vivo experiments. However, due to space limitations only a brief summary of the employed methods and results is given here. Further information can be found in the respective publications. In study 1[59], three ex vivo bovine brain experiments and finite element method (FEM) based simulations were used to investigate the shear modulus of brain tissue under static deformation. Deformation was induced by bending over an edge by gravity.[59] The brain's shear modulus was estimated by using 2D FEM simulations with varying initial shear modulus.[59] Good agreement between simulation and experiment was achieved for a bending shear modulus of 133 ± 29 Pa.[59] Figure 4 shows the bovine brain in its deformed state with various FEM simulations superimposed on the anatomical MRI image.

Furthermore, phantom tests in heparin-sodium gel were used to validate the in vivo MRE data analysis through profile-based *SWS* estimation.[59] Oscillatory shear rheometry was used to measure reference values for the gel at different frequencies.[59] However these experiments will not be part of this dissertation.

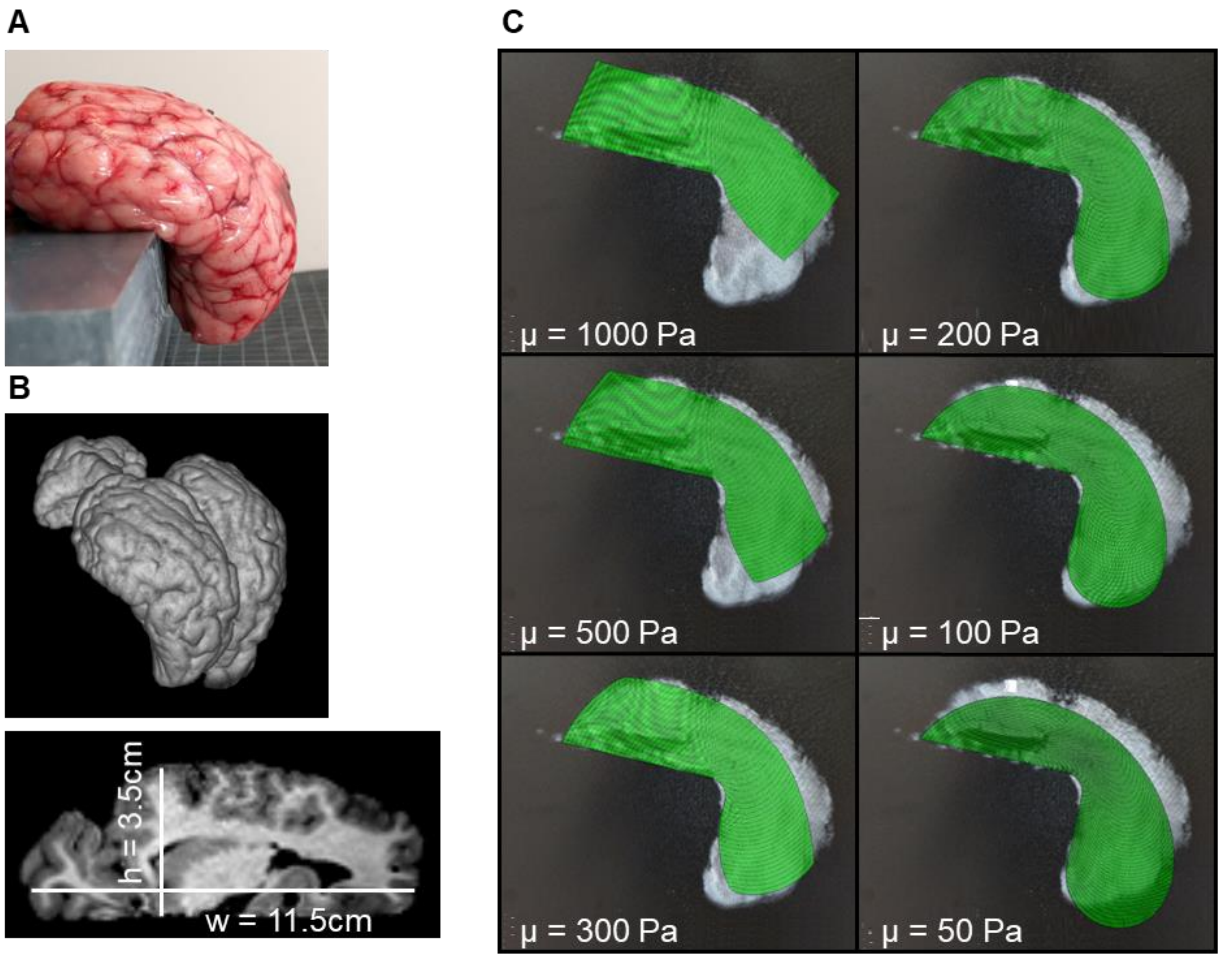

Figure 4: Bending experiments and FEM simulations illustrate super soft properties of ex vivo bovine brain tissue.[59] **A** Photograph of fresh brain bent by gravity over an edge.[59] **B** Anatomical MRI image of deformed and undeformed brain.[59] **C** FEM simulation results with varying initial shear modulus overlaid on sagittal MRI image.[59] (figure from Herthum *et al.*, 2021[59])

In study 3[61], finite-difference wave simulations were performed to estimate the resolution-dependent sensitivity boundaries of two inversion algorithms, MDEV and *k*-MDEV, as described below.[61] This involved simulating circular inclusions with a Gaussian shaped stiffness profile within a 1.5 kPa background.[61] Lesion size and stiffness contrast were varied (size: 5 mm – 38 mm, contrast: -75 % – 200%).[61] Both inversions were used for stiffness reconstruction and the difference to the true stiffness contrast was determined.[61] Figure 5 shows the simulation results. The first row shows that both pipelines underestimated the true stiffness contrast of -80% for a 1 cm wide inclusion.[61] However, MDEV performed better with smaller errors.[61] The simulated wavefields are shown in the second row. Figure 5B shows the contrast estimation error in % as a function

of width and true contrast. Negative contrasts were recovered better, while positive contrasts were severely underestimation in both pipelines.[61] The error increased with decreasing inclusion size.[61] These findings were compared with data acquired from phantom experiments and the respective details can be found in Herthum *et al.*[61].

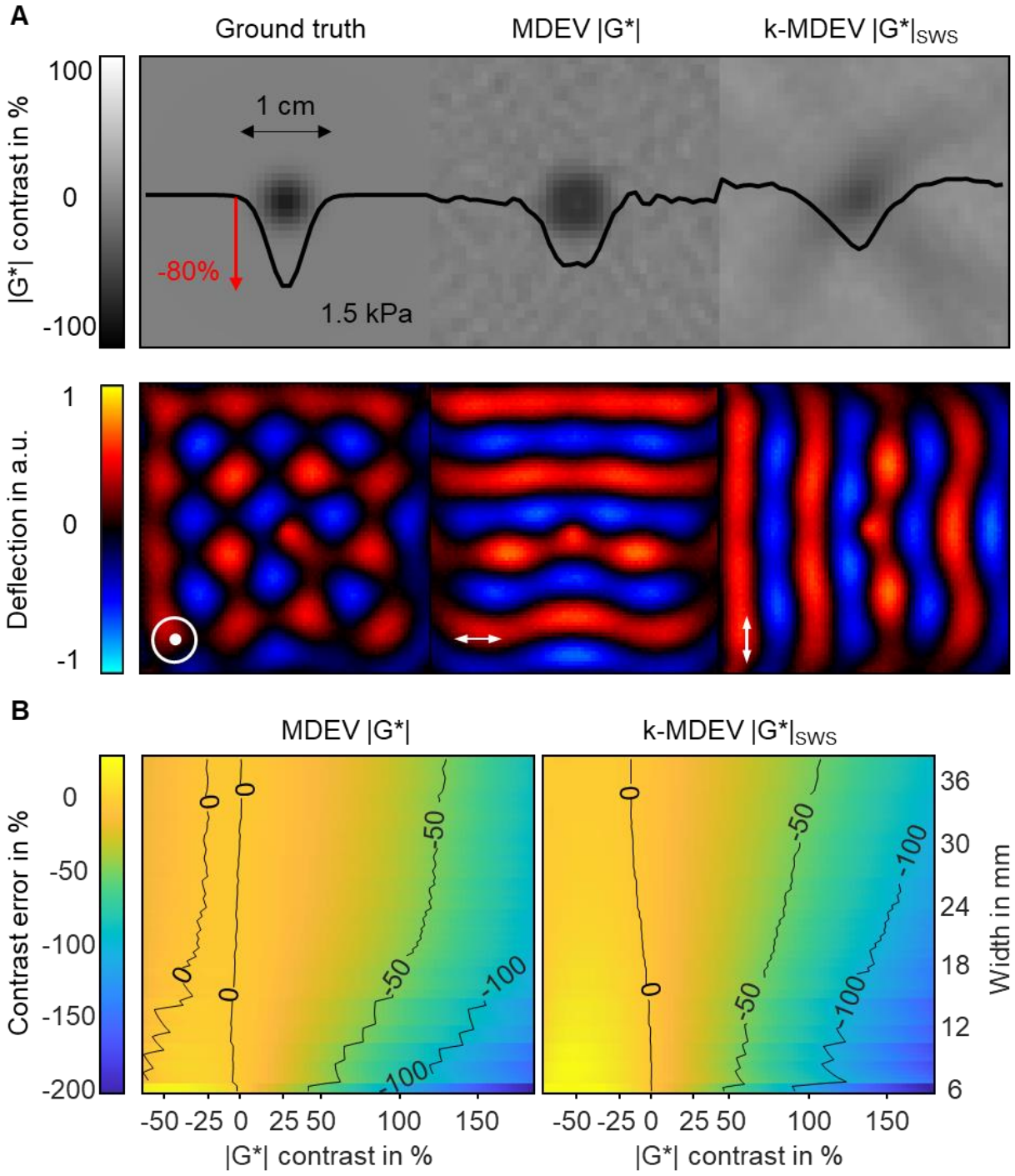

Figure 5: 2D finite-difference wave simulation and reconstruction results. **A** Top row shows an example for an inclusion of 1 cm width, Gaussian shape and -80% contrast

relative to the background (1.5 kPa) together with the reconstruction results for |*G**| based on MDEV and *k*-MDEV. The second row shows the simulated input wavefields in three deflection directions (⊙, ↔, ↕ denote deflections through-plane, left-right, and up-down, respectively) **B** Error map for contrast reconstruction for |*G**| from MDEV and *k*-MDEV. The x-axis shows the true contrast and the y-axis the width of the inclusion. The error is coded in color corresponding to the colorbar. (edited figure from Herthum *et al.*, 2022[61])

3.3 MRE experimental setup

In all studies[59-61], continuous harmonic vibrations were induced in the subject's brain tissue using two (single frequency, study 1[59] and 3[61]) or four (narrowband frequencies, study 2[60]) pneumatic air drivers (thickness: 1 cm, length: 8 cm, width: 4 cm) as illustrated in Figure 6A. Each driver was supplied by a compressed air tube. The drivers operated either in phase (study 1[59]) or with a phase delay of 180° (study 2[60] and 3[61], Figure 6B). The drivers were placed in a standard 32-channel head coil at a fixed position under the subject's head with a connection plate in between (Figure 6C).[59] The applied air pressure of the drivers was varied depending on the actuation frequency.[59] Steady state of harmonic vibrations was ensured by a 2 s forerun prior to data acquisition.[59] The air drivers were operated using a stand-alone control unit, which was synchronized with the MRI using optical trigger signals.[59]

Transversal slice positioning for single-slice (study 1[59] and 2[60]) and multi-slice MRE acquisitions (study 3[61]) and other anatomical sequences was automatically assigned by the *auto align* function of the scanner. This ensured optimal left-right laterality of brain hemispheres and optimal comparability between subjects. Figure 6D illustrates the automatic slice positioning in sagittal view as it was done in study 2[60]. For the multi-slice acquisition in study 3[61], the central slice would align with the one presented here. In addition, the manually delineated region of interest (ROI) for further parameter analysis from study 2[60] is shown. MRE imaging parameters are summarized in Table 3.

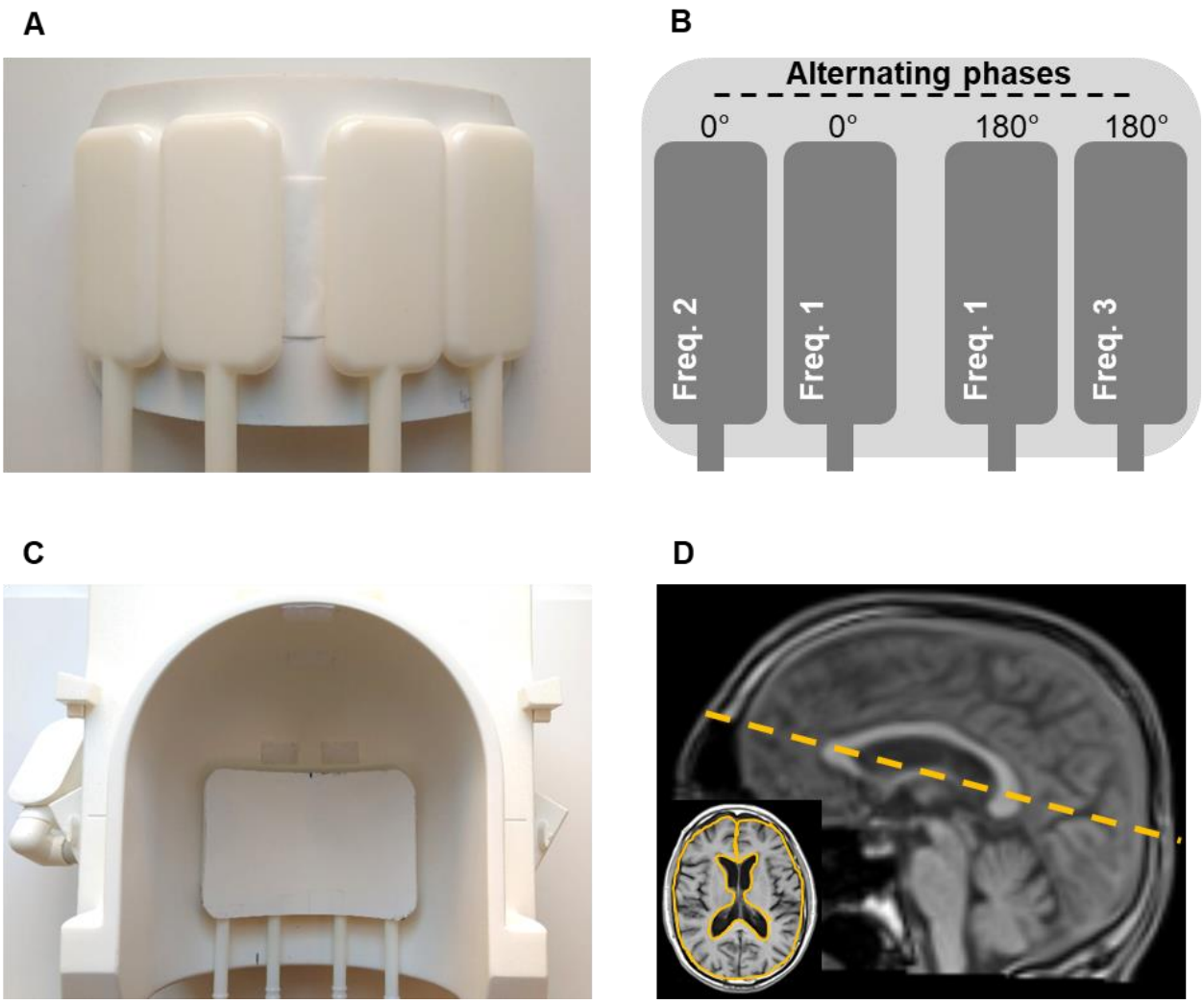

Figure 6: Experimental setup and automatic slice positioning from study 2[60] as it was also applied in study 1[59] and 3[61]. **A** Flask shaped air drivers attached to the connection plate (bottom view). **B** Illustration of driver placement, actuation frequencies and phase offsets between drivers. In study 1[59] and 3[61] only the two innermost drivers were used. **C** Placement of driver setup in a head coil with 32-channels (top view). **D** Automatic slice positioning (yellow line) in sagittal view of anatomic image from study 2[60]. Insert illustrates manual ROI delineation based on anatomical images from study 2[60] in transversal view. (edited figure from Herthum *et al.*, 2021[60])

Table 3: MRE imaging parameters for each study. For study 1[59], imaging parameters slightly differed for acquisition of intrinsic activated ssMRE (IA), low frequencies between 5 and 20 Hz and the conventional range between 20 and 40 Hz. (own table)

	Study 1	Study 2	Study 3
Scanner model	Siemens Magnetom Sonata	Siemens Magnetom Prisma	Siemens Magnetom Prisma
Static magnetic field strength of the scanner (T)	1.5	3.0	3.0
Sequence type	Gradient echo with spiral readout	Gradient echo with spiral readout	Spin echo with cartesian EPI readout
Echo time (ms)	20	20	78
Repetition time (ms)	60, 45, 40	62	4680
Flip angle	20°	20°	90°
Field of view (mm^2)	220x220	192x192	200x200
Voxel size (mm^3)	1.7x1.7x5 (IA), 1.1x1.1x5 (5 – 23.4375 Hz), 1.1x1.1x5 (20 – 40 Hz)	2x2x5	2x2x2
Matrix size	128x128 200x200 200x200	96x96	100x100
Number of images	334, 222, 222	1458	96
Sampling rate (Hz)	16.7, 22.2, 25	5.4	-
MEG amplitude (mT/m)	30	40	34
MEG duration (ms)	15	17.5	32.5
MEG moment nulling	0^{th}	0^{th}	1^{st}
Encoding directions	3	3	3

Encoding efficiency (μm/rad)	353.2, 71.4 – 19.2, 19.2 – 10.9	8.1	8.6, 6.4, 5.4, 5.3
Frequencies (Hz)	IA, 5, 6.25, 7.8125, 10, 12.5, 15.625, 20, 23.4375, 30, 31.25, 40	30.03, 30.91, 31.8	20, 25, 30, 40
Total scan time (min)	2.1, 4.6, 2.1	1.5	8

3.3.1 Study 1

In study 1[59], all experiments were conducted in a 1.5T MRI scanner (Siemens Magnetom Sonata, Erlangen, Germany) using MEGs with 30 mT/m amplitude. First, intrinsically activated ssMRE[49] (single-slice, single-shot) was performed in each volunteer without external wave stimulation. 334 consecutive motion-sensitive images were acquired with a frame rate of 16.7 Hz.[59] The experiment was followed by ssMRE (single slice, multi-shot [9 interleaves]) and external wave stimulations at ultra-low frequencies (5, 6.25, 7.8125, and 10 Hz) to capture 222 images at a frame rate of 22.2 Hz.[59] Higher frequencies in the conventional range (20, 31.25, and 40 Hz) were acquired with 100 images at a frame rate of 25 Hz.[59] Data acquisition was started by a cardiac trigger in each case and repeated for the three orthogonal components of the wavefield.[59] The nonlinear motion of the drivers induced additional higher harmonic frequency components that were additionally evaluated.[59] Specifically the second harmonic of 6.25 Hz (12.5 Hz) and of 7.8125 Hz (15.625 Hz) and the third harmonic of 7.8125 Hz (23.4375 Hz) and of 10 Hz (30 Hz).[59] Others were skipped because of low wave amplitudes or redundancy.[59] The real part of the complex wave images at the specific harmonic frequency in one volunteer is illustrated in Figure 7. Wavefields induced by the intrinsically activated pulse wave were extracted using the FFT at the mean heart rate of the subject during the experiment.[59] The pulse wave traveled outwards from a point-source at the circle of Willis[74].[59] The anterior-posterior encoding direction is displayed for the externally induced waves.

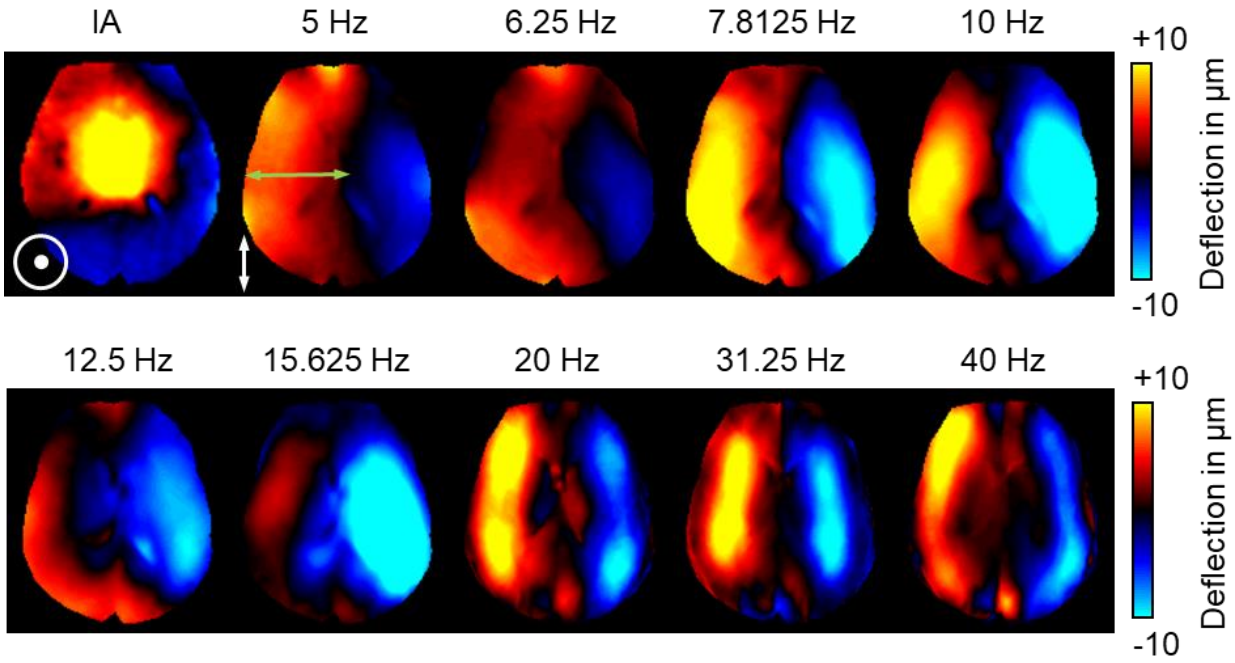

Figure 7: Example wave deflection images after temporal Fourier transformation from intrinsic actuation (IA) MRE to ultra-low frequencies between 5 – 10 Hz with their higher harmonics (12.5 and 15.625 Hz) up to conventional MRE (20 – 40 Hz) from study 1[59]. For IA MRE the through-plane component (head-to-feet, ⊙) is shown, otherwise the anterior-posterior encoding direction (up-down, ↕) is shown. The green arrow indicates the position where the data for the bi-directional fit was extracted. Wave images at 23.4375 and 30 Hz images were left out due to reasons of space. (edited figure from Herthum *et al.*, 2021[59])

3.3.2 Study 2

All experiments in study 2[60] were performed in a 3T MRI scanner (Siemens MAGNETOM Prisma, Erlangen, Siemens) using MEGs with 40 mT/m amplitude. A single-slice, single-shot, gradient-echo rtMRE sequence was optimized for brain examinations to sample the induced vibrations in a predetermined fashion with a spiral readout trajectory.[60] The sequence was originally developed to study dynamic muscle function at high frame rates.[50] The three orthogonal displacement components were captured in an interleaved fashion, which allowed to sample the full 3D displacement vector with a frame rate of $\frac{1}{3 \cdot TR} \approx 5.4\ Hz$.[60]

Each volunteer performed three physiological challenges during data acquisition (with 30 s break between each challenge).[60] First, 5 s breath-hold in inspiration followed by 20 s Valsalva maneuver.[60] Second, breath-hold at deep inspiration (BH-in, 25 s) and

third expiration and breath-hold (BH-ex, 25 s).[60] The total acquisition time was 90 s per experiment, including a 30 s baseline prior to the challenge and a 35 s recovery phase afterwards.[60]

Four air drivers were used to continuously induce three narrowband frequencies (30.03, 30.91 and 31.8 Hz).[60] The encoding efficiency was approximately 8 µm/rad.[60] The two inner drivers operated out of phase at 30.03 Hz.[60] The higher frequencies were applied laterally and out of phase to each other, as illustrated in Figure 8.[60] Figure 9 illustrates the recorded wave deflections for one representative volunteer. A T1-weighted, turbo-spin echo sequence was used to collect anatomical images.[60]

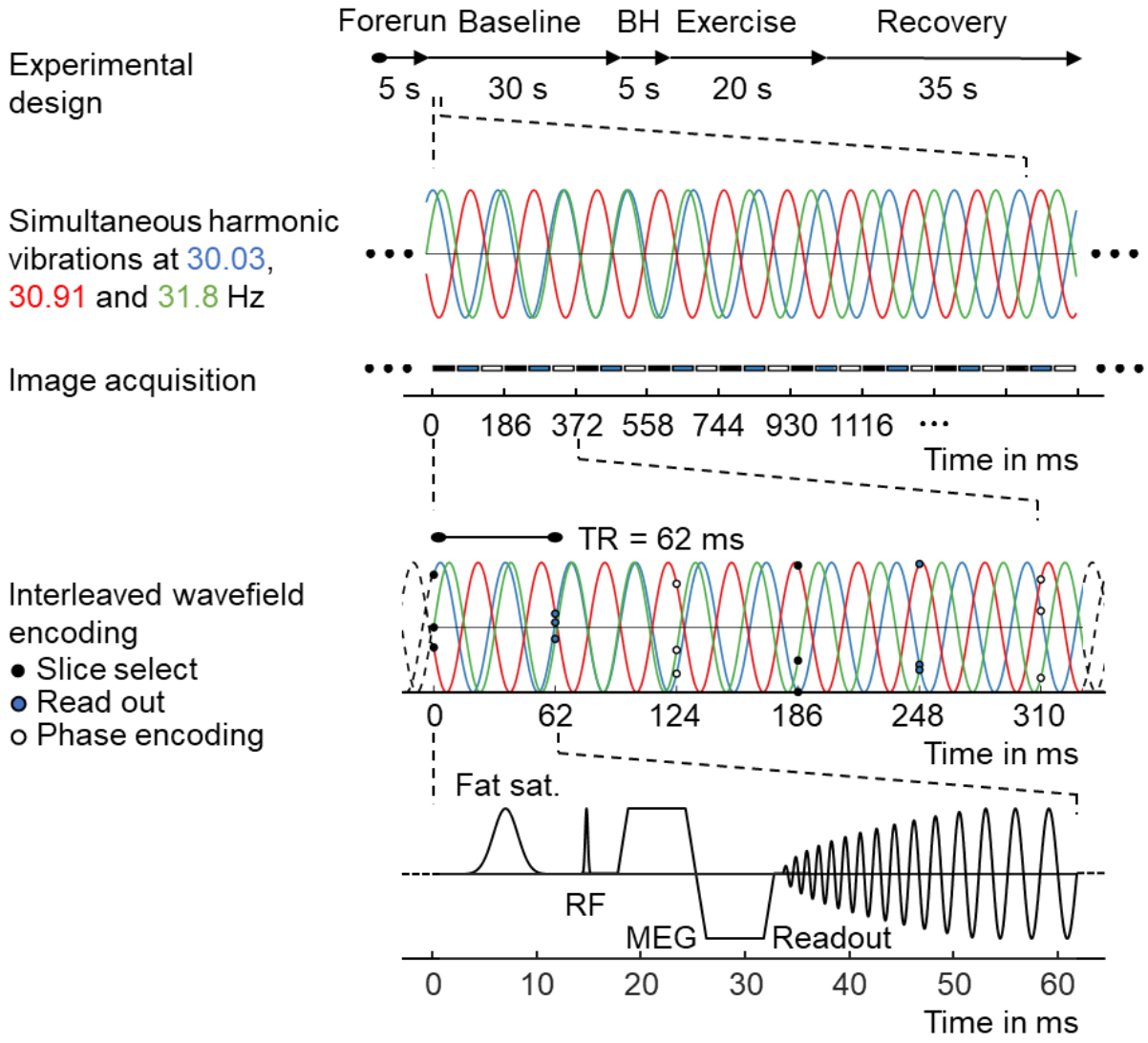

Figure 8: Timing diagram for experimental design (top row) and the single-shot multifrequency real-time MRE sequence (bottom row). A steady-state gradient echo sequence with spiral readout trajectory is used. Synchronized image acquisition for

harmonic vibrations at three frequencies over the period of 9 x 3 repetition times (TR) is shown in the second row. The interleaved wavefield encoding is illustrated in the third row for a period of 2 x 3 TRs. The simplified sequence diagram consists of fat saturation (Fat sat.), radiofrequency (RF) excitation, motion-encoding gradient (MEG) and spiral readout. (edited figure from Herthum *et al.*, 2021[60])

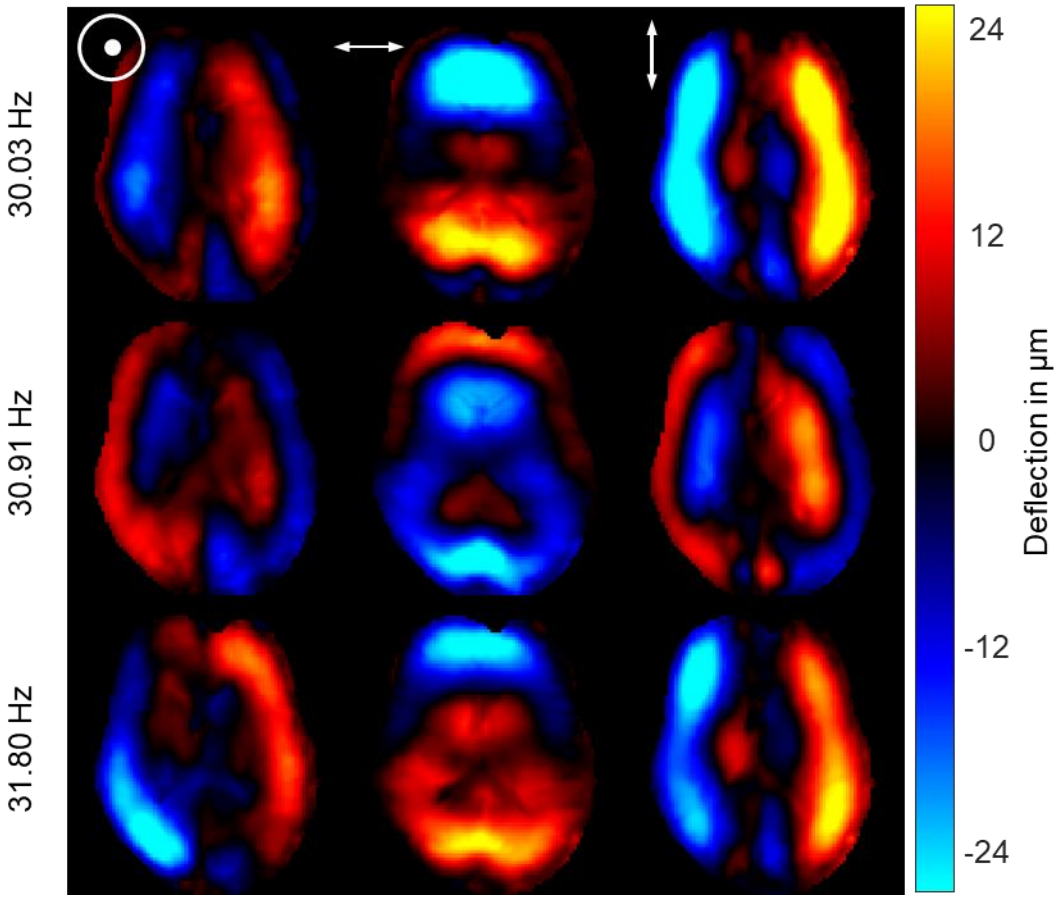

Figure 9: Example wave deflection images at each actuation frequency after temporal Fourier transformation in one volunteer for all encoding directions in study 2[60] (⊙, ⟷, ↕ represent displacements in head-to-feet [through-plane], left-right, and anterior-posterior [up-down] direction, respectively). (edited figure from Herthum *et al.*, 2021[60])

3.3.3 Study 3

All experiments of study 3[61] were conducted in a 3T MRI scanner (Siemens MAGNETOM Prisma, Erlangen, Siemens) using MEGs with 34 mT/m amplitude. Multifrequency MRE was performed with two pressurized air drivers and recorded with a spin-echo echo-planar imaging sequence.[61] Harmonic vibrations (20, 25, 30 and 40 Hz)

were continuously sampled at eight equidistant time points over one vibration period in 36 axial slices and three orthogonal encoding directions.[61] The frequency-averaged encoding efficiency was 6.4 µm/rad.[61] Example wave deflection images in one subject are shown in Figure 10. The total acquisition time was approximately 8 min.[61] Anatomical T2-weighted images were recorded using a 3D sequence with turbo-spin-echo and fluid attenuation inversion recovery (FLAIR).[61]

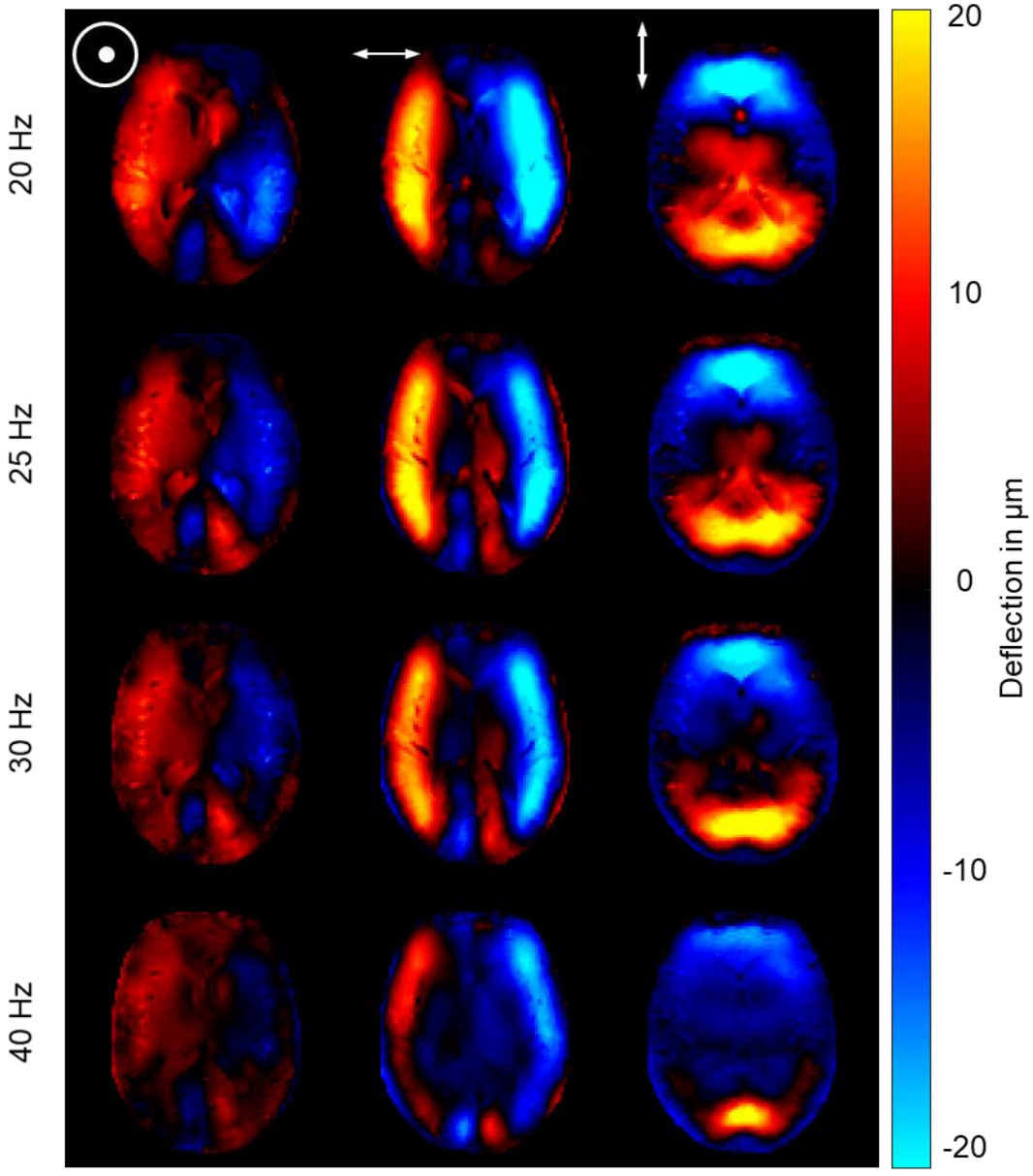

Figure 10: Representative wave deflection images at each actuation frequency after temporal Fourier transformation in one volunteer for all encoding directions in study 3[61] (⊙, ⟷, ↕ represent displacements in head-to-feet [through-plane], left-right, and anterior-posterior [up-down] direction, respectively). (edited figure from Herthum *et al.*, 2022[61])

3.4 Registration and segmentation

In study 3[61], slice-wise 2D motion correction was performed for the complex-valued MRE images prior to further data processing. Head motion was corrected using SPM12[75].[61] SPM12 was also used to co-register the anatomical FLAIR images with the averaged MRE magnitude images.[61] Averaging was done over time steps, encoding directions and oscillation frequencies.[61] Co-registered FLAIR images were further used as a visual guidance to identify and manually delineate 3D lesions based on averaged MRE magnitude images using ITK-SNAP[76].[61] Lesions smaller than 32 mm^3 were automatically excluded from further analysis. An experienced neuroradiologist in MS lesion identification performed the segmenation.[61] SPM12 was used to automatically generate tissue probability masks for cerebrospinal fluid (CSF), grey matter, and white matter (WM). Logical masks for further use were generated by thresholding the probability masks at 0.5.[61]

3.5 Viscoelastic parameter reconstruction

All data processing was done with MATLAB[77] (R2018b and R2020a, toolboxes: Signal Processing, Image Processing, Wavelet, Statistics, Global Optimization) unless otherwise stated.

3.5.1 Study 1

In vivo wideband reference values for SWS

In study 1[59], experimental data were modelled along one-dimensional (1D) profiles for all excitation frequencies using complex harmonic functions to generate reference *SWS* values. The profiles were manually drawn perpendicular to the main propagation direction of the imaged waves for the anterior-posterior encoding direction.[59] Wavenumbers were obtained by least-squares fitting of the data and the model using the function *fminsearch* in MATLAB.[59] The model consisted of two damped waves with same complex wavenumber $k = k' + ik''$ of opposite propagation directions (bi-directional), different amplitudes A_1 and A_2 and different initial phases φ_1 and φ_2.[59]

$$u(x) = A_1 \cdot e^{+i(kx+\varphi_1)} + A_2 \cdot e^{-i(kx+\varphi_2)} \qquad (3.1)$$

The performance of the model was compared in numerical simulations with a simplified model of a uni-directional wave by setting A_2 = 0.[59] The increased complexity of a bi-directional model allowed analyzing the data without directional filtering in the Fourier domain in order to separate opposite travelling waves.[59] At low wavenumbers and few sample points, the Fourier decomposition is prone to Gibb's ringing, which biases further data analysis and was not needed in the bi-directional fitting approach.[59] Examples of the profile-based analysis of the experimental data along 1D lines (green arrow Figure 7) in one subject is shown in Figure 11. The bi-directional fit of the complex data is shown by dotted lines. It is visible that the wavelength of the induced waves mostly exceeds the spatial extent of the profile.[59] However, the curvature and phase shift between the real and imaginary part are well visible.[59] The bi-directional fit sufficiently modelled the data in order to estimate the underlying wavelength.[59] At last, *SWS* values were obtained from profile-based wavenumbers using eq. (2.14).[59]

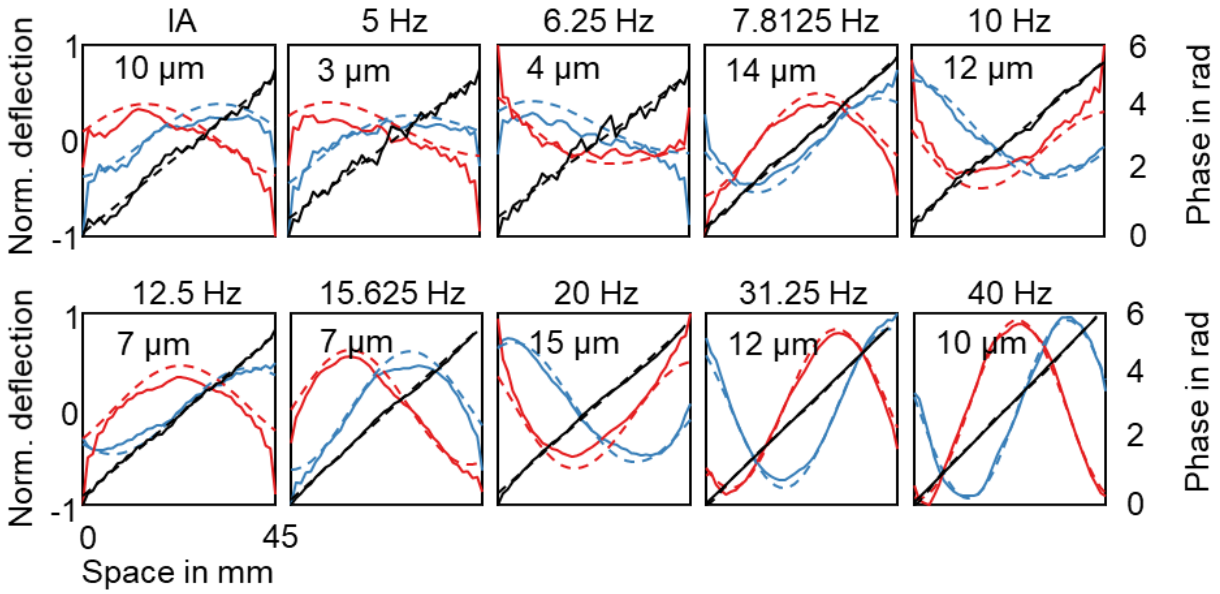

Figure 11: 1D profile-based analysis of wave deflections in one subject as shown in Figure 7. Imaginary part (red) and real part (blue) of the complex wave were fitted using the bi-directional model (dotted line) as described in eq. (3.4). The phase (black) with its corresponding fit (dotted black line) is shown as well. (edited figure from Herthum *et al.*, 2021[59])

Adaption of k-MDEV to brain MRE data

The *SWS* values from the profile fits in study 1[59] were used as a reference for in vivo MRE data to adapt the data processing of wavenumber (*k*-) based multi-component, elastic-viscous (*k*-MDEV) inversion[63] to brain MRE images. As detailed in the theory section, *k*-MDEV provides *SWS* maps, which are a surrogate marker of tissue stiffness. The inversion avoids excessive noise enhancement, which is caused by the Laplacian operator used in direct inversion techniques[4,73]. Higher signal-to-noise ratio (SNR) and better resolution compared to abdominal MRE data allowed for a substantial reduction in smoothing without compromising reproducibility and data consistency.[59] This effectively reduced the point spread function of the inversion algorithm, which is beneficial for detail and edge resolution.[59] The novel pipeline can be used for automatic 2D data processing, which is indispensable for further applications and clinical translation.

Prior to unwrapping the phase images of the complex MRI signal, the Gaussian smoothing kernel (σ = 2.75 mm, full width at half maximum (FWHM) ≈ 6.5 mm) was replaced by a Butterworth lowpass filter of 3rd order with threshold 250 m^{-1} (FWHM ≈ 2.8 mm).[59] As originally proposed by Dittmann *et al.*[62], the phase images were unwrapped with a 2D Laplacian-based phase unwrapping method. The FFT was subsequently used to extract harmonic component of the complex-valued wavefield at the actuation frequency. Since plane wave propagation is assumed for phase gradient methods, directional filters were applied as explained in Tzschätzsch *et al.*[63]. However, the radial filter in the spatial frequency domain (linear cone) was replaced by a Butterworth bandpass filter of 3rd order with a lowpass and highpass threshold of 200 m^{-1} and 15 m^{-1}, respectively, to suppress compression waves.[59] The filtered wavefields were finally processed by the *k*-MDEV inversion.[59] No frequency component weighting was used in the inversion.[59] The individual wave components were weighted with their respective squared amplitudes.[59]

It should be noted that the strength of smoothing, which is controlled by the lowpass filters, is a tradeoff between noise reduction and detail resolution and can be adjusted individually. In general, the strength of the smoothing depends on the data quality, i.e., the resolution and the noise in the phase images, which is proportional to the magnitude SNR and the encoded wave amplitude. Moreover, a full 3D inversion based on the *k*-MDEV algorithm was developed and presented at the ISMRM 2021[78]. For this purpose, slice phase offsets and inter-slice phase discontinuities were removed after the temporal Fourier transformation according to Barnhill *et al.*[79] and the radial bandpass

Butterworth filter was applied in three dimensions.[78] The slice-wise 2D directional filter with eight uniformly distributed segments was extended to 3D by a dodecahedron with 20 corners, dividing the wavefield into 20 propagation directions.[78] Finally, the 3D phase gradient was computed to reconstruct *SWS* maps.[78] This approach could be beneficial if a sufficiently large number of slices are recorded to incorporate through-slice wave propagation patterns. Further details and results can be found in Herthum *et al.*[78]. 2D and 3D data processing followed by the *k*-MDEV inversion was also used to generate maps of *SWS* in study 3[61].

3.5.2 Study 2

Time-resolved viscoelastic parameter reconstruction

In study 2[60], the MDEV inversion, as described in the theory section, was employed to reconstruct time-resolved viscoelasticity parameters. The temporal Fourier transformation of the data processing was adjusted as introduced and outlined in Schrank *et al.*[49]. Typically, one complex wavefield is recovered from the frequency spectrum of the temporal Fourier transformation at a single frequency (corresponding to the induced harmonic vibration), collapsing all measured time points. To generate a series of time-resolved wavefields, the spectrum is instead multiplied with a Gaussian bandpass filter of a given width σ centered at the frequency of the induced harmonic vibration f_0.[50] This effectively nulls one side of the spectrum, which makes the inverse transformation a Hilbert transformation. The Gaussian bandpass filter in the frequency domain translates into a weighted average of the inverse width $\frac{1}{\sigma}$ in the time domain and the multiplication becomes a convolution. The more frequencies included (large σ), the fewer measured time points needed to reconstruct a single parameter map. This allows faster tracking of viscoelastic changes, but introduces more noise and ringing artifacts. Consequently, the width of the Gaussian bandpass filter was chosen according to the expected temporal dynamics of the experiments and set to $\sigma = 0.1$ Hz.[60] All other parts of the data processing and the inversion were the same as described next.

The time-resolved complex-valued wavefields for each of the three excitation frequencies and encoding directions were recovered from the bandpass filtered Fourier spectrum centered at the aliased frequencies with subsequent inverse Hilbert transformations.[60] Aliasing occurred due to undersampling of higher frequencies at the sampling rate of approximately 5.4 Hz.[60] Nevertheless, the experimental design ensured

a good separation of the aliased excitation frequencies, as shown in Figure 12.[60] At each time point, the wavefields at the three excitation frequencies and encoding components were used to reconstruct a single 2D map of the shear modulus magnitude $|G^*|$ and phase angle φ, resulting in 486 consecutive parameter maps over the entire examination time for $|G^*|$ and φ.[60] The nonperiodicity of the discrete time series led to edge artifacts of the Hilbert transformation, which were discarded by removing a 5 s interval at the beginning and end of the reconstructed time series of the parameter maps.[60] Consequently, further data analysis was restricted to an 80 s time window.[60]

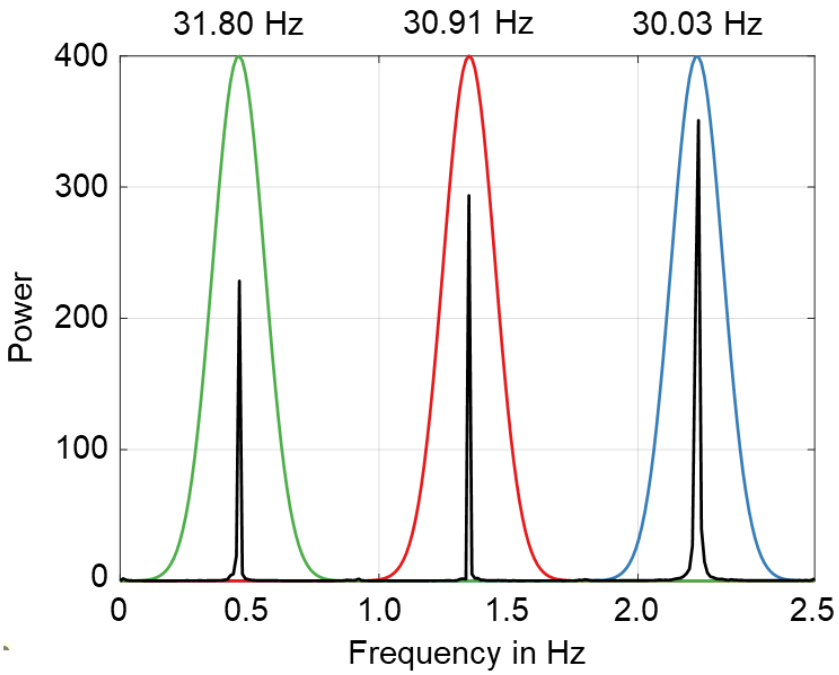

Figure 12: Power spectrum of simultaneously excited vibration frequencies (30.03 Hz, 30.91 Hz and 31.80 Hz) averaged over the ROI covering the volunteer's parenchyma in a single slice. The frequencies appear at their aliased positions in the spectrum, which only extends to the Nyquist frequency of approximately 2.7 Hz. 30.03 Hz shows the highest power, as it is also visible in Figure 9. The individual Gaussian shaped filter functions (width $\sigma = 0.1$ Hz) are shown in color. (edited figure from Herthum *et al.*, 2021[60])

3.5.3 Study 3

MDEV inversion

Conventional MRE reconstruction of brain viscoelastic parameters was performed using the 2D MDEV inversion[15,80,81] to generate maps of $|G^*|$ and φ based on

multifrequency wave images[70]. 2D image processing prior to the inversion followed the strategy outlined in Jiang *et al.*[82] and previously applied to brain MRE data by Streitberger *et al.*[83].[61] The complex MRI images were smoothed using a Gaussian filter (width σ = 0.65 voxel).[61] The phase images were then subjected to gradient-based unwrapping, resulting in two in-plane phase gradient images for each encoding direction as described by Papazoglou *et al.*[84].[61] The spatial derivatives additionally suppress compression waves due to their highpass filter properties.[61] As in the *k*-MDEV processing, the FFT was used to provide wave images at each driving frequency.[61] The respective complex-valued images were further subjected to a Butterworth lowpass filter of 1st order with a threshold of 100 m^{-1} to reduce noise and finally invoked by the reconstruction algorithm.[61]
In study 3[61], MDEV is solely used to reconstruct maps of the shear modulus magnitude |*G**| in parallel to the *k*-MDEV inversion.

k-MDEV inversion

The adapted data processing and 2D *k*-MDEV inversion for brain MRE data as developed in study 1[59] was utilized in study 3[61] to calculate maps of *SWS* from reconstructed wavenumbers based on the phase gradient method. In addition, the 3D *k*-MDEV pipeline was used to incorporate the full 3D wave propagation and 3D phase gradient including through-slice components. However, in contrast to Herthum *et al.*[78], the curl field was calculated as a substitute to the highpass filter to suppress longitudinal (compression) waves.[61] The shear modulus magnitude |*G**| was derived from *SWS* values to compare the results with the MDEV inversion. The model equation $|G^*|_{SWS} = SWS^2 \cdot \rho$, with density ρ = 1000 kg/m^3 was applied under the assumption of an elastic material.[61]

3.6 Parameter analysis

3.6.1 Study 1

In study 1[59], the *SWS* dispersion was modelled over the entire frequency range for in vivo data using the Kelvin-Voigt, Maxwell, spring-pot and viscous model. The model parameters were determined by a least-squares algorithm similar to the bi-directional fit described previously.[59] The standard deviations of *SWS* at each frequency was included as weighting factor for the least-squares fit[85].[59] The viscoelastic models for the complex shear modulus $G^* = G' + i \cdot G''$ are given in Table 1. The complex shear modulus was

converted into *SWS* using its magnitude |*G**| and phase angle φ together with eq. (2.12) with density ρ = 1000 kg/m^3.[59]

3.6.2 Study 2

Parameter analysis in study 2[60] was performed by averaging maps of |*G**| and φ over the brain parenchyma. The same ROI was used for each time point, converting the 2D parameter maps into a time series of discrete values for each volunteer.[60] The anatomical T1-weighted images were used to manually delineate ROIs for each subject.[60] Larger sulci and ventricles were removed using thresholds for a minimum time-averaged MRE signal magnitude of 10 and a minimum time-averaged |*G**| value of 950 Pa, as it was done previously in the literature[86].[60] Additionally, single frequency reconstruction of the viscoelastic parameters was performed to test whether simultaneous actuation and evaluation of multiple narrowband frequencies actually increased the stability of the reconstruction.[60] The single frequency inversion was based on the same raw data, but only one frequency was extracted from the discrete Fourier spectrum and used for the inversion.[60] Then the coefficient of variation, CV = (standard deviation / mean), was determined for the baseline phase for each volunteer and experiment for the multi- and single frequency inversion.[60]

For further statistical analysis, the absolute viscoelastic values were averaged over the different experimental phases, given by:

1. Baseline: 2.5 – 22.5 s
2. Established maneuver: 32.5 – 47.5 s
3. Late response maneuver: 52.5 – 57.5 s
4. Recovery: 70 – 80 s[60]

The evaluated phases are visualized in Figure 16. These time intervals were selected based on the study design minus transition phases of 2.5 s at the beginning and end of each phase.[60] An additional late-response phase immediately after the maneuver was included.[60] The breath-hold phase between 25 – 30 s and the transition from VM to recovery (60 – 70 s) were excluded.[60] The average lateral ventricle volume in each phase was also determined.[60] A significant deformation during VM, as it was reported earlier[87], could potentially affect the 2D viscoelastic parameter reconstruction.[60] Hence, automatic segmentations of CSF based on the time averaged MRE magnitude images in each

phase was done with SPM12[75].[60] The number of CSF-associated voxels were calculated by thresholding the probability maps at 0.5.[60]

Moreover, individual viscoelastic differences $\Delta|G^*|(t)$ and $\Delta\varphi(t)$ were quantified by subtracting the averaged values of the baseline phase $|G^*|_{baseline}$ and $\varphi_{baseline}$ from the time courses $|G^*|(t)$ and $\varphi(t)$.[60] Peak changes and temporal delays relative to the onset and end of the VM were determined.[60]

3.6.3 Study 3

In study 3[61], parameter maps of MDEV $|G^*|$, *k*-MDEV $|G^*|_{SWS}$ and T2-weigthed FLAIR intensity ($T2_{int}$) were analyzed for image contrast at different locations with and without focal disease expression. Disease expression (MS lesion) is marked by $T2_{int}$ hyperintensity.[61] Areas without disease expression in NAWM (control regions) were analyzed to better differentiate possible lesion induced tissue alterations from otherwise reconstructed brain heterogeneities.[61] In general, the contrast was determined as:

$$\text{contrast} = \frac{\text{mean}(\text{tissue of interest}) - \text{mean}(\text{reference tissue})}{\text{mean}(\text{reference tissue})} \qquad (3.2)$$

Signal intensities and both stiffness parameters were averaged within ROIs at the site of interest (MS lesion or control region) and at a reference site (surrounding tissue or control region).[61] ROIs at lesion sites were manually drawn.[61] To create ROIs for the control regions, all MS lesions were mirrored to the contralateral hemisphere of the centered parameter maps.[61] Surrounding tissue ROIs were automatically generated as a ring around the central ROI spaced two voxels apart with a thickness of one voxel.[61] CSF, other lesions and solid-fluid interfaces between tissue and CSF (identified by $|G^*|$ values less than 550 Pa[60,86,88]) were excluded from all automatically generated ROIs.[61] Figure 13 illustrates representative masks for MS lesions (red), control regions (blue) and surrounding tissue areas (green and yellow) displayed on an anatomical image slice (FLAIR image). In total, three contrasts were investigated:

- C1: Manually delineated MS lesion tissue versus automatically selected surrounding NAWM.[61]
- C2: Control lesions, i.e., MS lesions mirrored to the contralateral side: NAWM control lesion versus automatically selected surrounding NAWM.[61]

- C3: Manually delineated MS lesions versus control lesions in the contralateral hemisphere.[61]

As MS lesions regularly occur at periventricular locations, where tissue-fluid interfaces could confound the results, the proximity of each lesion to CSF was determined to test as a confounding factor.[61] Therefore, the CSF mask was successively enlarged by one, two, three, four, five and more than five pixels and lesions that matched with the enlarged CSF masks more than 30% were assigned the specific proximity value of one, two, three, four, five or more than five pixels.[61]

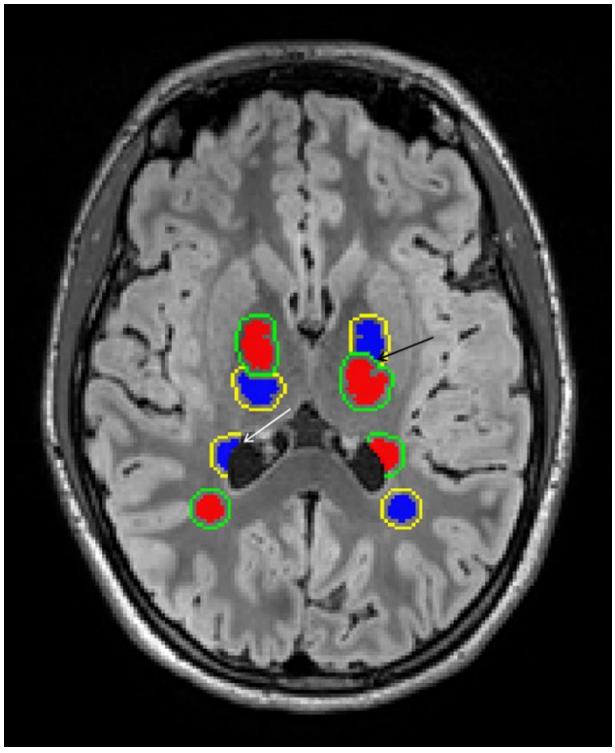

Figure 13: Illustration of possible tissue masks displayed on an anatomical image slice after removing CSF. MS lesions are colored red, automatically assigned surrounding tissue masks are shown in green. Mirrored control regions are shown in blue and their surrounding tissue masks in yellow. The black arrow points to a control region which overlapped by chance with a MS lesion and was therefore reduced in size. The white arrow points to a control region which overlapped by chance with CSF and was consequently reduced in size. (figure from Herthum *et al.*, 2022[61])

3.7 Signal-to-noise ratio of wave images

In all three studies[59-61], the displacement SNR (dSNR) of the wave images was determined. Therefore, the blind noise estimation method of Donoho *et al.*[89] was used to estimate the noise of the complex-valued wavefields based on the wavelet decomposition. Wavelet analysis is well suited to discriminate periodic patterns (spatial frequencies of harmonic waves) in wave images from edges and noise[89,90]. The method has been previously applied to MRE data in the literature[49,71]. Together with the signal magnitude (L2-norm of the wavefield), the dSNR was calculated as follows $dSNR = 20 \cdot \log_{10} \frac{Signal}{Noise}$.[59-61] Signal and noise were summed over all encoding directions and slices, but calculated separately for each frequency. Unless otherwise stated, dSNR was estimated using the same ROI as for the viscoelastic parameter analysis. Moreover, dSNR was evaluated in each MS lesion in study 3[61].

3.8 Statistical tests

All statistical analysis was done in R (version 3.6.2 or higher). P-values less than 0.05 were considered statistically significant.

3.8.1 Study 1

In nine volunteers the experiments were repeated the next day to determine measures of repeatability for in vivo ssMRE.[59] The relative absolute difference (RAD_j) between the two measurements and the coefficient of repeatability (C_R)[91] were calculated based on *SWS* values, which were derived from profile-based wave speed analysis $\overline{c_{1,J}}$ and $\overline{c_{2,J}}$. [59]

$$RAD_j = \frac{2 \cdot \left|\overline{c_{1J}} - \overline{c_{2,J}}\right|}{\left(\overline{c_{1,J}} + \overline{c_{2,J}}\right)} \tag{3.3}$$

$$C_R = 1.96 \cdot \sqrt{\sum_{j=1}^{n} \frac{\left(\overline{c_{1,J}} - \overline{c_{2,J}}\right)^2}{n}} \tag{3.4}$$

Correlation between vibration frequency and dSNR was analyzed using Pearson's correlation coefficient.[59]

3.8.2 Study 2

First, a two-sided paired Welch's t-test was performed to compare the CV during the baseline phase of the multifrequency inversion with the single frequency inversion.[60] Second, the averaged absolute viscoelastic values and the CSF volume were analyzed by group statistics to test for significant changes between the phases 1 – 4.[60] A linear mixed-effects model (LMM) with varying intercepts was used.[60] Viscoelastic parameters and CSF volume were assigned as dependent variables, the individual phases as independent variables and subjects as random effect.[60] Tukey's post hoc test was used to calculate P-values with Bonferroni correction for multiple comparisons.[60] Third, correlation analysis between the viscoelastic parameters and dSNR was performed using a LMM with $|G^*|$ and φ as dependent variables, dSNR as fixed effect and subjects as random effect.[60] At last, a correlation analysis of baseline values of $|G^*|$ and φ with individual peak responses and subject data were performed using Pearson's correlation coefficient.[60]

3.8.3 Study 3

First, a correlation analysis of stiffness contrast C1 and lesion dSNR, CSF proximity and size was done using Pearson's correlation coefficient with Bonferroni correction.[61] Second, a one-sample Welch's t-test was performed for each contrast C1, C2, and C3 and for each parameter $|G^*|$, $|G^*|_{SWS}$ and $T2_{int}$ to determine if the mean of the specific distribution is different from zero.[61] Third, a test for significant differences in $|G^*|$, $|G^*|_{SWS}$ and $T2_{int}$ contrasts was done using a LMM with varying intercepts.[61] Contrasts were used as dependent variables and the tissue type (MS lesion or control region) were assigned independent variable.[61] Random effects were lesion numbers and subjects.[61]

4 Results

4.1 Study 1: Human brain wave speed dispersion

The results of the large-scale wavelength analysis for the in vivo data in terms of *SWS* dispersion over frequency are shown in Figure 14. In addition, values from the literature are displayed. The data was acquired and published by Dittmann *et al.*[62], who used a 3D MDEV inversion on sets of three frequencies. |*G**| results were converted to *SWS* using the equation $= \sqrt{|G|^*/\rho}$, assuming a density ρ = 1000 kg/m^3 and a purely elastic material.[59] The same data was used to recover single-frequency results by Testu *et al.*[92] based on nonlinear inversion methods, yielding storage and loss moduli G' and G'', which were converted to *SWS* using eq. (2.8), (2.9) and (2.12).[59]

Both the spring-pot and Maxwell model converged to the model resembling a purely viscous material when fitted to the profile-based *SWS* dispersion curve.[59] Therefore μ was undetermined, with η = 6.23 ± 0.22 Pa·s based on the viscous model.[59] The two-parameters solid Kelvin-Voigt model also reflected super viscous properties of brain tissue with very low μ (42 ± 13 Pa) and relatively high η (6.57 ± 0.30 Pa·s).[59] The results for the model parameters are summarized in Table 4.

Data consistency for ssMRE was analyzed at 5 and 10 Hz vibration frequency.[59] The relative absolute difference RAD_j between repeated measurements was on average 6.6% with a maximum change of 8.9% in one subject for 5 Hz.[59] At 10 Hz the average RAD_j was 2.8%, with a maximum of 7.8%.[59] The coefficient of repeatability C_R was 0.07 m/s at 5 Hz (mean: 0.52 ± 0.06 m/s) and 0.06 m/s at 10 Hz (mean: 0.79 ± 0.03 m/s).[59] Frequency averaged dSNR was 22 ± 2 dB, which is higher than values from the literature[48,49].[59] No significant correlation with vibration frequency was found (r=.27, p=.45).[59]

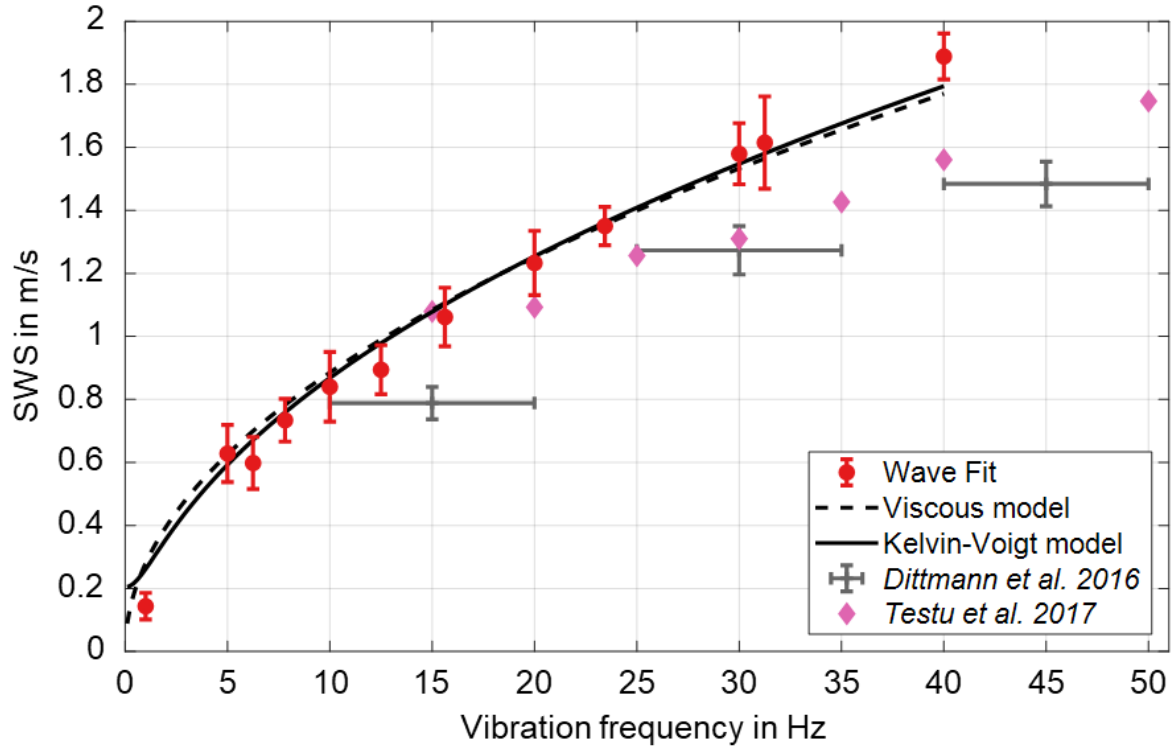

Figure 14: *SWS* dispersion curve over frequency. Wave-fit based *SWS* estimation from intrinsic activated waves to externally induced waves up to 40 Hz. *SWS* dispersion fits using the viscous model (dashed line) and the Kelvin-Voigt model (black thick line) are shown as well. Moreover, data from Dittmann *et al.*[62] and Testu *et al.*[92] were converted to *SWS* and added. (edited figure from Herthum *et al.*, 2021[59])

Table 4: Rheological model parameters (uncertainties given in brackets) based on *SWS* dispersion of profile-based MRE in human brain. (edited table from Herthum *et al.*, 2021[59])

Model	Formula	η in Pa · s	μ in Pa	α
Kelvin-Voigt	$G^* = \mu + i\omega\eta$	6.57 (0.30)	42 (13)	-
Viscous	$G^* = i\omega\eta$	6.23 (0.22)	-	-
Maxwell	$G^* = \frac{\mu \cdot i\omega\eta}{\mu + i\omega\eta}$	converges to viscous		-
Spring-Pot	$G^* = \mu^{1-\alpha}(i\omega\eta)^{\alpha}$	converges to viscous		0.20 (0.02)

4.2 Study 2: Viscoelasticity changes during Valsalva and breath-hold

CV during the baseline phase, averaged over each experiment and subject, was smaller for multifrequency inversion ($CV_{|G^*|}$ = 0.74 ± 0.36%, CV_{φ} = 0.51 ± 0.26%) than for single frequency inversion ($CV_{|G^*|}$ = 0.99 ± 0.50%, CV_{φ} = 0.77 ± 0.41%, p<.001).[60] The heart rate increased steadily in all subjects throughout the VM. This indicated the correct performance of the maneuver. Figure 15 shows representative images of the MRE magnitude, CSF segmentation, |*G**| and φ maps in a single subject averaged over the different time windows. The ROI is indicated by yellow lines. A visible difference from baseline was only evident for |*G**| during the late response phase, which was characterized by slightly increased values.[60] No significant change in CSF-associated voxels was observed.[60] Time courses of the group-averaged relative changes in |*G**| and φ during the three experiments are shown in Figure 16. |*G**| increased by 6.7 ± 4.1% (p<.001) at 2.4 ± 1.2 s after beginning of the VM.[60] The biggest difference was 69 ± 50 Pa.[60] A brief drop in stiffness was followed by a steady increase up to 7.4 ± 2.8% (p<.001) approximately 5.5 ± 2.0 s after the exercise.[60] The largest change to baseline values was 82 ± 42 Pa.[60] During the established maneuver, φ decreased significantly by -2.1 ± 1.4% (p<.001) within an average reduction of -0.018 ± 0.012 rad.[60] Both viscoelastic parameters recovered to baseline values with return to normal breathing.[60] During the BH-in experiment, |*G**| showed two local maxima, the first at 3.0 ± 1.0s after the onset of the VM with an average value of 18 ± 16 Pa (p<.001) and the second at 17.0 ± 2.0 s with 32 ± 29 Pa (p<.001).[60] φ was slightly decreased (-0.006 ± 0.004 rad, p<.001) during the BH-in experiment. During the BH-ex experiment, |*G**| slowly increased with breath holding, reaching its maximum 2.5 ± 1.5 s after finishing the maneuver (26 ± 23 Pa, p<.001).[60] dSNR was on group-average 36 ± 2 dB and changed only slightly during each experiment (±1 dB).[60] No correlations were found between viscoelastic parameters and participant characteristics or dSNR during the experiments.[60]

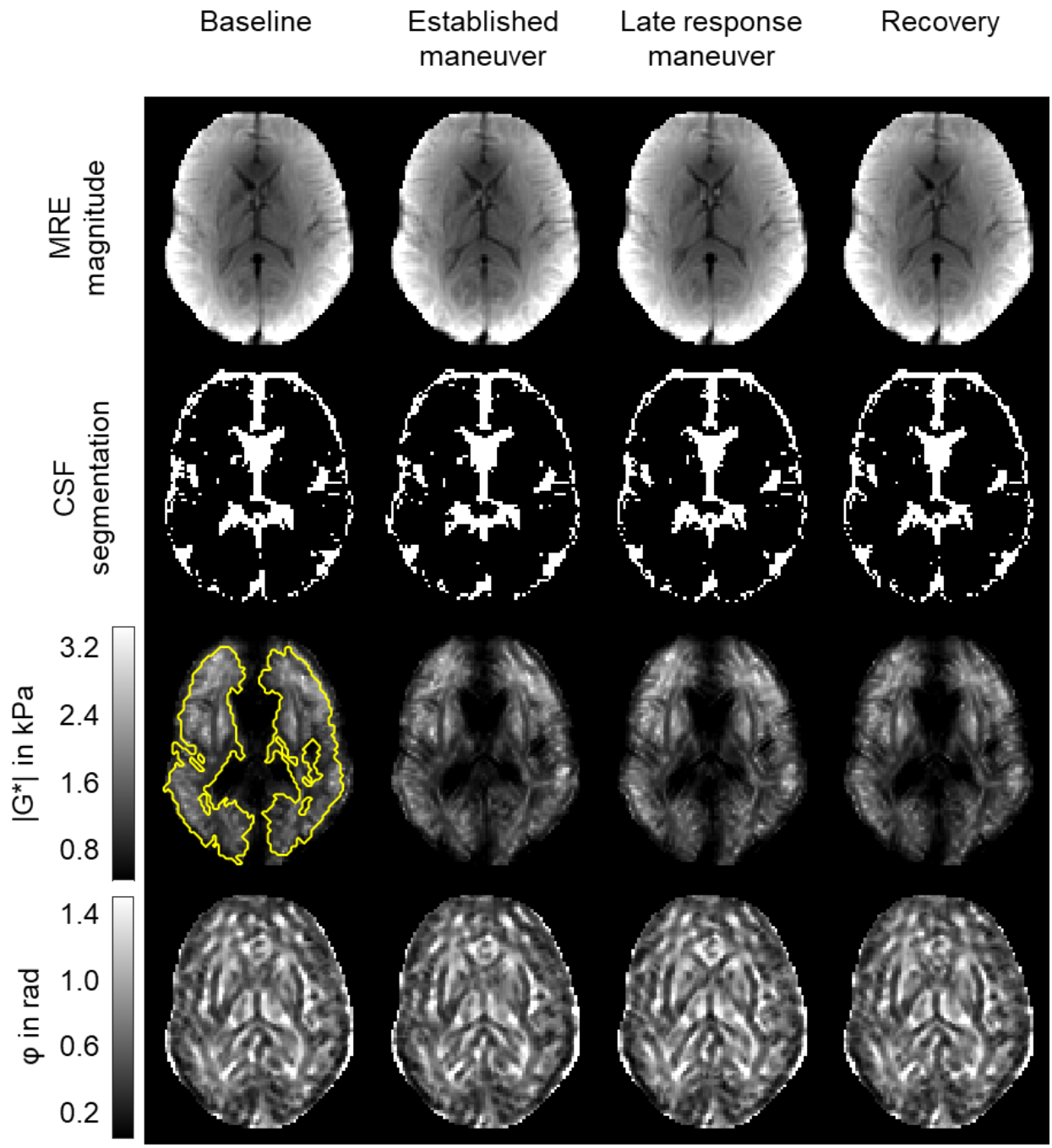

Figure 15: Maps of MRE magnitude, CSF segmentation, |*G**| and *φ* averaged over each experimental phase in one volunteer. White lines indicate the ROI for further data analysis. |*G**| shows a slight increase during the late response maneuver. (edited figure from Herthum *et al.*, 2021[60])

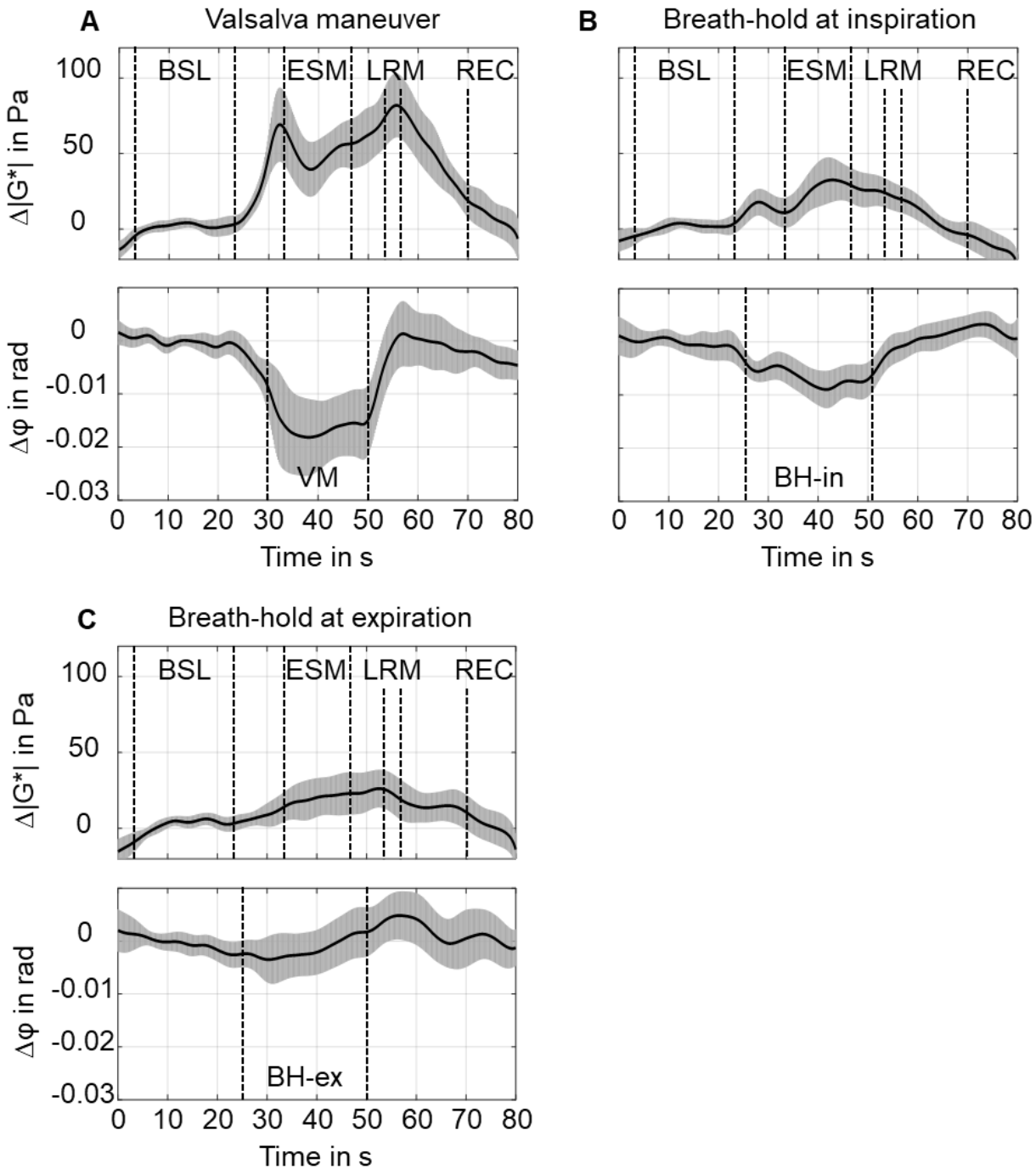

Figure 16: Group-averaged time courses of |*G**| and *φ* changes relative to the baseline values for the three respiratory challenges of Valsalva maneuver (VM), breath-hold at inspiration (BH-in) and breath-hold at expiration (BH-ex). Dashed vertical lines in Δ|*G**| indicate the defined beginning and end of the time windows of baseline (BSL), established maneuver (ESM), late response maneuver (LRM) and recovery (REC). Dashed vertical lines in *φ* indicate beginning and end of the specific exercise. (edited figure from Herthum *et al.*, 2021[60])

4.3 Study 3: Stiffness contrast of multiple sclerosis lesions in humans

In study 3[61], an average of 12 ± 5 (range 7 - 22) lesions per patient were manually delineated. The analysis included in total 147 MS lesions. An average 3D lesion size of 0.38 ± 40 cm^3 (range 0.03 – 2.6 cm^3) was found, corresponding to an idealized spherical lesion with a diameter of 9 mm.[61] Average dSNR in NAWM was 29 ± 3 dB.[61] Figure 17 shows the results in a representative slice in one patient. Masks of the lesion (red) and masks of surrounding tissue (green) are displayed on the co-registered FLAIR-MRI image and MRE magnitude image. MS lesions were hyperintense in both T2-weighted anatomical image contrasts.[61] Control regions (blue) and their respective surrounding tissue (yellow) are visualized on the second MRE magnitude image.[61] The bottom row shows reconstructed parameter maps based on MDEV and *k*-MDEV, showing the contrasts for $|G^*|$, *SWS* and $|G^*|_{SWS}$. MS lesions are not visible in terms of stiffness contrast.[61]

Figure 18 shows the histograms for the three analyzed contrasts for the parameters $|G^*|$ (Figure 18A), $|G^*|_{SWS}$ (Figure 18B) and FLAIR intensity (Figure 18C). The red arrow indicates a registration mismatch between averaged MRE magnitude and FLAIR images. The first contrast (C1) compared MS lesions to surrounding tissue, the second contrast (C2) compared control regions (contralateral NAWM) to surrounding tissue and the third contrast (C3) compared MS lesions to control regions.[61] Descriptive statistics are given in Table 5. The contrast of interest C1 was on average 2.1 ± 11.2%, 80 MS lesions showed higher and 67 lesions showed lower stiffness values than the surrounding tissue.[61] However, similar results (statistically not different, p=.86) were obtained for the control contrast C2 (1.8 ± 11.6%, 76 stiffer and 71 softer), which hindered a differentiation between lesion pathology-induced stiffness alterations and normal WM heterogeneity.[61] Comparison of the MS lesions with the control regions (C3) or analysis of the contrasts in $|G^*|_{SWS}$ yielded similar results.[61] In addition, none of the MS lesions were discernible in the reconstructed $|G^*|$ and $|G^*|_{SWS}$ maps.[61] Delineation of MS lesions by T2-weighted intensities of the FLAIR images showed that MS lesions (C1) yielded significantly higher average contrasts of 30.6 ± 12.1% than the control regions (C2) with 1.8 ± 6.0% (p<.001).[61]

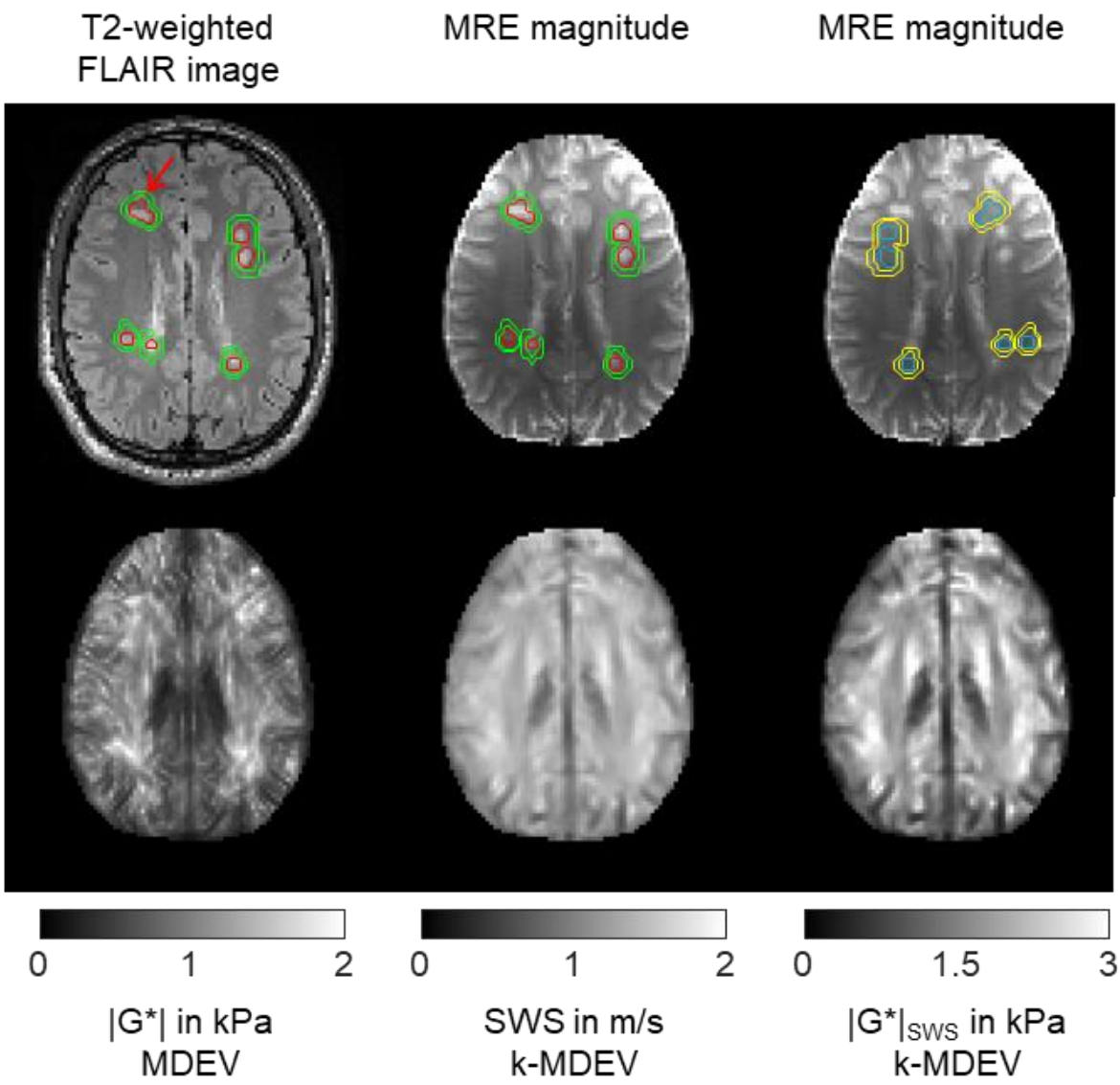

Figure 17: Representative images of T2-weighted FLAIR, MRE magnitude, MDEV based |*G**| and *k*-MDEV based *SWS* and $|G^*|_{SWS}$ for a single subject in the same slice. Manually delineated MS lesion (red) are shown together with automatically generated surrounding tissue masks (green). Control regions (blue) are shown with their respective surrounding tissue (yellow). The red arrow indicates registration mismatch between MRE magnitude and FLAIR images. (edited figure from Herthum *et al.*, 2021[61])

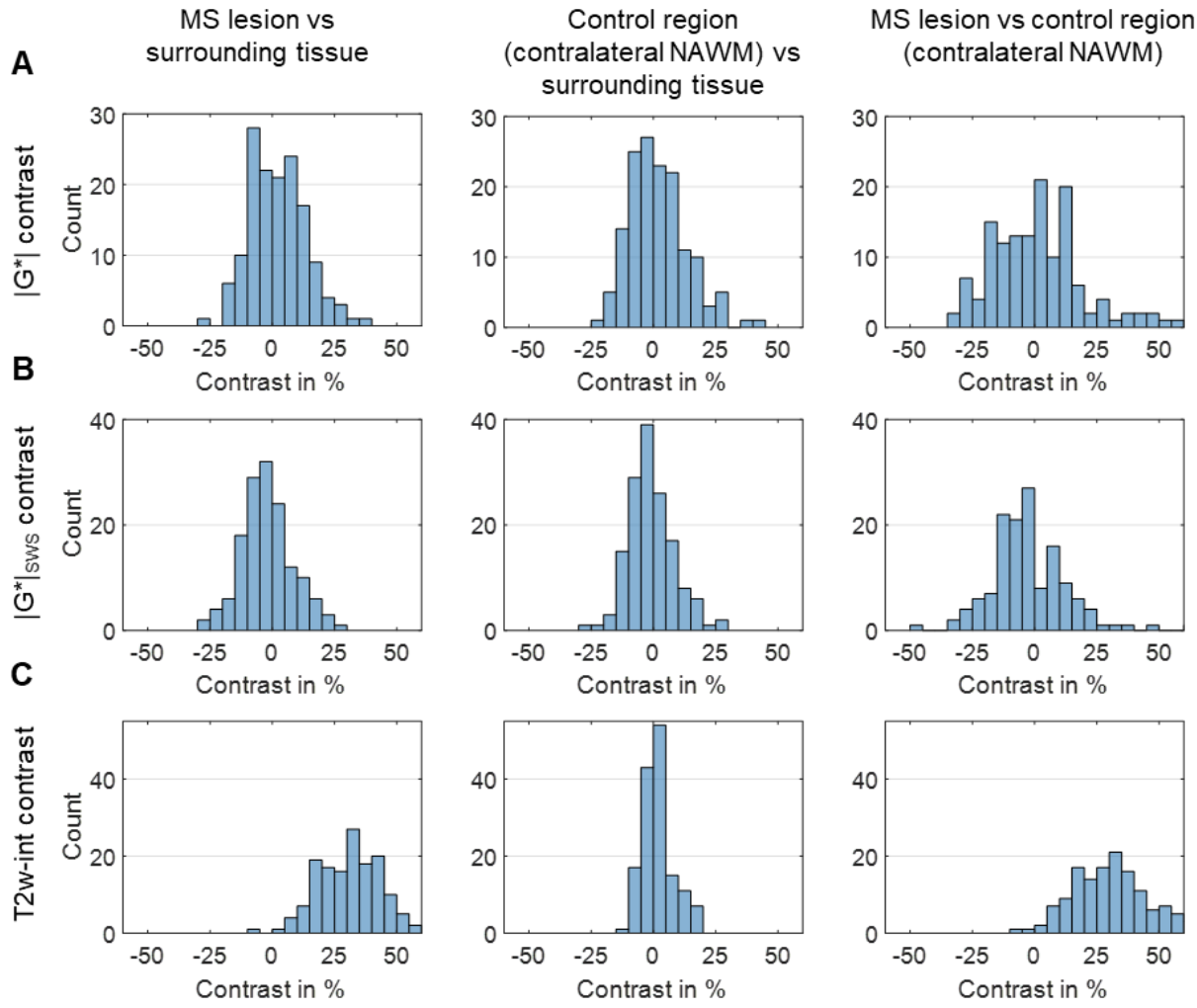

Figure 18: Histograms for different contrasts and parameters. Contrast C1 compares MS lesions with surrounding tissue. Contrast C2 compares control regions in contralateral NAWM with surrounding tissue and contrast C3 compares MS lesions with control regions. **A** Contrasts from MDEV based |*G**|. **B** Contrasts from *k*-MDEV based |*G**|$_{SWS}$. **C** Contrasts from T2-weighted intensity of FLAIR images. (edited figure from Herthum *et al.*, 2021[61])

Table 5: Descriptive statistics for Figure 18 from study 3[61]. Mean values ± standard deviations for different parameters and contrasts are given. In brackets test decision against $H_0 = 0$ and number of positive/negative contrasts. (own table)

	MS lesion vs surrounding tissue	Control region vs surrounding tissue	MS lesion vs control region
$\|G^*\|$ contrast (%)	2.1 ± 11.2 (p=.020, 80/67)	1.8 ± 11.6 (p=.060, 76/71)	1.3 ± 18.4 (p=.130, 78/69)
$\|G^*\|_{SWS}$ contrast (%)	-2.2 ± 10.4 (p=.004, 56/91)	-0.8 ± 9.1 (p=.170, 60/87)	-1.8 ± 16.0 (p=.700, 64/83)
T2w-intensity contrast (%)	30.6 ± 12.1 (p<.001, 146/1)	1.8 ± 6.0 (p=.240, 86/61)	30.7 ± 15.0 (p<.001, 145/2)

5 Discussion

5.1 Summary of results

The methods presented here are the foundation of the conducted studies and contribute to the further development of brain MRE. Exploiting the previously developed ssMRE sequence[49] made it possible for the first time to capture the viscoelastic dispersion of brain tissue from ultra-low frequencies to the conventional range including 1 Hz excitation by intrinsic pulsation.[59] Superviscous brain properties with strong dispersion were found. Combining the rtMRE sequence[50] with multifrequency actuation and adapted data processing improved the robustness of the inversion algorithm.[60] This enabled us to study the previously unknown time-resolved viscoelastic response of in vivo human brain during the Valsalva maneuver and different breath-hold challenges.[60] A perfusion-induced increase in stiffness and decrease in fluidity were observed during VM. Finally, MRE data was acquired with an optimized imaging sequence in a group of RRMS patients to study MS-related mechanical alterations in small lesions.[61] Therefore, *k*-MDEV data processing and stiffness reconstruction in 2D and 3D was redeveloped. No pronounced mechanical differences were detected between MS lesions and surrounding brain tissue beyond NAWM heterogeneity.

5.2 Interpretation of results

Study 1[59] is the first MRE study that used shear waves generated in a wide spectrum of frequencies from heart rate to 40 Hz external actuation in the human brain. Such a wide frequency range has never been used for in vivo brain MR elastography before and revealed a steady increase in *SWS* from 0.14 to 1.9 m/s.[59] Only superviscous tissue properties can explain this large dispersion of stiffness values.[59] Careful analysis of the slope of the propagating intrinsic shear wave that originated from the circle of Willis and traveled through the brain revealed very soft properties in these near-static deformations using intrinsic activation, which was supported by the ex vivo experiments.[59] These results may explain the large gap generally seen between shear stiffness estimates obtained with static and dynamic methods.[59] The viscous model-based viscosity of $\eta = 6.6 \pm 0.3\ Pa \cdot s$ is larger than previously reported values of $\eta = 2.1 \pm 0.4\ Pa \cdot s$ derived from higher frequencies between 25 to 62.5 Hz.[59] However, the results are consistent if we assume brain properties similar to fluids, as reported by Bilston *et*

al.[93].[59] The values thus highlight the importance of fluid-filled spaces such as vessels and pores for whole brain mechanical properties[94,95] that cannot be accounted for by local indentation methods or shear rheometry.[59] Sample preparation for ex vivo methods typically involves some type of fixation, which drains the tissue and leaves clogged blood in the vessels.[59] Therefore, ex vivo methods tend to predominantly capture the contribution of solid compartments, which explains the higher values of 1 – 2 kPa[96] reported in the literature. This is also theoretically predicted by the biphasic tissue model with a varying liquid phase.[97] The large-scale solid-fluid interactions captured by ssMRE at low and ultra-low frequencies may thus have the potential to serve as a future biomarker in clinical practice.[59] The tissue viscosity determined by dispersion analysis, including ultra-low frequencies, might reveal viscoelastic network modulations of brain tissue in inflammation and ECM remodeling.[59]

In study 2[60], the novel rtMRE technique[50] was used to image fast changes in human brain viscoelasticity in response to the VM and various breath-hold challenges.[60] Multifrequency actuation increased the consistency of mechanical parameter reconstruction without additional scan time, and all subjects consistently showed an increase in $|G^*|$ and a decrease in fluidity-related φ during VM.[60] The observed mechanical alterations may be attributable to brain perfusion and physiological processes induced by VM.[60] Figure 19 shows representative time courses of the heart rate and mean arterial blood pressure with additional plots for stiffness-related $|G^*|$ and fluidity-related loss angle φ. Subjects initiated the VM by abdominal muscle contraction to compress the lung volume against a closed mouth during breath-hold at deep inspiration.[60,65] In general, if the maneuver is performed correctly, intrathoracic pressure increases immediately and venous return to the heart is impeded.[60,98,99] The pressure rise is transmitted to the brain cavity through the vascular tree and elevates ICP.[60,100] Simultaneously, arterial blood pressure (ABP) and cerebral blood flow (CBF) are reduced and blood accumulates in the brain.[60,101] This in turn activates cerebral autoregulation, which aims to normalize CBF by dilating the cerebral arteries and reducing vascular resistance.[60,101,102] All subjects in the experiment showed a steady increase in heart rate to normalize ABP, which is commonly mediated by the baroreflex.[60,101,102]

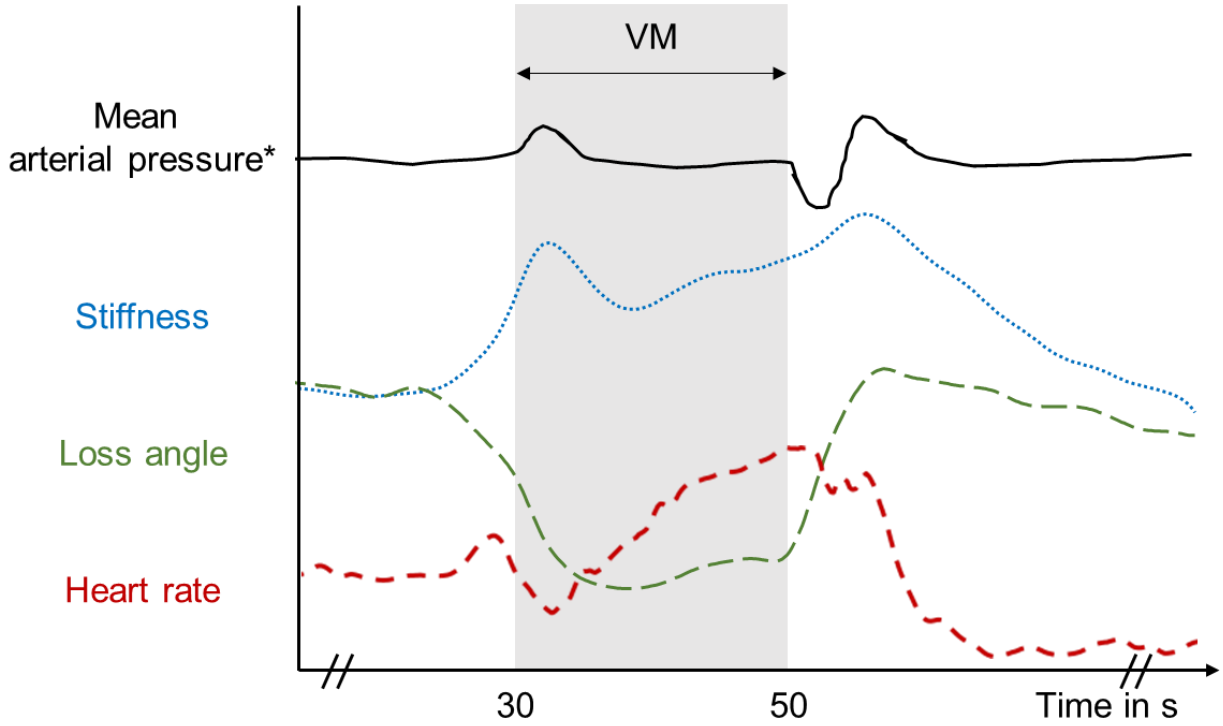

Figure 19: Schematic time courses of average stiffness and loss angle before, meanwhile and past the Valsalva maneuver inspiration as conducted and quantified in this study. In addition, mean arterial pressure variations as reported by Pstras *et al.*[103] and group mean heart rate changes measured in this study are given. (figure from Herthum *et al.*, 2021[60])

Interestingly, stiffness correlated with the increase in ICP and rose steadily throughout the VM.[60] This relationship is an intriguing finding because the observed changes may be indirectly linked to tissue stiffness, and ICP could be monitored with rtMRE.[60] Direct noninvasive ICP measurement is not yet possible, and understanding how a pathologically elevated ICP is related to whole brain stiffness is of interest for clinical purposes in patients with brain tumors or hematomas, hydrocephalus, and other conditions.[60] Fluidity followed the reduced cerebral perfusion, as viscous damping decreased with the drop in perfusion.[60] Physiologically driven alterations in φ have been previously studied by our group, and an increase of 2% was observed with hypercapnia[104] and of 0.5% with arterial pulsation[49].[60] In both cases, perfusion pressure and CBF were increased, supporting the findings of reduced fluidity with unchanged CBF and lowered perfusion pressure.[60] The baseline values measured in this study agree well with previously reported results obtained at similar frequencies.[36,49,105] The findings were corroborated by control experiments investigating breath-holds without VM.[60] Slight modulations similar to those induced by VM were observed for the BH-in control

experiment, as intrathoracic pressure is also likely to be elevated during full inspiration.[60] The least effect on brain viscoelasticity was observed during the BH-ex maneuver.[60] Analysis of CSF volume and ventricle size revealed no significant correlations with VM.[60] Therefore, the previously reported changes in ventricle volume in the range of 20%[87,106] were successfully avoided by instructing subjects to perform a moderate maneuver with minimization of muscle strain and head motion.[60] The reported time course of brain viscoelasticity in healthy subjects may serve as a baseline for the VM response.[60] This may be valuable for studying neurological dysfunction of autoregulation.[60]

To my knowledge, study 3[61] is the first analysis that relates the stiffness contrast of MS lesions derived from MRE to NAWM heterogeneity. The high complexity of brain tissue results in a wide variety of reported stiffness estimates, and MRE parameter maps of human brain tissue regularly appear very heterogeneous.[61] Thus, it is generally challenging to discriminate effects of small features.[61] To address this issue, the following measures were determined:

i. relative difference between lesion and surrounding tissue (lesion contrast)[61]
ii. relative difference between contralateral control regions and surrounding tissue (control tissue or MRE heterogeneity)[61]
iii. relative difference between lesion tissue and control regions[61]

MDEV reconstruction showed 54% and 46% lesions to exhibit higher and lower stiffness values than surrounding tissue, respectively.[61] However, control tissue analysis revealed a similar pattern of mechanical contrasts.[61] While the first finding alone might suggest that there is a lesion-dependent alteration in stiffness due to varying lesion status or pathology, the fact that similar contrasts occurred in control tissue indicates that the findings fall within the observed NAWM heterogeneity and thus, there is no evidence for a systematic pattern.[61] No lesion was visually apparent compared to the contralateral side.[61] Hotspots, or high-intensity areas, occur regularly in MRE maps due to wave reflections at tissue boundaries, which presents a further obstacle for mechanical delineation of MS lesions using MRE.[61] Still, the NAWM values are within the range of those reported in the literature.[61] The quantity of viscoelastic parameters obtained by MDEV direct inversion were lower than those obtained with *k*-MDEV, as first-order FDO inversions are less biased by noise effects.[61,73] Yet, MDEV is more firmly established for brain MRE, so both approaches were analyzed here. In simulations, both methods

performed better in resolving soft inclusions.[61] As described by Mura *et al.*[73], SNR and spatial support are the driving factors that seem to be better matched in larger and softer areas.[61] Stiffer and smaller inclusions showed severe inversion bias.[61]

As the mechanical environment of demyelinated lesions appears to be important for the remyelination process[107], existing ex vivo studies used atomic force and scanning force microscopy to examine microscopic stiffness alterations associated with MS lesions in tissue samples.[108,109] Mechanical alterations in MS have been attributed to glial cells and ECM composition, as myelin content may not be the sole cause.[107] ECM remodeling in chronic lesions has been found to be driven by reactive astrocytes and fibronectin accumulation, which has been associated with sclerosis or stiffening.[108,110] Conversely, demyelination with inflammation and gliosis has been associated with lesion softening, as glial cells were measured to be softer than neurons.[67,111] The study presented here did not reveal that these microscopic findings are expressed as marked macroscopic stiffness changes for in vivo lesions.[61] Overall, only relatively small contrasts were observed, compared with an overall brain stiffness reduction of about 15 – 20% in MS patients or compared with findings in prostate tumors with stiffness contrasts of up to 140%.[68,112] All patients were on immunomodulatory treatment, with the last relapse months or years before the study.[61] Accordingly, it was hypothesized that most lesions were chronic and possibly stiffer.[61] However, this group of lesions is very difficult to detect because stiffer contrasts are largely underestimated, as shown in the simulations, although it is theoretically possible to resolve small inclusions with different contrasts.[61] Moreover, most lesions were small and periventricular in location, where tissue-fluid boundaries present an additional hurdle.[61] Still, proximity to CSF was ruled out as a confounding factor, and also larger lesions did not show consistent contrast patterns.[61] Additional analysis using full 3D *k*-MDEV inversion, which accounts for complex wave patterns, did not yield results different from those discussed earlier.[61] In light of these findings, it can be concluded "… that marked tissue sclerosis may not be a mechanical signature of MS."[61].

5.3 Limitations

Although all three studies[59-61] were conducted with great care, there are limitations that need to be mentioned. First, there are no 'ground truth' values for brain viscoelasticity in humans.[59] Second, a relatively small number of participants was included, in part

because of the exploratory nature of the studies. Nevertheless, 147 lesion were delineated for study 3[61], which provided sufficient statistical power, assuming that different lesion types may be present in a single subject. Third, the single-slice reconstructions generated in study 1[59] and study 2[60] are possibly biased because obliquely travelling shear waves and compression wave components cannot be accounted for in 1D and 2D data analysis.[59,60] In general, shear wave propagation is heterogeneous and dispersive due to anisotropic and nonlinear tissue properties, and even 3D techniques, as employed in study 3[61] or other studies, cannot fully address these issues.[60,61] Another limitation for study 3[61] was that lesion activity could not be assessed with gadolinium-based contrast agent-enhanced MRI because this was not approved by the local ethics committee. Technical advancements with regard to actuation systems, imaging sequences[113-115], and inversion algorithms[88,116,117] may address these interesting challenges and will probably contribute significantly to the future developments in MRE and its clinical implementation.

5.4 Future research topics

The work presented here shows a high degree of novelty in all three studies performed[59-61], as each study sheds light on a research question that has not been addressed before. Consequently, there exist no comparable studies, and it is important that the findings are replicated and confirmed to provide reliable scientific evidence. Since study 1[59] and study 2[60] were performed in healthy participants, it would be interesting to conduct similar studies in patients and compare the findings with the healthy references presented here. As mentioned earlier, ultra-low frequencies might be suitable for studying matrix and fluid accumulation, which can be a sensitive marker in inflammation and ECM remodeling. Similarly, the viscoelastic response to the Valsalva maneuver could be sensitive to pathologies related to increased ICP or cerebral autoregulation. A highly interesting continuation of study 3[61] would be to evaluate mechanical alterations in relation to MS lesion activity. In particular, acute and active MS lesions are worth studying, as it has recently been shown that acute inflammation reduces tissue stiffness in an EAE mouse model.[118] Incorporating the MRE experiment into a clinical routine protocol for the initial diagnosis of MS in subjects with a clinically isolated syndrome would have several advantages. The routine protocol includes contrast-enhanced MRI, which is required for differentiation of active lesions. In addition, once the diagnosis has been established,

patients regularly return for follow-up examinations, allowing serial investigation of stiffness changes over time and correlation with treatment outcome.

Moreover, the methods developed can be used to answer other research questions of interest to the scientific community. Multifrequency rtMRE is a robust technique for mapping rapid mechanical variations. In a future study, this method could be used to image viscoelastic alterations in the brain induced by functional processes, as proposed by Lan *et al.*[37]. In contrast to their study, rtMRE allows higher frame rates, which are required to distinguish the potentially rapid mechanical response from a slower contrast dependent on blood oxygenation.[60] The developed technique of MRE at ultra-low frequencies opens many doors for future work, including artificial intelligence based wave image analysis. It is important to overcome profile-based, large scale stiffness estimation and to generate high-resolution maps of tissue stiffness and fluidity at ultra-low frequencies instead. AI-based viscoelastic dispersion analysis for tissue fluidity in disease-related ECM modulation is an exciting new research area that complements the initial findings presented here. This may help us to understand the role of brain structure in inflammatory and regenerative processes.

6 Conclusion

The in vivo viscoelastic properties of human brain tissue play a crucial role in health and disease and contribute to both tissue structure and function.[4] Human brain tissue is inherently inaccessible to surface-based mechanical testing methods such as palpation or local indentation techniques.[4] Any invasive approach bears risks for patients, and their use should be reduced as much as possible in clinical routine. Allowing quantification of viscoelastic tissue properties, brain MRE has a great potential to replace invasive procedures. Furthermore, viscoelasticity can be explored as a potential biomarker for pathologies, such as tumors, that affect the brain's mechanical structure. The sensitivity of brain mechanical measurement to solid-fluid interactions (CSF, blood), viscoelastic network interactions (neurons, oligodendrocytes, astrocytes), and viscoelastic damping (ECM remodeling) can be exploited for a variety of diagnostic and therapeutic applications. Nevertheless, as an emerging imaging modality, brain MRE also presents many challenges that need to be addressed by the scientific community to move the technique towards clinical application. All three studies presented here contribute to this task by exploring frequency regimes outside the conventional range[59], by applying recently developed rtMRE to test brain function in terms of viscoelasticity at high temporal resolution[60], and by investigating the limitations of spatial resolution and contrasts of brain MRE in detecting possible focal stiffness alterations in MS lesions[61].

The first study[59] explored frequencies outside the conventional range and successfully introduced intrinsically activated MRE using the pulse wave as the source of shear wave propagation. Probing brain tissue at such ultra-low frequencies revealed the superviscous properties of brain tissue at large scales, bridging the gap between static and dynamic measurement modalities.[59] The extended dispersion range may be sensitive to altered tissue fluidity, which affects the viscoelastic dispersion studied here.[59]

The second study[60] investigated healthy brain tissue under physiological challenges induced by the Valsalva maneuver and linked the observed brain stiffening to cardiovascular mechanisms. Quantification of viscoelastic changes at high temporal resolution without gating is an emerging branch within brain MRE and was first made possible by the previously developed imaging sequences of rtMRE[50].[60] The sequence was tailored to simultaneous multifrequency wave excitation, which increased the robustness of the inversion algorithm and allowed us to consistently observe relatively small viscoelasticity changes on short time scales in a group of healthy subjects.[60]

The third study[61] aimed at resolving small focal viscoelastic alterations possibly induced by MS lesions while taking NAWM heterogeneity into account. However, no such variations could be detected as the contralateral side exhibited local stiffness contrasts of the same magnitude.[61] Therefore, it was not possible to distinguish the observed stiffness changes in MS lesions from NAWM heterogeneity.[61] Though, simulations and phantom experiments allowed to set detection limits for small stiffness contrasts and constrained the mechanical modulations that might be induced in MS lesions.[61] This rigorous analysis suggests that tissue sclerosis is not a marked feature of MS lesions in RRMS patients and also points to the current challenges of brain MRE in terms of spatial resolution and detectability of stiffness contrasts.[61]

In summary, this dissertation contributes to the field of brain MRE by developing and validating new methods and by exploring unanswered research questions with state-of-the-art technology. This opens new possibilities for future studies. Each study was accompanied by technical and methodological advances in each major component of MRE examinations: actuation, imaging, and reconstruction. The limits of MRE have been pushed and the challenges of ultra-low frequency MRE[59], high temporal resolution[60], and high spatial resolution[61] have been tested. Each of the three studies contributes to the clinical translation of human brain MRE as a new imaging modality for assessing viscoelasticity as a quantitative biomarker in the in vivo examination of biological soft tissues.

References

1 Fung, Y.-c. *Biomechanics: mechanical properties of living tissues*. (Springer Science & Business Media, 2013).

2 Ambrosi, D., Ben Amar, M., Cyron, C. J., DeSimone, A., Goriely, A., Humphrey, J. D. & Kuhl, E. Growth and remodelling of living tissues: perspectives, challenges and opportunities. *J R Soc Interface* **16**, 20190233 (2019).

3 Barnes, J. M., Przybyla, L. & Weaver, V. M. Tissue mechanics regulate brain development, homeostasis and disease. *J Cell Sci* **130**, 71-82 (2017).

4 Hirsch, S., Braun, J. & Sack, I. *Magnetic Resonance Elastography: Physical Background And Medical Applications*. (Wiley-VCH, 2017).

5 Reichert, B. & Stelzenmüller, W. *Palpation techniques: surface anatomy for physical therapists*. (Thieme New York, NY, 2011).

6 Wells, R. G. Tissue mechanics and fibrosis. *Biochim Biophys Acta* **1832**, 884-890 (2013).

7 Singh, S., Fujii, L. L., Murad, M. H., Wang, Z., Asrani, S. K., Ehman, R. L., Kamath, P. S. & Talwalkar, J. A. Liver stiffness is associated with risk of decompensation, liver cancer, and death in patients with chronic liver diseases: a systematic review and meta-analysis. *Clin Gastroenterol Hepatol* **11**, 1573-1584 e1571-1572; quiz e1588-1579 (2013).

8 Hiscox, L. V., Johnson, C. L., Barnhill, E., McGarry, M. D., Huston, J., van Beek, E. J., Starr, J. M. & Roberts, N. Magnetic resonance elastography (MRE) of the human brain: technique, findings and clinical applications. *Phys Med Biol* **61**, R401-R437 (2016).

9 Muthupillai, R., Lomas, D. J., Rossman, P. J., Greenleaf, J. F., Manduca, A. & Ehman, R. L. Magnetic resonance elastography by direct visualization of propagating acoustic strain waves. *Science* **269**, 1854-1857 (1995).

10 Aponte Ortiz, J. A., Konik, E., Eckert, E. C., Pepin, K. M. & Greenberg-Worisek, A. Premarket Approval Through the 510(k) Process: Lessons from the Translation Process of Magnetic Resonance Elastography. *Clin Transl Sci* **11**, 447-449 (2018).

11 Serai, S. D., Obuchowski, N. A., Venkatesh, S. K., Sirlin, C. B., Miller, F. H., Ashton, E., Cole, P. E. & Ehman, R. L. Repeatability of MR Elastography of Liver: A Meta-Analysis. *Radiology* **285**, 92-100 (2017).

12 Fung, Y. *Biomechanics: mechanical properties of living tissue*. (Springer-Verlag, 1993).

13 Yin, Z., Romano, A. J., Manduca, A., Ehman, R. L. & Huston, J., 3rd. Stiffness and Beyond: What MR Elastography Can Tell Us About Brain Structure and Function Under Physiologic and Pathologic Conditions. *Top Magn Reson Imaging* **27**, 305-318 (2018).

14 Murphy, M. C., Huston, J., 3rd & Ehman, R. L. MR elastography of the brain and its application in neurological diseases. *Neuroimage* **187**, 176-183 (2019).

15 Guo, J., Hirsch, S., Fehlner, A., Papazoglou, S., Scheel, M., Braun, J. & Sack, I. Towards an elastographic atlas of brain anatomy. *PLoS One* **8**, e71807 (2013).

16 Hiscox, L. V., McGarry, M. D. J., Schwarb, H., Van Houten, E. E. W., Pohlig, R. T., Roberts, N., Huesmann, G. R., Burzynska, A. Z., Sutton, B. P., Hillman, C. H., Kramer, A. F., Cohen, N. J., Barbey, A. K., Paulsen, K. D. & Johnson, C. L. Standard-space atlas of the viscoelastic properties of the human brain. *Hum Brain Mapp* **41**, 5282-5300 (2020).

17 Johnson, C. L., Schwarb, H., M, D. J. M., Anderson, A. T., Huesmann, G. R., Sutton, B. P. & Cohen, N. J. Viscoelasticity of subcortical gray matter structures. *Hum Brain Mapp* **37**, 4221-4233 (2016).
18 McIlvain, G., Schwarb, H., Cohen, N. J., Telzer, E. H. & Johnson, C. L. Mechanical properties of the in vivo adolescent human brain. *Dev Cogn Neurosci* **34**, 27-33 (2018).
19 Johnson, C. L., McGarry, M. D., Gharibans, A. A., Weaver, J. B., Paulsen, K. D., Wang, H., Olivero, W. C., Sutton, B. P. & Georgiadis, J. G. Local mechanical properties of white matter structures in the human brain. *Neuroimage* **79**, 145-152 (2013).
20 Hiscox, L. V., Johnson, C. L., McGarry, M. D. J., Perrins, M., Littlejohn, A., van Beek, E. J. R., Roberts, N. & Starr, J. M. High-resolution magnetic resonance elastography reveals differences in subcortical gray matter viscoelasticity between young and healthy older adults. *Neurobiol Aging* **65**, 158-167 (2018).
21 Hiscox, L. V., Schwarb, H., McGarry, M. D. J. & Johnson, C. L. Aging brain mechanics: Progress and promise of magnetic resonance elastography. *Neuroimage* **232**, 117889 (2021).
22 Sack, I., Beierbach, B., Wuerfel, J., Klatt, D., Hamhaber, U., Papazoglou, S., Martus, P. & Braun, J. The impact of aging and gender on brain viscoelasticity. *Neuroimage* **46**, 652-657 (2009).
23 Arani, A., Murphy, M. C., Glaser, K. J., Manduca, A., Lake, D. S., Kruse, S. A., Jack, C. R., Jr., Ehman, R. L. & Huston, J., 3rd. Measuring the effects of aging and sex on regional brain stiffness with MR elastography in healthy older adults. *Neuroimage* **111**, 59-64 (2015).
24 Lipp, A., Trbojevic, R., Paul, F., Fehlner, A., Hirsch, S., Scheel, M., Noack, C., Braun, J. & Sack, I. Cerebral magnetic resonance elastography in supranuclear palsy and idiopathic Parkinson's disease. *Neuroimage Clin* **3**, 381-387 (2013).
25 Lipp, A., Skowronek, C., Fehlner, A., Streitberger, K. J., Braun, J. & Sack, I. Progressive supranuclear palsy and idiopathic Parkinson's disease are associated with local reduction of in vivo brain viscoelasticity. *Eur Radiol* **28**, 3347-3354 (2018).
26 Hiscox, L. V., Johnson, C. L., McGarry, M. D. J., Marshall, H., Ritchie, C. W., van Beek, E. J. R., Roberts, N. & Starr, J. M. Mechanical property alterations across the cerebral cortex due to Alzheimer's disease. *Brain Commun* **2**, fcz049 (2020).
27 Murphy, M. C., Huston, J., 3rd, Jack, C. R., Jr., Glaser, K. J., Manduca, A., Felmlee, J. P. & Ehman, R. L. Decreased brain stiffness in Alzheimer's disease determined by magnetic resonance elastography. *J Magn Reson Imaging* **34**, 494-498 (2011).
28 Murphy, M. C., Jones, D. T., Jack, C. R., Jr., Glaser, K. J., Senjem, M. L., Manduca, A., Felmlee, J. P., Carter, R. E., Ehman, R. L. & Huston, J., 3rd. Regional brain stiffness changes across the Alzheimer's disease spectrum. *Neuroimage Clin* **10**, 283-290 (2016).
29 Wuerfel, J., Paul, F., Beierbach, B., Hamhaber, U., Klatt, D., Papazoglou, S., Zipp, F., Martus, P., Braun, J. & Sack, I. MR-elastography reveals degradation of tissue integrity in multiple sclerosis. *Neuroimage* **49**, 2520-2525 (2010).
30 Fehlner, A., Behrens, J. R., Streitberger, K. J., Papazoglou, S., Braun, J., Bellmann-Strobl, J., Ruprecht, K., Paul, F., Wurfel, J. & Sack, I. Higher-resolution MR elastography reveals early mechanical signatures of neuroinflammation in patients with clinically isolated syndrome. *J Magn Reson Imaging* **44**, 51-58 (2016).

31 Streitberger, K. J., Wiener, E., Hoffmann, J., Freimann, F. B., Klatt, D., Braun, J., Lin, K., McLaughlin, J., Sprung, C., Klingebiel, R. & Sack, I. In vivo viscoelastic properties of the brain in normal pressure hydrocephalus. *NMR Biomed* **24**, 385-392 (2011).

32 Murphy, M. C., Cogswell, P. M., Trzasko, J. D., Manduca, A., Senjem, M. L., Meyer, F. B., Ehman, R. L. & Huston, J., 3rd. Identification of Normal Pressure Hydrocephalus by Disease-Specific Patterns of Brain Stiffness and Damping Ratio. *Invest Radiol* **55**, 200-208 (2020).

33 Aunan-Diop, J. S., Pedersen, C. B., Halle, B., Jensen, U., Munthe, S., Harbo, F., Johannsson, B. & Poulsen, F. R. Magnetic resonance elastography in normal pressure hydrocephalus-a scoping review. *Neurosurg Rev* (2021).

34 Hatt, A., Cheng, S., Tan, K., Sinkus, R. & Bilston, L. E. MR Elastography Can Be Used to Measure Brain Stiffness Changes as a Result of Altered Cranial Venous Drainage During Jugular Compression. *AJNR Am J Neuroradiol* **36**, 1971-1977 (2015).

35 Arani, A., Min, H. K., Fattahi, N., Wetjen, N. M., Trzasko, J. D., Manduca, A., Jack, C. R., Jr., Lee, K. H., Ehman, R. L. & Huston, J., 3rd. Acute pressure changes in the brain are correlated with MR elastography stiffness measurements: initial feasibility in an in vivo large animal model. *Magn Reson Med* **79**, 1043-1051 (2018).

36 Hetzer, S., Birr, P., Fehlner, A., Hirsch, S., Dittmann, F., Barnhill, E., Braun, J. & Sack, I. Perfusion alters stiffness of deep gray matter. *J Cereb Blood Flow Metab* **38**, 116-125 (2018).

37 Lan, P. S., Glaser, K. J., Ehman, R. L. & Glover, G. H. Imaging brain function with simultaneous BOLD and viscoelasticity contrast: fMRI/fMRE. *Neuroimage* **211**, 116592 (2020).

38 Bunevicius, A., Schregel, K., Sinkus, R., Golby, A. & Patz, S. REVIEW: MR elastography of brain tumors. *Neuroimage Clin* **25**, 102109 (2020).

39 Reiss-Zimmermann, M., Streitberger, K. J., Sack, I., Braun, J., Arlt, F., Fritzsch, D. & Hoffmann, K. T. High Resolution Imaging of Viscoelastic Properties of Intracranial Tumours by Multi-Frequency Magnetic Resonance Elastography. *Clin Neuroradiol* **25**, 371-378 (2015).

40 Schregel, K., Wuerfel, E., Garteiser, P., Gemeinhardt, I., Prozorovski, T., Aktas, O., Merz, H., Petersen, D., Wuerfel, J. & Sinkus, R. Demyelination reduces brain parenchymal stiffness quantified in vivo by magnetic resonance elastography. *Proc Natl Acad Sci U S A* **109**, 6650-6655 (2012).

41 Riek, K., Millward, J. M., Hamann, I., Mueller, S., Pfueller, C. F., Paul, F., Braun, J., Infante-Duarte, C. & Sack, I. Magnetic resonance elastography reveals altered brain viscoelasticity in experimental autoimmune encephalomyelitis. *Neuroimage Clin* **1**, 81-90 (2012).

42 Wang, S., Millward, J. M., Hanke-Vela, L., Malla, B., Pilch, K., Gil-Infante, A., Waiczies, S., Mueller, S., Boehm-Sturm, P., Guo, J., Sack, I. & Infante-Duarte, C. MR Elastography-Based Assessment of Matrix Remodeling at Lesion Sites Associated With Clinical Severity in a Model of Multiple Sclerosis. *Front Neurol* **10**, 1382 (2019).

43 Murphy, M. C., Curran, G. L., Glaser, K. J., Rossman, P. J., Huston, J., 3rd, Poduslo, J. F., Jack, C. R., Jr., Felmlee, J. P. & Ehman, R. L. Magnetic resonance elastography of the brain in a mouse model of Alzheimer's disease: initial results. *Magn Reson Imaging* **30**, 535-539 (2012).

44 Munder, T., Pfeffer, A., Schreyer, S., Guo, J., Braun, J., Sack, I., Steiner, B. & Klein, C. MR elastography detection of early viscoelastic response of the murine hippocampus to amyloid beta accumulation and neuronal cell loss due to Alzheimer's disease. *J Magn Reson Imaging* **47**, 105-114 (2018).

45 Patz, S., Fovargue, D., Schregel, K., Nazari, N., Palotai, M., Barbone, P. E., Fabry, B., Hammers, A., Holm, S., Kozerke, S., Nordsletten, D. & Sinkus, R. Imaging localized neuronal activity at fast time scales through biomechanics. *Sci Adv* **5**, eaav3816 (2019).

46 Guo, J., Bertalan, G., Meierhofer, D., Klein, C., Schreyer, S., Steiner, B., Wang, S., Vieira da Silva, R., Infante-Duarte, C., Koch, S., Boehm-Sturm, P., Braun, J. & Sack, I. Brain maturation is associated with increasing tissue stiffness and decreasing tissue fluidity. *Acta Biomater* **99**, 433-442 (2019).

47 Bertalan, G., Boehm-Sturm, P., Schreyer, S., Morr, A. S., Steiner, B., Tzschatzsch, H., Braun, J., Guo, J. & Sack, I. The influence of body temperature on tissue stiffness, blood perfusion, and water diffusion in the mouse brain. *Acta Biomater* **96**, 412-420 (2019).

48 Bertalan, G., Klein, C., Schreyer, S., Steiner, B., Kreft, B., Tzschatzsch, H., de Schellenberger, A. A., Nieminen-Kelha, M., Braun, J., Guo, J. & Sack, I. Biomechanical properties of the hypoxic and dying brain quantified by magnetic resonance elastography. *Acta Biomater* **101**, 395-402 (2020).

49 Schrank, F., Warmuth, C., Tzschatzsch, H., Kreft, B., Hirsch, S., Braun, J., Elgeti, T. & Sack, I. Cardiac-gated steady-state multifrequency magnetic resonance elastography of the brain: Effect of cerebral arterial pulsation on brain viscoelasticity. *J Cereb Blood Flow Metab* **40**, 991-1001 (2020).

50 Schrank, F., Warmuth, C., Gorner, S., Meyer, T., Tzschatzsch, H., Guo, J., Uca, Y. O., Elgeti, T., Braun, J. & Sack, I. Real-time MR elastography for viscoelasticity quantification in skeletal muscle during dynamic exercises. *Magn Reson Med* **84**, 103-114 (2020).

51 Peng, X., Sui, Y., Trzasko, J. D., Glaser, K. J., Huston, J., 3rd, Ehman, R. L. & Pipe, J. G. Fast 3D MR elastography of the whole brain using spiral staircase: Data acquisition, image reconstruction, and joint deblurring. *Magn Reson Med* **86**, 2011-2024 (2021).

52 Palmeri, M. L., Milkowski, A., Barr, R., Carson, P., Couade, M., Chen, J., Chen, S., Dhyani, M., Ehman, R., Garra, B., Gee, A., Guenette, G., Hah, Z., Lynch, T., Macdonald, M., Managuli, R., Miette, V., Nightingale, K. R., Obuchowski, N., Rouze, N. C., Morris, D. C., Fielding, S., Deng, Y., Chan, D., Choudhury, K., Yang, S., Samir, A. E., Shamdasani, V., Urban, M., Wear, K., Xie, H., Ozturk, A., Qiang, B., Song, P., McAleavey, S., Rosenzweig, S., Wang, M., Okamura, Y., McLaughlin, G., Chen, Y., Napolitano, D., Carlson, L., Erpelding, T. & Hall, T. J. Radiological Society of North America/Quantitative Imaging Biomarker Alliance Shear Wave Speed Bias Quantification in Elastic and Viscoelastic Phantoms. *J Ultrasound Med* **40**, 569-581 (2021).

53 Schregel, K., Nazari, N., Nowicki, M. O., Palotai, M., Lawler, S. E., Sinkus, R., Barbone, P. E. & Patz, S. Characterization of glioblastoma in an orthotopic mouse model with magnetic resonance elastography. *NMR Biomed* **31**, e3840 (2018).

54 Eilam, R., Segal, M., Malach, R., Sela, M., Arnon, R. & Aharoni, R. Astrocyte disruption of neurovascular communication is linked to cortical damage in an animal model of multiple sclerosis. *Glia* **66**, 1098-1117 (2018).

55 Svensson, S. F., De Arcos, J., Darwish, O. I., Fraser-Green, J., Storas, T. H., Holm, S., Vik-Mo, E. O., Sinkus, R. & Emblem, K. E. Robustness of MR Elastography in

the Healthy Brain: Repeatability, Reliability, and Effect of Different Reconstruction Methods. *J Magn Reson Imaging* **53**, 1510-1521 (2021).

56 Huang, X., Chafi, H., Matthews, K. L., 2nd, Carmichael, O., Li, T., Miao, Q., Wang, S. & Jia, G. Magnetic resonance elastography of the brain: A study of feasibility and reproducibility using an ergonomic pillow-like passive driver. *Magn Reson Imaging* **59**, 68-76 (2019).

57 Kolipaka, A., Wassenaar, P. A., Cha, S., Marashdeh, W. M., Mo, X., Kalra, P., Gans, B., Raterman, B. & Bourekas, E. Magnetic resonance elastography to estimate brain stiffness: Measurement reproducibility and its estimate in pseudotumor cerebri patients. *Clin Imaging* **51**, 114-122 (2018).

58 Murphy, M. C., Huston, J., 3rd, Jack, C. R., Jr., Glaser, K. J., Senjem, M. L., Chen, J., Manduca, A., Felmlee, J. P. & Ehman, R. L. Measuring the characteristic topography of brain stiffness with magnetic resonance elastography. *PLoS One* **8**, e81668 (2013).

59 Herthum, H., Dempsey, S. C. H., Samani, A., Schrank, F., Shahryari, M., Warmuth, C., Tzschatzsch, H., Braun, J. & Sack, I. Superviscous properties of the in vivo brain at large scales. *Acta Biomater* **121**, 393-404 (2021).

60 Herthum, H., Shahryari, M., Tzschatzsch, H., Schrank, F., Warmuth, C., Gorner, S., Hetzer, S., Neubauer, H., Pfeuffer, J., Braun, J. & Sack, I. Real-Time Multifrequency MR Elastography of the Human Brain Reveals Rapid Changes in Viscoelasticity in Response to the Valsalva Maneuver. *Front Bioeng Biotechnol* **9**, 666456 (2021).

61 Herthum, H., Hetzer, S., Scheel, M., Shahryari, M., Braun, J., Paul, F. & Sack, I. In vivo stiffness of multiple sclerosis lesions is similar to that of normal-appearing white matter. *Acta Biomater* **138**, 410-421 (2022).

62 Dittmann, F., Hirsch, S., Tzschatzsch, H., Guo, J., Braun, J. & Sack, I. In vivo wideband multifrequency MR elastography of the human brain and liver. *Magn Reson Med* **76**, 1116-1126 (2016).

63 Tzschatzsch, H., Guo, J., Dittmann, F., Hirsch, S., Barnhill, E., Johrens, K., Braun, J. & Sack, I. Tomoelastography by multifrequency wave number recovery from time-harmonic propagating shear waves. *Med Image Anal* **30**, 1-10 (2016).

64 Schmidt, R. F., Lang, F. & Heckmann, M. *Physiologie des Menschen*. 31 edn, (Springer-Verlag Berlin Heidelberg, 2011).

65 Ipek-Ugay, S., Tzschatzsch, H., Braun, J., Fischer, T. & Sack, I. Physiologic Reduction of Hepatic Venous Blood Flow by the Valsalva Maneuver Decreases Liver Stiffness. *J Ultrasound Med* **36**, 1305-1311 (2017).

66 Greenfield, J. C., Jr., Rembert, J. C. & Tindall, G. T. Transient changes in cerebral vascular resistance during the Valsalva maneuver in man. *Stroke* **15**, 76-79 (1984).

67 Franze, K., Janmey, P. A. & Guck, J. Mechanics in neuronal development and repair. *Annu Rev Biomed Eng* **15**, 227-251 (2013).

68 Streitberger, K. J., Sack, I., Krefting, D., Pfuller, C., Braun, J., Paul, F. & Wuerfel, J. Brain viscoelasticity alteration in chronic-progressive multiple sclerosis. *PLoS One* **7**, e29888 (2012).

69 Popescu, B. F., Pirko, I. & Lucchinetti, C. F. Pathology of multiple sclerosis: where do we stand? *Continuum (Minneap Minn)* **19**, 901-921 (2013).

70 Papazoglou, S., Hirsch, S., Braun, J. & Sack, I. Multifrequency inversion in magnetic resonance elastography. *Phys Med Biol* **57**, 2329-2346 (2012).

71 Bertalan, G., Guo, J., Tzschatzsch, H., Klein, C., Barnhill, E., Sack, I. & Braun, J. Fast tomoelastography of the mouse brain by multifrequency single-shot MR elastography. *Magn Reson Med* **81**, 2676-2687 (2019).
72 Streitberger, K. J., Lilaj, L., Schrank, F., Braun, J., Hoffmann, K. T., Reiss-Zimmermann, M., Kas, J. A. & Sack, I. How tissue fluidity influences brain tumor progression. *Proc Natl Acad Sci U S A* **117**, 128-134 (2020).
73 Mura, J., Schrank, F. & Sack, I. An analytical solution to the dispersion-by-inversion problem in magnetic resonance elastography. *Magn Reson Med* **84**, 61-71 (2020).
74 Hirsch, S., Klatt, D., Freimann, F., Scheel, M., Braun, J. & Sack, I. In vivo measurement of volumetric strain in the human brain induced by arterial pulsation and harmonic waves. *Magn Reson Med* **70**, 671-683 (2013).
75 Penny, W. D., Friston, K. J., Ashburner, J. T., Kiebel, S. J. & Nichols, T. E. *Statistical parametric mapping: the analysis of functional brain images*. (Elsevier, 2011).
76 Yushkevich, P. A., Piven, J., Hazlett, H. C., Smith, R. G., Ho, S., Gee, J. C. & Gerig, G. User-guided 3D active contour segmentation of anatomical structures: Significantly improved efficiency and reliability. *Neuroimage* **31**, 1116-1128 (2006).
77 MATLAB. *version 9.8.0.1417392 (R2020a)*. (The MathWorks Inc., Natick, Massachusetts, 2010).
78 Herthum, H., Tzschätzsch, H., Meyer, T., Shahryari, M., Stencel, L., Guo, J., Braun, J. & Sack, I. in *ISMRM & SMRT Virtual Conference & Exhibition.* (ed In: Proceedings of the 29st Annual Meeting of ISMRM).
79 Barnhill, E., Nikolova, M., Ariyurek, C., Dittmann, F., Braun, J. & Sack, I. Fast Robust Dejitter and Interslice Discontinuity Removal in MRI Phase Acquisitions: Application to Magnetic Resonance Elastography. *IEEE Trans Med Imaging* **38**, 1578-1587 (2019).
80 Hirsch, S., Guo, J., Reiter, R., Papazoglou, S., Kroencke, T., Braun, J. & Sack, I. MR elastography of the liver and the spleen using a piezoelectric driver, single-shot wave-field acquisition, and multifrequency dual parameter reconstruction. *Magn Reson Med* **71**, 267-277 (2014).
81 Braun, J., Guo, J., Lutzkendorf, R., Stadler, J., Papazoglou, S., Hirsch, S., Sack, I. & Bernarding, J. High-resolution mechanical imaging of the human brain by three-dimensional multifrequency magnetic resonance elastography at 7T. *Neuroimage* **90**, 308-314 (2014).
82 Jiang, X., Asbach, P., Streitberger, K. J., Thomas, A., Hamm, B., Braun, J., Sack, I. & Guo, J. In vivo high-resolution magnetic resonance elastography of the uterine corpus and cervix. *Eur Radiol* **24**, 3025-3033 (2014).
83 Streitberger, K. J., Reiss-Zimmermann, M., Freimann, F. B., Bayerl, S., Guo, J., Arlt, F., Wuerfel, J., Braun, J., Hoffmann, K. T. & Sack, I. High-resolution mechanical imaging of glioblastoma by multifrequency magnetic resonance elastography. *PLoS One* **9**, e110588 (2014).
84 Papazoglou, S., Xu, C., Hamhaber, U., Siebert, E., Bohner, G., Klingebiel, R., Braun, J. & Sack, I. Scatter-based magnetic resonance elastography. *Phys Med Biol* **54**, 2229-2241 (2009).
85 Aster, R. C., Borchers, B. & Thurber, C. H. *Parameter Estimation and Inverse Problems*. (Elsevier, 2013).
86 Shahryari, M., Meyer, T., Warmuth, C., Herthum, H., Bertalan, G., Tzschatzsch, H., Stencel, L., Lukas, S., Lilaj, L., Braun, J. & Sack, I. Reduction of breathing

artifacts in multifrequency magnetic resonance elastography of the abdomen. *Magn Reson Med* **85**, 1962-1973 (2021).

87 Ertl-Wagner, B. B., Lienemann, A., Reith, W. & Reiser, M. F. Demonstration of periventricular brain motion during a Valsalva maneuver: description of technique, evaluation in healthy volunteers and first results in hydrocephalic patients. *Eur Radiol* **11**, 1998-2003 (2001).

88 Barnhill, E., Davies, P. J., Ariyurek, C., Fehlner, A., Braun, J. & Sack, I. Heterogeneous Multifrequency Direct Inversion (HMDI) for magnetic resonance elastography with application to a clinical brain exam. *Med Image Anal* **46**, 180-188 (2018).

89 Donoho, D. L., Johnstone, I. M., Kerkyacharian, G. & Picard, D. Wavelet shrinkage: asymptopia? *Journal of the Royal Statistical Society: Series B (Methodological)* **57**, 301-337 (1995).

90 Barnhill, E., Hollis, L., Sack, I., Braun, J., Hoskins, P. R., Pankaj, P., Brown, C., van Beek, E. J. R. & Roberts, N. Nonlinear multiscale regularisation in MR elastography: Towards fine feature mapping. *Med Image Anal* **35**, 133-145 (2017).

91 Bland, J. M. & Altman, D. G. Applying the right statistics: analyses of measurement studies. *Ultrasound Obstet Gynecol* **22**, 85-93 (2003).

92 Testu, J., McGarry, M. D. J., Dittmann, F., Weaver, J. B., Paulsen, K. D., Sack, I. & Van Houten, E. E. W. Viscoelastic power law parameters of in vivo human brain estimated by MR elastography. *J Mech Behav Biomed Mater* **74**, 333-341 (2017).

93 Bilston, L. E., Liu, Z. & Phan-Thien, N. Linear viscoelastic properties of bovine brain tissue in shear. *Biorheology* **34**, 377-385 (1997).

94 Tully, B. & Ventikos, Y. Coupling poroelasticity and CFD for cerebrospinal fluid hydrodynamics. *IEEE Trans Biomed Eng* **56**, 1644-1651 (2009).

95 Parker, K. J. Are rapid changes in brain elasticity possible? *Phys Med Biol* **62**, 7425-7439 (2017).

96 Kaster, T., Sack, I. & Samani, A. Measurement of the hyperelastic properties of ex vivo brain tissue slices. *J Biomech* **44**, 1158-1163 (2011).

97 McGarry, M., Van Houten, E., Solamen, L., Gordon-Wylie, S., Weaver, J. & Paulsen, K. Uniqueness of poroelastic and viscoelastic nonlinear inversion MR elastography at low frequencies. *Phys Med Biol* **64**, 075006 (2019).

98 Elisberg, E. I. Heart Rate Response to the Valsalva Maneuver as a Test of Circulatory Integrity. *Jama* **186**, 200-205 (1963).

99 Smith, S. A., Salih, M. M. & Littler, W. A. Assessment of beat to beat changes in cardiac output during the Valsalva manoeuvre using electrical bioimpedance cardiography. *Clin Sci (Lond)* **72**, 423-428 (1987).

100 Prabhakar, H., Bithal, P. K., Suri, A., Rath, G. P. & Dash, H. H. Intracranial pressure changes during Valsalva manoeuvre in patients undergoing a neuroendoscopic procedure. *Minim Invasive Neurosurg* **50**, 98-101 (2007).

101 Eckberg, D. L. Parasympathetic cardiovascular control in human disease: a critical review of methods and results. *Am J Physiol* **239**, H581-593 (1980).

102 Looga, R. Reflex cardiovascular responses to lung inflation: a review. *Respir Physiol* **109**, 95-106 (1997).

103 Pstras, L., Thomaseth, K., Waniewski, J., Balzani, I. & Bellavere, F. The Valsalva manoeuvre: physiology and clinical examples. *Acta Physiol (Oxf)* **217**, 103-119 (2016).

104 Hetzer, S., Dittmann, F., Bormann, K., Hirsch, S., Lipp, A., Wang, D. J., Braun, J. & Sack, I. Hypercapnia increases brain viscoelasticity. *J Cereb Blood Flow Metab* **39**, 2445-2455 (2019).

105 Hetzer, S., Hirsch, S., Braun, J., Sack, I. & Weygandt, M. Viscoelasticity of striatal brain areas reflects variations in body mass index of lean to overweight male adults. *Brain Imaging Behav* **14**, 2477-2487 (2020).
106 Mousavi, S. R., Fehlner, A., Streitberger, K. J., Braun, J., Samani, A. & Sack, I. Measurement of in vivo cerebral volumetric strain induced by the Valsalva maneuver. *J Biomech* **47**, 1652-1657 (2014).
107 Urbanski, M. M., Brendel, M. B. & Melendez-Vasquez, C. V. Acute and chronic demyelinated CNS lesions exhibit opposite elastic properties. *Sci Rep* **9**, 999 (2019).
108 Lu, Y. B., Franze, K., Seifert, G., Steinhauser, C., Kirchhoff, F., Wolburg, H., Guck, J., Janmey, P., Wei, E. Q., Kas, J. & Reichenbach, A. Viscoelastic properties of individual glial cells and neurons in the CNS. *Proc Natl Acad Sci U S A* **103**, 17759-17764 (2006).
109 Lu, Y. B., Iandiev, I., Hollborn, M., Korber, N., Ulbricht, E., Hirrlinger, P. G., Pannicke, T., Wei, E. Q., Bringmann, A., Wolburg, H., Wilhelmsson, U., Pekny, M., Wiedemann, P., Reichenbach, A. & Kas, J. A. Reactive glial cells: increased stiffness correlates with increased intermediate filament expression. *FASEB J* **25**, 624-631 (2011).
110 Stoffels, J. M., de Jonge, J. C., Stancic, M., Nomden, A., van Strien, M. E., Ma, D., Siskova, Z., Maier, O., Ffrench-Constant, C., Franklin, R. J., Hoekstra, D., Zhao, C. & Baron, W. Fibronectin aggregation in multiple sclerosis lesions impairs remyelination. *Brain* **136**, 116-131 (2013).
111 Eberle, D., Fodelianaki, G., Kurth, T., Jagielska, A., Möllmert, S., Ulbricht, E., Wagner, K., Taubenberger, A. V., Träber, N. & Escolano, J.-C. Acquired demyelination but not genetic developmental defects in myelination leads to brain tissue stiffness changes. *Brain Multiphysics* **1**, 100019 (2020).
112 Li, M., Guo, J., Hu, P., Jiang, H., Chen, J., Hu, J., Asbach, P., Sack, I. & Li, W. Tomoelastography Based on Multifrequency MR Elastography for Prostate Cancer Detection: Comparison with Multiparametric MRI. *Radiology* **299**, 362-370 (2021).
113 Majeed, W., Kalra, P. & Kolipaka, A. Simultaneous multislice rapid magnetic resonance elastography of the liver. *NMR Biomed* **33**, e4252 (2020).
114 Strasser, J., Haindl, M. T., Stollberger, R., Fazekas, F. & Ropele, S. Magnetic resonance elastography of the human brain using a multiphase DENSE acquisition. *Magn Reson Med* **81**, 3578-3587 (2019).
115 Sui, Y., Arani, A., Trzasko, J. D., Murphy, M. C., Rossman, P. J., Glaser, K. J., McGee, K. P., Manduca, A., Ehman, R. L., Araoz, P. A. & Huston, J., 3rd. TURBINE-MRE: A 3D hybrid radial-Cartesian EPI acquisition for MR elastography. *Magn Reson Med* **85**, 945-952 (2021).
116 Solamen, L. M., Gordon-Wylie, S. W., McGarry, M. D., Weaver, J. B. & Paulsen, K. D. Phantom evaluations of low frequency MR elastography. *Phys Med Biol* **64**, 065010 (2019).
117 Scott, J. M., Arani, A., Manduca, A., McGee, K. P., Trzasko, J. D., Huston, J., 3rd, Ehman, R. L. & Murphy, M. C. Artificial neural networks for magnetic resonance elastography stiffness estimation in inhomogeneous materials. *Med Image Anal* **63**, 101710 (2020).
118 Silva, R. V., Morr, A. S., Mueller, S., Koch, S. P., Boehm-Sturm, P., Rodriguez-Sillke, Y., Kunkel, D., Tzschatzsch, H., Kuhl, A. A., Schnorr, J., Taupitz, M., Sack, I. & Infante-Duarte, C. Contribution of Tissue Inflammation and Blood-Brain Barrier Disruption to Brain Softening in a Mouse Model of Multiple Sclerosis. *Front Neurosci* **15**, 701308 (2021).

Statutory Declaration

“I, Helge Herthum, by personally signing this document in lieu of an oath, hereby affirm that I prepared the submitted dissertation on the topic *Development of multifrequency magnetic resonance elastography for biophysical property quantification of human brain tissue* | *Entwicklung der multifrequenten Magnetresonanz-Elastographie zur Quantifizierung der biophysikalischen Eigenschaften von menschlichem Hirngewebe*, independently and without the support of third parties, and that I used no other sources and aids than those stated.

All parts which are based on the publications or presentations of other authors, either in letter or in spirit, are specified as such in accordance with the citing guidelines. The sections on methodology (in particular regarding practical work, laboratory regulations, statistical processing) and results (in particular regarding figures, charts and tables) are exclusively my responsibility.

Furthermore, I declare that I have correctly marked all of the data, the analyses, and the conclusions generated from data obtained in collaboration with other persons, and that I have correctly marked my own contribution and the contributions of other persons (cf. declaration of contribution). I have correctly marked all texts or parts of texts that were generated in collaboration with other persons.

My contributions to any publications to this dissertation correspond to those stated in the below joint declaration made together with the supervisor. All publications created within the scope of the dissertation comply with the guidelines of the ICMJE (International Committee of Medical Journal Editors; www.icmje.org) on authorship. In addition, I declare that I shall comply with the regulations of Charité – Universitätsmedizin Berlin on ensuring good scientific practice.

I declare that I have not yet submitted this dissertation in identical or similar form to another Faculty.

The significance of this statutory declaration and the consequences of a false statutory declaration under criminal law (Sections 156, 161 of the German Criminal Code) are known to me.”

Date Signature

Declaration of my own contribution to the publications

Helge Herthum contributed the following to the below listed publications:

Publication 1: Herthum, H., Dempsey, S. C. H., Samani, A., Schrank, F., Shahryari, M., Warmuth, C., Tzschätzsch, H., Braun, J. & Sack, I. Superviscous properties of the in vivo brain at large scales. Acta Biomaterialia 121, 393-404 (2021). https://doi.org/10.1016/j.actbio.2020.12.027

Contribution: Prof. Sack and Dr. Braun conceived the original idea to apply ultra-low frequencies in the human brain to extend the frequency bandwidth for dispersion analysis. They also performed the funding acquisition. Prof. Sack, Dr. Tzschätzsch and I conceptualized the simulations and phantom experiments, which I conducted. Prof. Sack, Prof. Samani, Dr. Braun, Dr. Dempsey and I developed the idea to perform ex vivo experiments to further support our in vivo findings. Prof. Samani and Dr. Dempsey carried out the FEM simulations and provided the FEM results shown in Figure 4c. F. Schrank and Dr. Warmuth together with Dr. Tzschätzsch, Dr. Braun, Prof. Sack and others originally developed the imaging sequence[49]. I tailored the sequence (see Table 1 for details) and the experimental setup shown in Figure 1 to allow for optimal assessment of ultra-low frequencies in human brain for wideband dispersion analysis, which resulted in the images shown in Figure 7. I developed the hypothesis that ultra-low frequency actuation in brain tissue might be feasible and might contribute additional information to the brain dispersion function in close collaboration with Prof. Sack, Dr. Braun and Dr. Tzschätzsch. I performed the literature research on human brain properties between static and dynamic deformations of up to 60 Hz vibration frequency. I recruited the volunteers and informed them about the experiment. I acquired the data for in vivo and ex vivo experiments and collected the physiological data given in Table 2. I performed the data analysis in MATLAB with consultation from M. Shahryari, Dr. Tzschätzsch, Dr. Braun and Prof. Sack, which led to the results shown in Figure 11 and Figure 14 and Table 4. I developed brain *k*-MDEV inversion with support of Dr. Tzschätzsch. I wrote and edited the first draft of the manuscript with support from Dr. Braun and Prof. Sack. All co-authors provided critical feedback and helped shape the research and the final manuscript. I created all table and figures shown in the publication, which are the result of my data analysis and statistical tests. I submitted the manuscript and performed necessary editing with valuable contributions from all co-authors.

Publication 2: Herthum, H., Shahryari, M., Tzschätzsch, H., Schrank, F., Warmuth, C., Görner, S., Hetzer, S., Neubauer, H., Pfeuffer, J., Braun, J. & Sack, I. Real-Time Multifrequency MR Elastography of the Human Brain Reveals Rapid Changes in Viscoelasticity in Response to the Valsalva Maneuver. Front Bioeng Biotechnol 9, 666456 (2021). https://doi.org/10.3389/fbioe.2021.666456

Contribution: Prof. Sack, Dr. Braun and I developed the idea to use real-time MRE to track fast viscoelastic changes of human brain tissue during the Valsalva maneuver. I conceived the idea for the additional breath-hold experiments. The real-time sequence was previously published by F. Schrank, Dr. Warmuth, Dr. Pfeuffer and others[50]. Prof. Sack, Dr. Braun, S. Görner and H. Neubauer developed the actuation system and respective control unit. Dr. Warmuth developed the synchronization between sequence and actuation control unit. I tailored the sequence with support of Dr. Warmuth as shown in Figure 8 and adapted the parameters as summarized in Table 1. I performed the literature research on the topic. M. Shahryari gave medical advice on human physiology for data interpretation and performing the Valsalva maneuver. I developed the experimental setup to allow for optimal imaging of fast viscoelastic changes during the conducted experiments. Therefore, I modified the actuation system to use three frequencies simultaneously for harmonic actuation using four pressurized air drivers as shown in Figure 6. Dr. Braun supported me to develop and manufacture the transmission plate to improve subject comfort and reproducibility as shown in Figure 6. I recruited all subjects and informed them about the experiment. I collected the subject characteristics (Table 1) and physiological data during the experiment. I performed all experiments. The acquired wave images are shown in Figure 9 and their respective power spectrum is shown in Figure 12. I edited the post-processing to incorporate three actuation frequencies. I performed the viscoelastic parameter reconstruction and data analysis, which is shown in Figure 15. Additionally, I developed the statistical analysis in R studio to assess group changes visualized in Figure 16 and Figure 19. I programmed the automatic selection of the region of interest and the number of fluid associated voxels as visualized in Figure 15. I wrote and edited the first draft of the manuscript with support from Dr. Braun and Prof. Sack. All co-authors provided critical feedback and helped shape the research and the final manuscript. I created all table and figures shown in the publication. I submitted the manuscript and performed necessary editing with valuable contributions from all co-authors. Prof. Sack and Dr. Braun acquired the funding.

Publication 3: Herthum, H., Hetzer, S., Scheel, M., Shahryari, M., Braun, J., Paul, F. & Sack, I. In vivo stiffness of multiple sclerosis lesions is similar to that of normal-appearing white matter. Acta Biomaterialia 138, 410-421 (2022). https://doi.org/10.1016/j.actbio.2021.10.038

Contribution: Prof. Sack, Prof. Friedemann, Dr. Braun and Dr. Scheel conceived the idea to investigate patients with relapsing-remitting multiple sclerosis (MS) regarding viscoelastic changes in MS lesions and hypothesized disease induced mechanical changes in focal lesions. I tailored the sequence (see Table 1 for details) and the experimental setup to allow for optimal assessment of brain viscoelasticity in MS patients. Recruitment of MS patients and medical information was done by Prof. Friedemann and Dr. Scheel. They also contributed to data curation and assisted in the formal analysis regarding medical characteristics of the disease. The medical technicians S. Pikol and C. Kraut performed the MRI examinations with my support. They also provided medical information on the subjects. Prof. Sack and I performed simulations as shown in Figure 5. I performed all post-processing and data analysis of human brain data. Dr. Hetzer supported me in automatic registration and segmentation of human brain data using anatomical images. I developed 3D brain adapted *k*-MDEV inversion. Figure 10 shows the acquired data in one subject and Figure 17 shows the results in one subject. Dr. Scheel demarcated all MS lesions based on MRE magnitude images and co-registered FLAIR images. I created the surrounding tissue masks and control region masks as shown in Figure 13. I performed all statistical analysis with support of M. Shahryari, who also assisted in interpreting the results regarding medical characteristics. I developed the idea to use control regions to include white matter mechanical heterogeneity in assessment of MS lesion mechanical contrasts with support of Dr. Hetzer. Figure 18 shows the results of the data analysis including control analysis. All co-authors aided in interpreting the results and support the literature research regarding viscoelastic changes induces by MS lesions. I wrote and edited the first draft of the manuscript with support from Prof. Sack. All co-authors provided critical feedback and helped shape the research and the final manuscript. I created all table and figures shown in the publication. I submitted the manuscript and performed necessary editing with valuable contributions from all co-authors. Prof. Sack, Prof. Friedemann, Dr. Braun, Dr. Scheel and Dr. Hetzer contributed to the funding acquisition. I applied for the BIH Quest Award.

_____

Signature, date and stamp of first supervising university professor / lecturer

_____

Signature of doctoral candidate

Publication 1: Superviscous properties of the in vivo brain at large scales

Herthum, H., Dempsey, S. C. H., Samani, A., Schrank, F., Shahryari, M., Warmuth, C., Tzschatzsch, H., Braun, J. & Sack, I. Superviscous properties of the in vivo brain at large scales. Acta Biomater 121, 393-404 (2021). https://doi.org/10.1016/j.actbio.2020.12.027

Journal Data Filtered By: **Selected JCR Year: 2019** Selected Editions: SCIE,SSCI
Selected Categories: **"ENGINEERING, BIOMEDICAL"** Selected Category Scheme: WoS
Gesamtanzahl: 87 Journale

Rank	Full Journal Title	Total Cites	Journal Impact Factor	Eigenfactor Score
1	Nature Biomedical Engineering	3,143	18.952	0.014180
2	Annual Review of Biomedical Engineering	4,698	15.541	0.004880
3	MEDICAL IMAGE ANALYSIS	9,028	11.148	0.017100
4	BIOMATERIALS	108,070	10.317	0.089110
5	Bioactive Materials	859	8.724	0.001650
6	Biofabrication	4,311	8.213	0.007470
7	Advanced Healthcare Materials	11,883	7.367	0.027520
8	Acta Biomaterialia	39,268	7.242	0.050720
9	npj Regenerative Medicine	417	7.021	0.001630
10	IEEE TRANSACTIONS ON MEDICAL IMAGING	21,657	6.685	0.030060
11	Bioengineering & Translational Medicine	595	6.091	0.001660
12	Photoacoustics	715	5.870	0.001760
13	Tissue Engineering Part B-Reviews	3,603	5.724	0.004190
14	IEEE TRANSACTIONS ON BIOMEDICAL ENGINEERING	23,928	4.424	0.021150
15	ARTIFICIAL INTELLIGENCE IN MEDICINE	2,953	4.383	0.003370
16	Journal of Neural Engineering	7,240	4.141	0.011940
17	Bio-Design and Manufacturing	99	4.095	0.000180
18	IEEE Transactions on Biomedical Circuits and Systems	3,534	4.042	0.006530
19	COMPUTERIZED MEDICAL IMAGING AND GRAPHICS	2,656	3.750	0.002940
20	EUROPEAN CELLS & MATERIALS	3,088	3.741	0.003140

Herthum, H., Dempsey, S. C. H., Samani, A., Schrank, F., Shahryari, M., Warmuth, C., Tzschatzsch, H., Braun, J. & Sack, I. Superviscous properties of the in vivo brain at large scales. *Acta Biomater* **121**, 393-404 (2021).
https://doi.org/10.1016/j.actbio.2020.12.027

Herthum, H., Dempsey, S. C. H., Samani, A., Schrank, F., Shahryari, M., Warmuth, C., Tzschatzsch, H., Braun, J. & Sack, I. Superviscous properties of the in vivo brain at large scales. *Acta Biomater* **121**, 393-404 (2021).
https://doi.org/10.1016/j.actbio.2020.12.027

Herthum, H., Dempsey, S. C. H., Samani, A., Schrank, F., Shahryari, M., Warmuth, C., Tzschatzsch, H., Braun, J. & Sack, I. Superviscous properties of the in vivo brain at large scales. *Acta Biomater* **121**, 393-404 (2021).
https://doi.org/10.1016/j.actbio.2020.12.027

Herthum, H., Dempsey, S. C. H., Samani, A., Schrank, F., Shahryari, M., Warmuth, C., Tzschatzsch, H., Braun, J. & Sack, I. Superviscous properties of the in vivo brain at large scales. *Acta Biomater* **121**, 393-404 (2021).
https://doi.org/10.1016/j.actbio.2020.12.027

Herthum, H., Dempsey, S. C. H., Samani, A., Schrank, F., Shahryari, M., Warmuth, C., Tzschatzsch, H., Braun, J. & Sack, I. Superviscous properties of the in vivo brain at large scales. *Acta Biomater* **121**, 393-404 (2021).
https://doi.org/10.1016/j.actbio.2020.12.027

Herthum, H., Dempsey, S. C. H., Samani, A., Schrank, F., Shahryari, M., Warmuth, C., Tzschatzsch, H., Braun, J. & Sack, I. Superviscous properties of the in vivo brain at large scales. *Acta Biomater* **121**, 393-404 (2021).
https://doi.org/10.1016/j.actbio.2020.12.027

Herthum, H., Dempsey, S. C. H., Samani, A., Schrank, F., Shahryari, M., Warmuth, C., Tzschatzsch, H., Braun, J. & Sack, I. Superviscous properties of the in vivo brain at large scales. *Acta Biomater* **121**, 393-404 (2021).
https://doi.org/10.1016/j.actbio.2020.12.027

Herthum, H., Dempsey, S. C. H., Samani, A., Schrank, F., Shahryari, M., Warmuth, C., Tzschatzsch, H., Braun, J. & Sack, I. Superviscous properties of the in vivo brain at large scales. *Acta Biomater* **121**, 393-404 (2021).
https://doi.org/10.1016/j.actbio.2020.12.027

Herthum, H., Dempsey, S. C. H., Samani, A., Schrank, F., Shahryari, M., Warmuth, C., Tzschatzsch, H., Braun, J. & Sack, I. Superviscous properties of the in vivo brain at large scales. *Acta Biomater* **121**, 393-404 (2021).
https://doi.org/10.1016/j.actbio.2020.12.027

Herthum, H., Dempsey, S. C. H., Samani, A., Schrank, F., Shahryari, M., Warmuth, C., Tzschatzsch, H., Braun, J. & Sack, I. Superviscous properties of the in vivo brain at large scales. *Acta Biomater* **121**, 393-404 (2021).
https://doi.org/10.1016/j.actbio.2020.12.027

Herthum, H., Dempsey, S. C. H., Samani, A., Schrank, F., Shahryari, M., Warmuth, C., Tzschatzsch, H., Braun, J. & Sack, I. Superviscous properties of the in vivo brain at large scales. *Acta Biomater* **121**, 393-404 (2021).
https://doi.org/10.1016/j.actbio.2020.12.027

Herthum, H., Dempsey, S. C. H., Samani, A., Schrank, F., Shahryari, M., Warmuth, C., Tzschatzsch, H., Braun, J. & Sack, I. Superviscous properties of the in vivo brain at large scales. *Acta Biomater* **121**, 393-404 (2021).
https://doi.org/10.1016/j.actbio.2020.12.027

Publication 2: Real-Time Multifrequency MR Elastography of the Human Brain Reveals Rapid Changes in Viscoelasticity in Response to the Valsalva Maneuver

Herthum, H., Shahryari, M., Tzschatzsch, H., Schrank, F., Warmuth, C., Gorner, S., Hetzer, S., Neubauer, H., Pfeuffer, J., Braun, J. et al. Real-Time Multifrequency MR Elastography of the Human Brain Reveals Rapid Changes in Viscoelasticity in Response to the Valsalva Maneuver. Front Bioeng Biotechnol 9, 666456 (2021). https://doi.org/10.3389/fbioe.2021.666456

Journal Data Filtered By: **Selected JCR Year: 2019** Selected Editions: SCIE,SSCI Selected Categories: **"MULTIDISCIPLINARY SCIENCES"** Selected Category Scheme: WoS
Gesamtanzahl: 71 Journale

Rank	Full Journal Title	Total Cites	Journal Impact Factor	Eigenfactor Score
1	NATURE	767,209	42.778	1.216730
2	SCIENCE	699,842	41.845	1.022660
3	National Science Review	2,775	16.693	0.009760
4	Science Advances	36,380	13.116	0.172060
5	Nature Human Behaviour	2,457	12.282	0.014190
6	Nature Communications	312,599	12.121	1.259510
7	Science Bulletin	5,172	9.511	0.014150
8	PROCEEDINGS OF THE NATIONAL ACADEMY OF SCIENCES OF THE UNITED STATES OF AMERICA	676,425	9.412	0.931890
9	Journal of Advanced Research	3,564	6.992	0.005470
10	GigaScience	4,068	5.993	0.016410
11	Scientific Data	5,761	5.541	0.028720
12	Research Synthesis Methods	2,572	5.299	0.006440
13	ANNALS OF THE NEW YORK ACADEMY OF SCIENCES	45,596	4.728	0.026370
14	FRACTALS-COMPLEX GEOMETRY PATTERNS AND SCALING IN NATURE AND SOCIETY	2,156	4.536	0.002210
15	iScience	1,410	4.447	0.004140
16	GLOBAL CHALLENGES	481	4.306	0.001440
17	Scientific Reports	386,848	3.998	1.231180
18	JOURNAL OF KING SAUD UNIVERSITY SCIENCE	1,640	3.819	0.002020
19	Journal of the Royal Society Interface	13,762	3.748	0.027670

Rank	Full Journal Title	Total Cites	Journal Impact Factor	Eigenfactor Score
20	Frontiers in Bioengineering and Biotechnology	2,770	3.644	0.007650
21	NPJ Microgravity	346	3.380	0.001210
22	PHILOSOPHICAL TRANSACTIONS OF THE ROYAL SOCIETY A-MATHEMATICAL PHYSICAL AND ENGINEERING SCIENCES	20,609	3.275	0.027840
23	PROCEEDINGS OF THE JAPAN ACADEMY SERIES B-PHYSICAL AND BIOLOGICAL SCIENCES	1,669	3.000	0.001980
24	Advanced Theory and Simulations	432	2.951	0.000700
25	SCIENCE AND ENGINEERING ETHICS	2,129	2.787	0.003760
26	PROCEEDINGS OF THE ROYAL SOCIETY A-MATHEMATICAL PHYSICAL AND ENGINEERING SCIENCES	19,218	2.741	0.018450
27	PLoS One	688,763	2.740	1.388860
28	Royal Society Open Science	7,222	2.647	0.027340
29	Symmetry-Basel	4,888	2.645	0.005390
30	INTERNATIONAL JOURNAL OF BIFURCATION AND CHAOS	7,115	2.469	0.007090
31	COMPLEXITY	4,413	2.462	0.007160
32	PeerJ	17,984	2.379	0.062850
33	MIT Technology Review	871	2.357	0.001810
34	Science of Nature	673	2.090	0.002400
35	SCIENCE PROGRESS	499	1.906	0.000340
36	SOUTH AFRICAN JOURNAL OF SCIENCE	2,631	1.866	0.001800
37	Journal of Taibah University for Science	1,126	1.863	0.001470
38	Journal of Radiation Research and Applied Sciences	1,127	1.804	0.002280

Selected JCR Year: 2019; Selected Categories: "MULTIDISCIPLINARY SCIENCES"

frontiers in Bioengineering and Biotechnology

ORIGINAL RESEARCH
published: 05 May 2021
doi: 10.3389/fbioe.2021.666456

Real-Time Multifrequency MR Elastography of the Human Brain Reveals Rapid Changes in Viscoelasticity in Response to the Valsalva Maneuver

*Helge Herthum[1], Mehrgan Shahryari[2], Heiko Tzschätzsch[2], Felix Schrank[2], Carsten Warmuth[2], Steffen Görner[2], Stefan Hetzer[3], Hennes Neubauer[2], Josef Pfeuffer[4], Jürgen Braun[1] and Ingolf Sack[2]**

[1] Institute of Medical Informatics, Charité – Universitätsmedizin Berlin, Corporate Member of Freie Universität Berlin, Humboldt-Universität zu Berlin, and Berlin Institute of Health, Berlin, Germany, [2] Department of Radiology, Charité – Universitätsmedizin Berlin, Corporate Member of Freie Universität Berlin, Humboldt-Universität zu Berlin, and Berlin Institute of Health, Berlin, Germany, [3] Berlin Center for Advanced Neuroimaging (BCAN), Berlin, Germany, [4] Application Development, Siemens Healthcare GmbH, Erlangen, Germany

OPEN ACCESS

Edited by:
Silvia Budday, University of Erlangen Nuremberg, Germany

Reviewed by:
Mehmet Kurt, Stevens Institute of Technology, United States
Lucy Hiscox, University of Delaware, United States

***Correspondence:**
Ingolf Sack
Ingolf.sack@charite.de

Specialty section:
This article was submitted to Biomechanics, a section of the journal Frontiers in Bioengineering and Biotechnology

Received: *10 February 2021*
Accepted: *07 April 2021*
Published: *05 May 2021*

Citation:
Herthum H, Shahryari M, Tzschätzsch H, Schrank F, Warmuth C, Görner S, Hetzer S, Neubauer H, Pfeuffer J, Braun J and Sack I (2021) Real-Time Multifrequency MR Elastography of the Human Brain Reveals Rapid Changes in Viscoelasticity in Response to the Valsalva Maneuver. Front. Bioeng. Biotechnol. 9:666456. doi: 10.3389/fbioe.2021.666456

Modulation of cerebral blood flow and vascular compliance plays an important role in the regulation of intracranial pressure (ICP) and also influences the viscoelastic properties of brain tissue. Therefore, magnetic resonance elastography (MRE), the gold standard for measuring *in vivo* viscoelasticity of brain tissue, is potentially sensitive to cerebral autoregulation. In this study, we developed a multifrequency MMRE technique that provides serial maps of viscoelasticity at a frame rate of nearly 6 Hz without gating, i.e., in quasi-real time (rt-MMRE). This novel method was used to monitor rapid changes in the viscoelastic properties of the brains of 17 volunteers performing the Valsalva maneuver (VM). rt-MMRE continuously sampled externally induced vibrations comprising three frequencies of 30.03, 30.91, and 31.8 Hz were over 90 s using a steady-state, spiral-readout gradient-echo sequence. Data were processed by multifrequency dual elasto-visco (MDEV) inversion to generate maps of magnitude shear modulus $|G^*|$ (stiffness) and loss angle φ at a frame rate of 5.4 Hz. As controls, the volunteers were examined to study the effects of breath-hold following deep inspiration and breath-hold following expiration. We observed that $|G^*|$ increased while φ decreased due to VM and, less markedly, due to breath-hold in inspiration. Group mean VM values showed an early overshoot of $|G^*|$ 2.4 ± 1.2 s after the onset of the maneuver with peak values of 6.7 ± 4.1% above baseline, followed by a continuous increase in stiffness during VM. A second overshoot of $|G^*|$ occurred 5.5 ± 2.0 s after the end of VM with peak values of 7.4 ± 2.8% above baseline, followed by 25-s sustained recovery until the end of image acquisition. φ was constantly reduced by approximately 2% during the entire VM without noticeable peak values. This is the first report of viscoelasticity changes in brain tissue induced by physiological maneuvers known to alter ICP and detected by clinically applicable rt-MMRE. Our results show that apnea and VM slightly alter brain properties toward a more rigid-solid behavior. Overshooting stiffening reactions seconds after onset and end of VM reveal rapid autoregulatory processes of brain tissue viscoelasticity.

Keywords: real-time multifrequency MRE, cerebral autoregulation, Valsalva maneuver, stiffness, viscoelasticity

INTRODUCTION

A balance of intracranial mechanical properties is of crucial importance for normal brain function (Linninger et al., 2005; Guyton and Hall, 2006; Wagshul et al., 2006; Schmid Daners et al., 2012). Shear modulus and bulk modulus of brain tissue influence cerebrovascular compliance and pulsatility as well as intracranial pressure (ICP) (Giulioni et al., 1988; Greitz et al., 1992; Wagshul et al., 2011; Parker, 2017). While shear modulus can be measured non-invasively by magnetic resonance elastography (MRE) (Hirsch et al., 2017), there is currently no method for direct ICP measurement without an intervention or without making model assumptions (Guyton and Hall, 2006). In complex multiphasic mechanical systems such as the brain, shear modulus and pressure are linked through poroelastic interactions between the fluid and solid spaces (Bilston, 2002; Tully and Ventikos, 2011; Parker, 2014). Thus, it is likely that regulation of ICP, which is one of the most important vital functions of intracranial mechanics, also affects shear viscoelasticity (Perrinez et al., 2009; McGarry et al., 2015; Lilaj et al., 2020). However, this mechanical component of cerebral autoregulation is largely unstudied due to a lack of imaging techniques that can measure cerebral shear modulus *in vivo* with high spatial and temporal resolution.

In the past, cerebral MRE was used to study a wide variety of physiological effects or diseases which affect the *in vivo* shear modulus of brain tissue (Hiscox et al., 2016; Yin et al., 2018). It has been shown that the brain becomes softer during normal aging (Sack et al., 2009; Arani et al., 2015) or pathophysiological processes such as neuroinflammation (Riek et al., 2012; Wang et al., 2019), demyelination (Schregel et al., 2012), or neurodegeneration (Murphy et al., 2012; Munder et al., 2018). In patients, brain softening has been observed in a wide set of neuronal disorders including multiple sclerosis (Wuerfel et al., 2010; Fehlner et al., 2016), Alzheimer's disease (Murphy et al., 2011; Murphy et al., 2016; Gerischer et al., 2018), Parkinson's disease (Lipp et al., 2013, 2018) and normal pressure hydrocephalus (Streitberger et al., 2011; Juge et al., 2016; Murphy et al., 2020). Brain tumors can be either softer or stiffer than normal tissue (Simon et al., 2013; Jamin et al., 2015; Reiss-Zimmermann et al., 2015), while malignant tumors have reduced viscosity (Streitberger et al., 2014; Schregel et al., 2018; Streitberger et al., 2020). A higher stiffness of neural tissue has been associated with increased perfusion pressure (Chatelin et al., 2015; Hetzer et al., 2018, 2019; Bertalan et al., 2019a), ICP (Hatt et al., 2015; Arani et al., 2018), formation of cytotoxic edema in dying animals (Weickenmeier et al., 2018; Bertalan et al., 2020), proliferation of neurons (Klein et al., 2014), neuronal activity (Patz et al., 2019; Lan et al., 2020), and brain maturation (Guo et al., 2019). All of these studies have revealed that brain viscoelasticity can change within minutes (perfusion alterations), weeks (brain maturation in mice), or years (aging, disease progression). However, requiring several minutes of data acquisition, conventional MRE is limited in resolving non-periodic rapid processes such as cerebral autoregulation and ICP alterations which cannot be consistently repeated in volunteers.

Faster techniques including time-harmonic ultrasound elastography (Tzschatzsch et al., 2018; Kreft et al., 2020) and real-time MRE (rt-MRE) (Schrank et al., 2020a) have been introduced recently. While cerebral ultrasound elastography is limited by acoustic windows and cannot generate detailed maps, rt-MRE has the potential to map viscoelasticity with both high spatial resolution and high frame rates. However, feasibility of rt-MRE has as yet only been demonstrated with a small field of view in the lower extremities (Schrank et al., 2020a) and has never been tested in the brain.

Therefore, we here introduce real-time multifrequency MRE (rt-MMRE) for applications in the human brain. Multifrequency extension of rt-MRE was motivated by previous work on multifrequency wavefield inversion promising higher stability and consistency of parameter maps than single-frequency direct inversion (Papazoglou et al., 2012; Hirsch et al., 2014). Moreover, rt-MRE builds on continuous stroboscopic sampling of harmonic vibrations (Schrank et al., 2020b), which can be spectrally decomposed into multifrequency vibrations without extra scan time. As such, rt-MMRE is a natural extension of rt-MRE that yields, at no extra cost, consistent viscoelasticity maps at relatively high frame rates in the order of 6 Hz depending on the repetition time (TR). Since rt-MRE does not require gating and provides multiple viscoelasticity maps per second, we consider this method as a real-time imaging technique.

Using rt-MMRE, we investigate rapid viscoelastic changes during cerebral autoregulation associated with the Valsalva maneuver (VM). The VM is a standard maneuver to voluntarily increase ICP by forceful breathing against the closed airway with abdominal muscle contraction at the same time. VM will be compared with normal breath-holds in inspiration (BH-in) and expiration (BH-ex). To address frequency dispersion and to test the overall consistency of the values measured in association with the VM, the experiment is repeated with a second set of drive frequencies.

Overall, this study has two aims: first, we introduce rt-MMRE based on three simultaneous excitation frequencies to acquire hundreds of viscoelasticity maps within less than 1 min of scan time. Second, we explore cerebral autoregulation with the unprecedentedly high spatiotemporal resolution offered by rt-MMRE.

MATERIALS AND METHODS

Subjects

rt-MMRE was performed in 17 healthy volunteers without a history of neurological diseases (5 females, 36 ± 13 years, age range: 25–81 years, randomly selected). The study was approved by the ethics committee of Charité – Universitätsmedizin Berlin in accordance with the Ethical Principles for Medical Research Involving Human Subjects of the World Medical Association Declaration of Helsinki. Every participant gave written informed consent. Participant characteristics are summarized in **Table 1**. Group mean time curves of heart rate are given in Inline **Supplementary Figure 1**.

Experimental Setup

All experiments were performed in a 3T MRI scanner (Siemens MAGNETOM Prisma, Erlangen) using a 32-channel head coil. Triple-harmonic vibrations in a narrowband frequency regimen

TABLE 1 | Participant characteristics with abbreviations: body mass index (BMI), systolic blood pressure (BPsys), diastolic blood pressure (BPdis), and heart rate (HR).

ID	Sex	Age in years	BMI in kg/m^2	BPsys in mmHg	BPdia in mmHg	HR in bpm
1	f	37	17.5	97	56	69
2	m	29	24.2	130	77	80
3	m	43	23.6	150	88	88
4	m	46	26.3	134	85	62
5	m	34	22.7	124	68	76
6	m	25	20.8	120	70	70
7	m	27	21.6	118	70	64
8	m	30	26.3	126	78	78
9	f	28	20.7	131	85	62
10	m	36	19.9	77	50	54
11	m	26	20.2	121	75	80
12	f	26	20.5	113	60	55
13	f	29	25.7	114	72	73
14	m	51	20.7	130	85	62
15	m	37	26.2	122	72	70
16	f	27	31.6	140	78	90
17	m	81	22.5	125	80	70
Mean (SD)	–	36 (13)	23 (3)	122 (16)	74 (10)	71 (10)

were synchronously induced by four pressurized air drivers attached to a transmission plate and placed underneath the head. The applied frequencies were: 30.03, 30.91, and 31.8 Hz (hereinafter referred to as 31-Hz regimen). The two outmost drivers were operated at the highest frequencies with alternated phases relative to each other. The two inner drivers were operated with the same frequency, again with alternated phases. This way each frequency induced mainly lateral-rotational head motion with minimized compression components. The setup is shown in **Figure 1**.

Vibrations and radiofrequency (RF) excitation started 5 s before data acquisition to ensure establishment of steady states of time-harmonic oscillations and magnetization before start of each experiment. The following rt-MMRE experiments were performed:

i Valsalva maneuver (VM)
ii deep inspiration and breath-hold (BH-in)
iii expiration and breath-hold (BH-ex)

The VM experiment included four consecutive phases: 30 s baseline, 5 s breath-hold in inspiration, 20 s VM and 35 s recovery (total scan time: 90 s). Prior to the experiment, subjects were trained to perform a moderate Valsalva maneuver that could be easily sustained for 20 s to prevent involuntary movement after deep breathing. This experiment was repeated with a second narrowband frequency regimen comprising 40.77, 41.67, and 42.55 Hz (hereinafter referred to as 42-Hz regimen) in order to check the overall consistency of MRE during VM and if there is a noticeable influence of frequency.

BH-in and BH-ex experiments consisted of 30-s baseline acquisition with the volunteer breathing normally, followed by

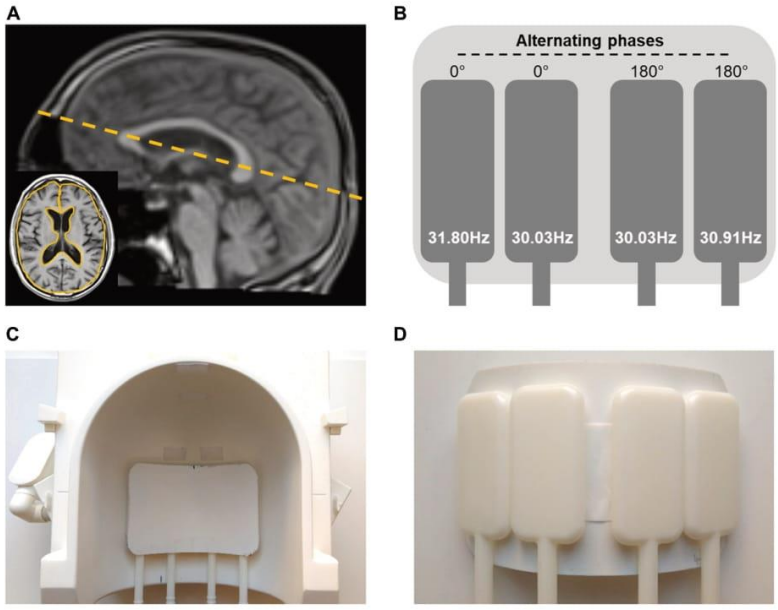

FIGURE 1 | Experimental setup. **(A)** Image slice position (dashed yellow line) and region of interest (ROI) based on anatomical image (yellow solid line in the insert) for rt-MMRE of the brain. **(B)** Diagram of the four flask drivers with vibration frequencies and 180°-phase alterations between the drivers. **(C)** Top view of positioning of actuator setup in the 32-channel head coil. **(D)** Bottom view of driver setup.

a 25-s breath-hold in inspiration or expiration, and a final 35 s recovery phase (total scan time: 90 s).

A resting period of at least 30 s was observed between the experiments. Start and stop commands were given as visual signals to the volunteers. The finger pulse was continuously recorded to track changes in heart rate.

Additionally, anatomical images were acquired using a T1-weighted, turbo-spin echo (TSE) sequence.

rt-MMRE Pulse Sequence

Single-frequency rt-MRE using a 2D single-shot gradient echo MRE pulse sequence with spiral readout was recently introduced for directly mapping skeletal muscle function (Schrank et al., 2020a). For rt-MMRE we used a similar prototype—a single-shot, gradient-echo sequence with dual-density spiral readout, which samples multifrequency vibrations in a stroboscopic fashion as illustrated in **Figure 2**. TR was 62 ms including RF excitation with 20° flip angle, 20 ms TE, 28 ms readout length, signal spoiling and fat suppression. For motion encoding, a single-cycle, bipolar motion-encoding gradient of 17.5-ms duration (57 Hz) and 40-mT/m amplitude was deployed within each TR according to the principle of fractional encoding (Rump et al., 2007). Images were reconstructed using the SPIRiT non-Cartesian parallel imaging technique (Lustig and Pauly, 2010). Three Cartesian motion components were encoded in an interleaved fashion within the series of consecutive TRs, yielding a sequence of 1,458 wave images. Collapsing these three components into a single viscoelasticity map resulted in a total MRE frame rate of 3 × TR = 186 ms, or approximately 5.4 Hz.

Data were acquired in a single transverse image slice with a field of view (FoV) of 192 × 192 mm^2 and 2 × 2 × 5 mm^3 voxel size. The slice was automatically positioned using the localizer-based auto-align function at the level of the basal nuclei along the largest diameter of the lateral ventricles in the sagittal plane as shown in **Figure 1**.

Parameter Reconstruction

The 1,458 raw, complex-valued MR images were smoothed with a Gaussian filter (σ = 0.65 px) and subsequently unwrapped using gradient unwrapping (Hirsch et al., 2017). The three vibration frequencies were decomposed by temporal Fourier transformation. Due to stroboscopic undersampling of vibrations in rt-MMRE, the frequencies appeared at aliased positions in the spectrum (see **Figure 3A**). The frequencies were selected

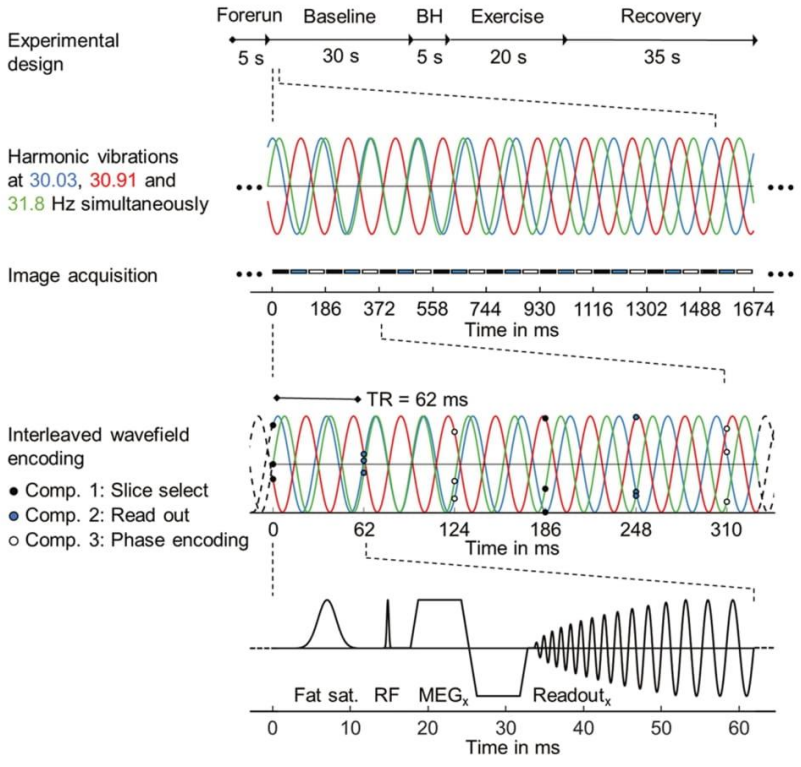

FIGURE 2 | Steady-state gradient echo timing diagram with spiral readout trajectory for single-shot multifrequency real-time MRE. From top to bottom: Experimental design with timing, harmonic vibrations at three frequencies over a period of 9 × 3 TRs with stroboscopic image acquisition below, interleaved wavefield encoding over 2 × 3 TRs, simplified sequence diagram with combined RF and x-gradients to illustrate fat saturation, RF excitation, motion encoding and spiral readout by x-gradients over a single TR period.

by three Gaussian bandpass filters (σ = 0.1 Hz) each of which centered at the expected (aliased) frequency of the fundamental drive frequency. These filters were used for inverse Hilbert transformation to compute complex-valued wave fields (wave images) for each vibration frequency, separately yielding 4,374 (1,458 × 3 vibration frequencies) time-resolved wave images (Schrank et al., 2020b). Nine wave images of three Cartesian field components and three vibration frequencies (see **Figure 3B**) were fed into multifrequency dual elasto-visco inversion (Papazoglou et al., 2012), yielding 486 (4,374/3 encoding components/3 vibration frequencies) consecutive maps of stiffness ($|G^*|$) and loss angle (φ) with 5.4-Hz frame rate over the entire examination time. While $|G^*|$ is a measure of stiffness, φ describes the ratio of elastic to viscous tissue properties indicating fluid properties as explained in Streitberger et al. (2020) $|G^*|$ and φ maps from the beginning and end of the series were discarded within 5-s margins to minimize transient effects introduced by periodic boundary conditions of the Hilbert transform. Consequently, the final observation window was 80 s. All data processing was done in MATLAB (version 2020a). The inversion pipeline is publicly available at https://bioqic$-$apps.charite.de (Meyer et al., 2019). Main results are given in **Table 1**, **Table 2** and in

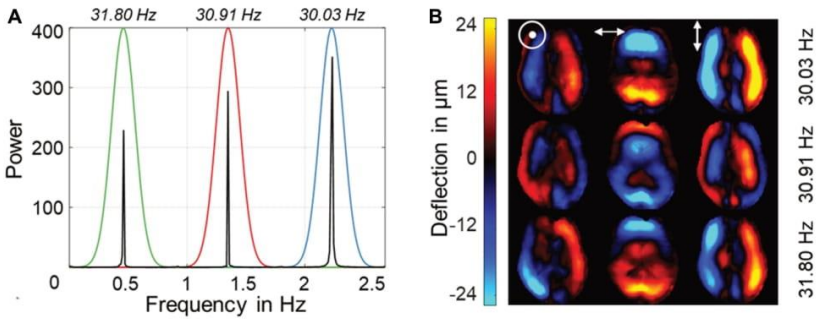

FIGURE 3 | Representative Fourier power spectra with three aliased excitation frequencies for one motion-encoding component above and wave deflections for three encoding components and three vibration frequencies below. **(A)** Power spectra for vibrations at 31-Hz regimen. Color coding indicates the respective vibration frequency with Gaussian bandpass filter used for Hilbert transformation. The frequency axis is scaled from 0 to the Nyquist frequency in Hz, which is determined by the sampling rate of 5.4 Hz. Stroboscopic sampling of multiharmonic vibrations causes all frequencies to be aliased within this limited frequency window. **(B)** Representative wave images after frequency decomposition for the three encoding components using the 31-Hz regimen (30.03, 30.91, 31.8 Hz). [⊙,↔,↕ denote deflections through-plane (head-to-feet), left-right, and up-down (anterior-posterior), respectively].

TABLE 2 | Mean $|G^*|$ (SD) in Pa and mean φ (SD) in rad for each phase and participant in the Valsalva maneuver experiments using the 31-Hz regimen (30.03, 30.91, 31.8 Hz).

ID	Mean $\|G^*\|$ (SD) in Pa				Mean φ (SD) in rad			
	BSL	ESM	LRM	REC	BSL	ESM	LRM	REC
1	1290(6)	1323(17)	1313(5)	12902 (8)	0.841(0.001)	0.831(0.001)	0.849(0.001)	0.840(0.001)
2	1243(16)	1340(17)	1327(10)	1237(11)	0.816(0.007)	0.798(0.003)	0.799(0.003)	0.817(0.001)
3	1351(11)	1415(14)	1409(5)	1336(9)	0.783(0.001)	0.769(0.003)	0.791(0.005)	0.783(0.002)
4	1490(12)	1530(29)	1525(6)	1495(8)	0.87(0.002)	0.853(0.001)	0.87(0.003)	0.868(0.004)
5	1441(6)	1484(24)	1566(14)	1456(10)	0.799(0.003)	0.777(0.005)	0.811(0.009)	0.794(0.004)
6	1502(4)	1536(7)	1609(3)	1511(7)	0.795(0.001)	0.789(0.004)	0.799(0.002)	0.795(0.002)
7	1321(8)	1363(17)	1395(14)	1301(11)	0.818(0.004)	0.815(0.006)	0.83(0.002)	0.829(0.002)
8	1495(6)	1519(20)	1655(8)	1534(16)	0.791(0.002)	0.763(0.004)	0.796(0.008)	0.79(0.004)
9	1515(7)	1620(9)	1617(6)	1549(1)	0.809(0.003)	0.765(0.008)	0.778(0.006)	0.792(0.001)
10	1395(4)	1431(8)	1473(8)	1401(8)	0.78(0.002)	0.776(0.004)	0.779(0.003)	0.778(0.001)
11	1237(12)	1238(11)	1312(15)	1242(9)	0.807(0.004)	0.806(0.003)	0.81(0.005)	0.804(0.001)
12	1312(11)	1350(7)	1416(11)	1310(11)	0.758(0.003)	0.742(0.004)	0.755(0.001)	0.754(0.003)
13	1509(4)	1510(15)	1572(2)	1509(5)	0.809(0.001)	0.807(0.001)	0.804(0.001)	0.8(0.001)
14	1373(8)	1407(14)	1392(3)	1353(4)	0.792(0.002)	0.777(0.002)	0.787(0.002)	0.786(0)
15	1295(8)	1421(35)	1407(13)	1325(15)	0.784(0.005)	0.741(0.018)	0.796(0.002)	0.781(0.003)
16	1356(7)	1391(19)	1422(2)	1330(18)	0.813(0.003)	0.795(0.004)	0.805(0.002)	0.805(0.003)
17	1157(3)	1192(9)	1175(12)	1212(6)	0.733(0.003)	0.725(0.002)	0.722(0.002)	0.728(0.001)
Mean(SD)	1370(106)	1416(108)	1446(126)	1376(108)	0.800(0.030)	0.784(0.032)	0.799(0.032)	0.797(0.031)

BSL, Baseline; ESM, established maneuver; LRM, late response maneuver; REC, recovery.

Supplementary Tables 1a–c. Raw data can be made available upon request without restrictions.

Parameter Analysis and Statistical Tests

For every time frame, | G*| and φ were quantified by averaging values over the same region of interest (ROI). ROIs were manually drawn based on anatomical T1-weighted images, as shown in **Figure 1A**. Furthermore, these ROIs were refined by empirical thresholds of 10 (time-averaged MRE signal magnitude) and of 950 Pa (time-averaged | G*| map) to remove ventricles and larger sulci similar to Shahryari et al. (2020) (see **Figure 4**).

The same ROI was also used to determine magnetization signal-to-noise ratio (SNR) and wave displacement SNR (WSNR) for every time frame. WSNR was derived using the blind noise estimation method proposed by Donoho et al. (1995) as outlined and previously applied to MRE data in Bertalan et al. (2019b) and Schrank et al. (2020a) This noise estimation method is suited for wave image analysis since the spatial frequencies of MRE waves and noise are well separated in the wavelet domain (Selesnick et al., 2005; Barnhill et al., 2017).

To test if multifrequency inversion yields more stable values than single-frequency inversion we determined the coefficient of variation (CV) during the baseline phase prior to VM, BH-in and BH-ex for both | G*| and φ in all volunteers. The same raw data was used, but for the single-frequency inversion only one frequency from the temporal Fourier spectrum was selected.

We further analyzed difference | G*| and φ values relative to mean baseline values given as $\Delta|G^*| = |G^*|_{(t)} - |G^*|_{(baseline)}$ (correspondingly for Δφ) in order to quantify individual parameter changes. In addition, peak viscoelasticity values and their temporal delays relative to the onset and end of VM were identified and tabulated for each volunteer.

Finally, group statistics was applied to the absolute values of | G*| and φ, after temporal averaging over the following experimental phases for each participant:

(1) Baseline (BSL): 2.5–22.5 s
(2) Established maneuver (ESM): 32.5–47.5 s
(3) Late response maneuver (LRM): 52.5–57.5 s
(4) Recovery (REC): 70–80 s.

Of note, these time intervals were given by the aforementioned study design (30-25-35 s. for baseline-breathold/VM-recovery) minus 2.5 s transition phases at the beginnings and ends of these phases including an additional late-response phase. The transition phases were discarded from our analysis in order to minimize transients resulted by the frequency bandpass filter. Also, 5 s BH (25–30 s) and 10 s of post-VM (60–70 s) were considered as transition phases and henceforth not included in our group statistical analysis. All phases are demarcated in **Figure 5**.

To test possible deformations of lateral ventricles due to VM as reported previously (Ertl-Wagner et al., 2001), we applied automatic segmentation of cerebral spinal fluid (CSF) to the temporal averaged MRE magnitude images of the different experimental phases using SPM12 (Penny et al., 2011; see **Figure 4**). CSF probability maps were thresholded at 0.5 to generate logical CSF-associated voxel masks. A linear mixed-effects model with varying intercept was employed. CSF volume was used as dependent variable and the individual phases as independent variables. Participants were assigned as random effect, and *P*-values were calculated using Tukey's *post hoc* test with Bonferroni correction for multiple comparisons. To test for significant changes in | G*| and φ between phases (1)–(4), a linear mixed-effects model with varying intercept was employed. | G*| and φ were used as dependent variables and the individual phases as independent variables. Participants were assigned as random effect, and *P*-values were calculated using Tukey's *post hoc* test with Bonferroni correction for multiple comparisons. This test does not account for inter-individual slope variations of | G*| and φ but analyzes the significance of temporal changes of these parameters. SNR and viscoelastic parameters were correlated using a linear mixed model with | G*| and φ as dependent variables and SNR or WSNR as fixed effects with subjects as random factor. All statistical analysis was done in R (version 3.6.2). Unless otherwise stated, errors are given as standard deviation (SD). Correlations between viscoelastic baseline values as well as individual peak responses and participant characteristics (see **Table 1**) were analyzed

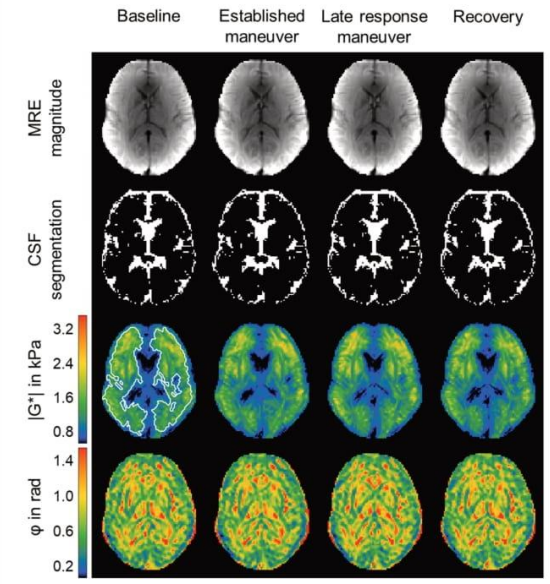

FIGURE 4 | Representative rt-MMRE MRE magnitude, CSF masks, | G*| and φ maps of the *in vivo* human brain. Time-averaged MRE magnitude, derived CSF masks, | G*| and φ maps of one volunteer over the four phases [baseline (BSL), established maneuver (ESM), late response maneuver (LRM) and recovery (REC)] of the VM experiment using the 31-Hz regimen (30.03, 30.91, 31.8 Hz). The number of CSF associated voxels for each phase was BSL: 1079, ESM: 1128, LRM: 1069, REC: 1074. The | G*| maps show slightly elevated values throughout the slice. The region of interest (ROI) is indicated by white lines. The same ROI was used for all phases and for the φ maps as well.

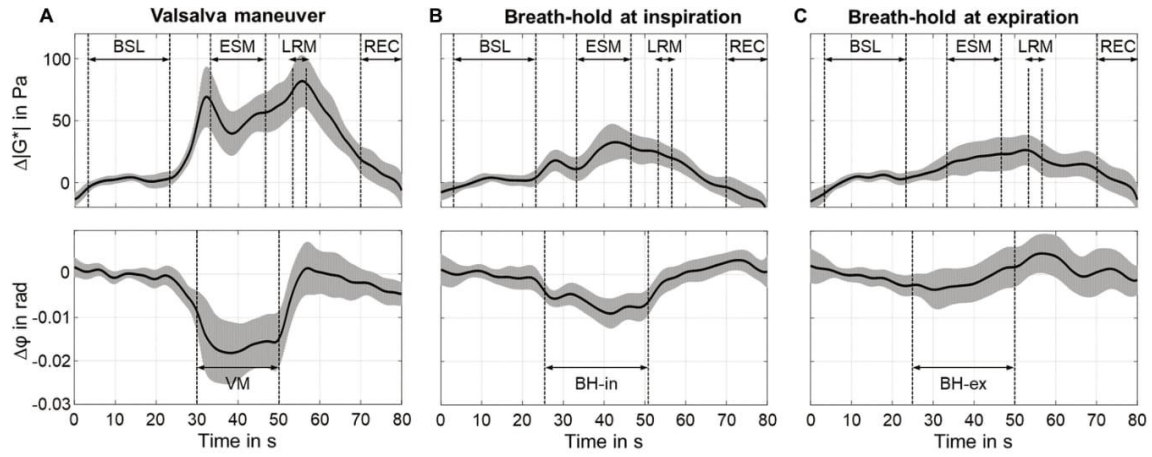

FIGURE 5 | Time courses of group mean values of Δ| G*| (top of subfigures) and Δφ (bottom of subfigures) using the 31-Hz regimen (30.03, 30.91, 31.8 Hz). The gray areas show 95% confidence intervals. For Valsalva maneuver (VM), timing was as follows: breath-hold in inspiration (BH-in) at 25 s, start of VM at 30 s, stop of VM at 50 s. For breath-hold (BH) experiments, timing was as follows: start of BH at 25 s, stop at 50 s. **(A)** Valsalva maneuver (VM). **(B)** Breath-hold in inspiration (BH-in). **(C)** Breath-hold in expiration (BH-ex).

using Pearson's correlation coefficient. *P*-values below 0.05 were considered statistically significant.

RESULTS

Variation in baseline | G*| and φ was smaller when using multifrequency inversion (CV = 0.74%, 0.51%) than single frequencies (CV = 0.99%, 0.77%, $P < 0.001$).

Figure 4 shows representative time-averaged MRE magnitude images, automatically segmented CSF masks, as well as | G*| and φ maps acquired during the four phases of the experiment. A slight increase in | G*| was visible in the late VM response, whereas no response of φ was apparent in individual maps. Group statistics revealed no significant change of CSF-associated voxels between the different states of the maneuver. A descriptive statistic for the individual phases of the VM experiment in the 31-Hz regimen and for each participant is given in **Supplementary Table 2**.

Relative | G*| and φ Changes

Individual analysis of | G*| showed an increase (6.7 ± 4.1%, $P < 0.001$) at approximately 2.4 ± 1.2 s after start of VM and 5.5 ± 2.0 s after end of VM (7.4 ± 2.8%. $P < 0.001$). φ decreased during ESM (−2.1 ± 1.4%, $P < 0.001$). Averaged time courses of Δ| G*| and Δφ are presented in **Figure 5**. An early peak of Δ| G*| showed a difference of 69 ± 50 Pa ($P < 0.001$) from baseline values. After a short drop, Δ| G*| steadily increased during ESM. The second overshoot differed from baseline by 82 ± 42 Pa ($P < 0.01$). Δ| G*| recovered toward baseline values once the volunteers returned to normal breathing. Δφ was constantly decreased during ESM (−0.018 ± 0.012 rad, $P < 0.01$).

The BH-in experiment showed an increase in Δ| G*| after 3.0 ± 1.0 s (18 ± 16 Pa, $P < 0.001$) with a maximum at 17.0 ± 2.0 s after start of BH-in (32 ± 29 Pa, $P < 0.001$). Δφ decreased during ESM (−0.006 ± 0.004 rad, $P < 0.001$) reaching a minimum at 17 ± 2 s after start of BH-in (−0.009 ± 0.007 rad, $P < 0.001$).

The BH-ex experiment showed no clear peak, neither in Δ| G*| nor Δφ. | G*| increased continuously with onset of BH-ex and reached a maximum 2.5 ± 1.5 s after the end of BH-ex (26 ± 23 Pa, $P < 0.001$).

Absolute | G*| and φ Changes

Figure 6 shows boxplots with median effects for different states of the maneuver for | G*| and φ. The significance levels, indicated by asterisks, were determined from a linear mixed model analysis with varying intercept and participants as random effect. For the VM, different individual effect sizes were observed; however, all subjects showed an increase in | G*| and a decrease in φ due to the maneuver. Averaged | G*| values changed between all phases of the experiment (range: 1,370–1,446 Pa) with significance levels indicated in the figure. Averaged φ values changed both from BSL to ESM and again from ESM to LRM (range: 0.784–0.800 rad).

By contrast, | G*| only changed at the start and end of the maneuver in BH-in (range: 1,338–1,372 Pa), whereas φ changed between BSL and ESM as well as between ESM and LRM (range: 0.783–0.792 rad). In the BH-ex experiment, | G*| changed between LRM and REC (range: 1,348–1,371 Pa) while φ changed between ESM and LRM (range: 0.786–0.791 rad).

Results of the second VM experiment performed using the 42-Hz regimen are presented in **Supplementary Material**. No significant differences in viscoelastic responses between the 31-Hz and 42-Hz regimen were observed ($P = 0.24$).

Descriptive statistics of | G*| in Pa and φ in rad for the individual phases of the VM experiment and for each participant are summarized in **Table 2A**. Correspondingly, statistical results

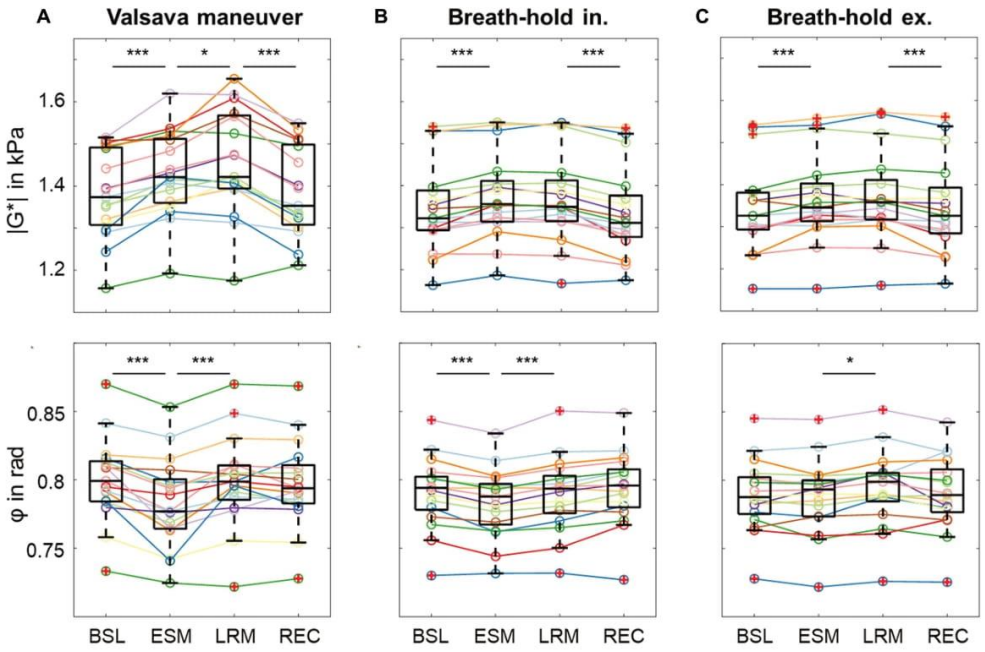

FIGURE 6 | Group values as boxplots for the absolute values of | G*| (top) and φ (bottom) in each phase illustrate the changes in viscoelastic properties induced by the different maneuvers using the 31-Hz regimen for each phase [baseline (BSL), established maneuver (ESM), late response maneuver (LRM), recovery (REC)]. **(A)** Valsalva maneuver (VM). **(B)** Breath-hold in inspiration (BH-in). **(C)** Breath-hold in expiration (BH-ex). Asterisks at the top demarcate significant changes in | G*| and φ which were determined from a linear mixed-effects model with varying intercept. | G*| and φ assigned dependent variables and the individual phases as independent variables. Participants were assigned as random effect, and *P*-values were calculated using Tukey's *post hoc* test with Bonferroni correction for multiple comparisons. (*$P < 0.05$, ***$P < 0.001$).

for the breath-hold and VM experiments performed with the 42-Hz regimen are presented in **Supplementary Tables 1a–c**. Participant characteristics did not correlate with | G*| or φ .

SNR Analysis

Time-averaged SNR and WSNR values did not change significantly across volunteers and over time ($P = 0.43$). Mean SNR was 29 ± 2 dB across all volunteers with minor and insignificant variations of ± 0.5 dB over the course of the experiment. Mean WSNR was 36 ± 2 dB with minor and insignificant variations of ± 1 dB over the course of the experiment. Significant correlation between group mean | G*| and φ was observed (31-Hz regimen: $R = -0.4$, $P < 0.001$, 42-Hz regimen: $R = -0.5$, $P < 0.001$).

DISCUSSION

This paper presents a novel rt-MMRE technique for the *in vivo* measurement of rapid and non-periodic changes in brain viscoelasticity in humans. MRE exploiting stroboscopic sampling of multifrequency harmonic vibrations revealed the viscoelastic response of brain tissue to the Valsalva maneuver. Overall, the extension of rt-MRE to rt-MMRE by simultaneous excitation of multifrequency oscillations has increased the consistency of our measurements without adding scanning time. Probably for this reason, all subjects consistently showed an increase in | G*| and a decrease in φ with VM, resulting in high statistical significance. This basic finding is remarkable, since the VM is known to induce variability by subjective pressure generation. To further discuss our results we start by briefly reviewing the basic effects of VM on cerebral perfusion and ICP.

Physiological Effects of VM on Cerebral Blood Flow, ICP and MRE

In this study, elevation of intrathoracic pressure during VM was induced by deep inspiration following and increased abdominal pressure similar to the maneuver used in Ipek-Ugay et al. (2017). With onset of VM and elevated intrathoracic pressure, arterial blood pressure (ABP) increases (Elisberg, 1963; Smith et al., 1987). Intrathoracic pressure is communicated through the vascular tree into the cranial cavity, leading to a transient increase in ICP and obstruction of venous outflow from the brain with, thus, increased venous pressure (Prabhakar et al., 2007). Reduced venous return to the heart causes ABP to decrease. Hence, cerebral perfusion pressure is reduced, leading to a reduction in cerebral blood flow (CBF). Cerebral autoregulation is a mechanism to maintain constant CBF. For this reason, cerebral autoregulation, after the decrease in CBF, immediately

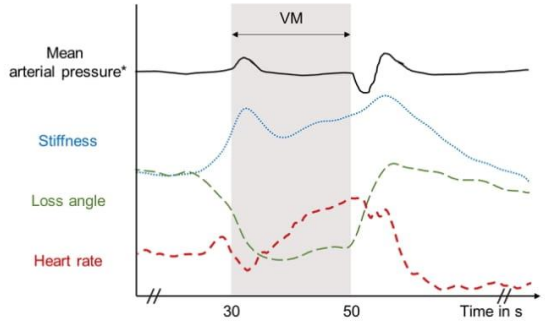

FIGURE 7 | Diagram of average viscoelastic response with typical mean arterial pressure reported by Pstras et al. (2016) and heart rate variations during and after the Valsalva maneuver with inspiration before the maneuver as measured in this study.

responds to reduce vascular resistance by dilating the cerebral arteries in order to facilitate blood flow and maintain stable CBF. At the same time, the heart rate is increased through the baroreflex (Eckberg, 1980; Looga, 1997), which restores normal ABP and accumulation of blood in the brain, since venous return is still diminished. Constant influx of blood with reduced outflow steadily increases ICP. With release of intrathoracic pressure, there is a significant drop of ABP (Stone et al., 1965), and ICP returns to normal. As a result, normal venous return is restored and more blood flows back into the heart, leading to a transient increase in cardiac output and overshoot in ABP. Since vascular resistance is still low, CBF overshoots as well.

The time curves of MRE parameters presented in **Figure 7** suggest that stiffness (| G^*|) correlates with ICP while viscosity-related φ correlates with reduced venous outflow or cerebral perfusion pressure. Perfusion pressure is proportional to CBF normalized by mean vascular diameter (Hetzer et al., 2019) and, thus, decreases upon vasodilation with constant CBF. The ramp-up of | G^*| during the continuing VM phase seems to reflect the increasing heart rate and steady accumulation of blood in the brain, which drives ICP. By contrast, φ remains low throughout the VM phase as if viscous damping in brain tissue is lower when perfusion pressure is reduced. It is an intriguing result that possible ICP changes during VM can be indirectly monitored using rt-MMRE since non-invasive ICP measurement are still an unsolved problem. These findings could help to relate pathologically increased ICP to overall brain stiffness for clinical applications.

In previous work we observed an increase in φ of the brain due to hypercapnia (2% increase) (Hetzer et al., 2019) and arterial pulsation (0.5% increase) (Schrank et al., 2020b). In both studies, there was an increase in CBF with a concomitant increase in perfusion pressure while, as explained above, CBF in VM is, due to cerebral autoregulation, associated with a fairly constant CBF and reduced perfusion pressure. Together, the two rt-MMRE parameters, | G^*| and φ, provide complementary information on the concert of physical parameters involved in ICP autoregulation.

Overall, our baseline parameters of brain viscoelasticity are in good agreement with previously reported values acquired in similar frequency ranges (Hetzer et al., 2018, 2019; Schrank et al., 2020b). We observed no significant differences in the responses of rt-MMRE parameters to VM between the 31 and 42 Hz regimens. This consistency of multifrequency data further validates the technique of rt-MMRE. Furthermore, this observation indicates that the poroelastic response of brain tissue (Lilaj et al., 2020) is similar at 30 and 40 Hz (McGarry et al., 2015). Additional validation of rt-MMRE was obtained by reference experiments performed during breath-holds but without sustained VM. BH-in induced a similar increase in stiffness and decrease in φ as observed during VM. Thus, from an MRE perspective, deep inspiration followed by breath-holding induces effects similar to a *light* VM. Otherwise, no such changes were observed in BH-ex, rendering this maneuver neutral with regard to ICP. Nevertheless, even BH-ex had some small effect on MRE parameters, which, notably, were not correlated to changes in either SNR or WSNR. Also, analysis of CSF volume and ventricle size did not reveal any significant correlation with VM. Previous work by us and others showed that total brain volume increases due to VM by approximately 3% while ventricle volume shrinks by 20% (Ertl-Wagner et al., 2001; Mousavi et al., 2014). In contrast to these studies, our subjects were instructed to perform a moderate Valsalva maneuver to minimize variations in thoracic pressure, muscle strain, and head position.

In our previous work we used ultrasound time-harmonic elastography in a temporal bone window to acquire VM-induced rapid changes in shear wave speed in the temporal lobes of healthy volunteers (Tzschatzsch et al., 2018). Effect sizes in that region were higher (10.8 $\pm$ 2.5%) than revealed by MRE in the full brain tissue slice. It should be noted that the regions covered by our current study do not correspond to the medial temporal gyrus addressed by transtemporal time-harmonic elastography, which makes a direct comparison of effect sizes between the two studies difficult. To analyze the spatial representation of viscoelasticity changes we performed automatic image segmentation using MNI-based registration as well as voxel-wise correlation analysis based on a boxcar function. No significant patterns of viscoelasticity changes could be detected. A more detailed analysis of the spatiotemporal representation of brain viscoelasticity in response to the VM is warranted.

Our study has limitations. The nature of stroboscopic sampling of vibrations by steady-state single-shot acquisitions limited our technique to 2D wave field sampling including three encoding components. This intrinsic limitation of rt-MMRE can currently not be overcome by a multishot variant because VM is a non-periodic event and cannot be repeated with enough temporal reliability. Consequently, our multi-frequency inversion technique was entirely 2D, which may have led to variability due to different slice positioning and oblique intersection of 3D shear wavefields rendering our values as effective viscoelasticity parameters. Nevertheless, our conclusions are drawn from group values in two different frequency regimens. The fact that these values changed with statistical significance

in VM, while neither SNR nor anatomy changed, emphasizes the robustness of the observed MRE effects. Furthermore, our data could be used for suppression of bulk waves based on the in-plane curl component. However, this curl-analysis did not provide more consistent values than our standard MDEV inversion with respect to confidence intervals and statistical power. Finally, 2D brain MRE has a long tradition in disease detection (Wuerfel et al., 2010; Streitberger et al., 2012, 2017, 2020; Lipp et al., 2013, 2018; Fehlner et al., 2016; Gerischer et al., 2018) as well as in the study of brain physiology (Sack et al., 2009, 2011; Schrank et al., 2020b; Herthum et al., 2021). It remains to be determined whether single-frequency 3D MRE can provide similarly consistent clinical and physiological brain data. Instead, as shown herein, unintentional breath-holds may affect 3D MRE due to long scan times. Generally, current MRE techniques cannot account for poroelasticity, heterogeneity, hyperelasticity, anisotropy and temporal variations of brain tissue at the same time. Therefore, to date *all* values measured by brain MRE should be considered as effective parameters.

In summary, we studied the viscoelastic response of the human brain to breathing and the Valsalva maneuver using a novel real-time multifrequency MRE technique. Significant increases in brain stiffness and decreases in φ due to VM were observed with use of two different frequency regimens. Control experiments showed that breath-holds after inhalation induce a response similar to VM but with a smaller effect size. By contrast, breath-holds after exhalation had the smallest effects on cerebral MRE parameters. The time courses we report here provide a reference for the VM response in healthy subjects and might be of value for studying dysfunctional autoregulation as associated with various neurological diseases. rt-MMRE is a fast technique which can provide consistent imaging markers of brain viscoelasticity within a fraction of a minute.

DATA AVAILABILITY STATEMENT

The original contributions presented in the study are included in the article/**Supplementary Material**, further inquiries can be directed to the corresponding author/s.

ETHICS STATEMENT

The studies involving human participants were reviewed and approved by the Ethics committee of Charité – Universitätsmedizin Berlin in accordance with the Ethical Principles for Medical Research Involving Human Subjects of the World Medical Association Declaration of Helsinki. The patients/participants provided their written informed consent to participate in this study.

AUTHOR CONTRIBUTIONS

HH carried out all experiments and contributed to all parts of the manuscript. MS assisted in interpreting the results with regard to physiological changes and statistical analysis. FS, HT, and SH helped to carry out the data processing and verified the results. CW and JP carried out the MRI sequence implementation and image reconstruction. SG and HN contributed to the experimental setup. JB helped supervise the project and constructed the actuation system. IS designed and directed the project and aided in interpreting the results. All authors provided critical feedback and helped shape the research and manuscript.

FUNDING

Funding from the German Research Foundation (GRK 2260 BIOQIC, SFB1340 Matrix in Vision, Neuro-MRE Sa901/17-2) and from the European Union's Horizon 2020 Program (ID 668039, EU FORCE – Imaging the Force of Cancer) is gratefully acknowledged.

SUPPLEMENTARY MATERIAL

The Supplementary Material for this article can be found online at: https://www.frontiersin.org/articles/10.3389/fbioe.2021.666456/full#supplementary-material

REFERENCES

Arani, A., Min, H. K., Fattahi, N., Wetjen, N. M., Trzasko, J. D., Manduca, A., et al. (2018). Acute pressure changes in the brain are correlated with MR elastography stiffness measurements: initial feasibility in an in vivo large animal model. *Magn. Reson. Med.* 79, 1043–1051. doi: 10.1002/mrm.26738

Arani, A., Murphy, M. C., Glaser, K. J., Manduca, A., Lake, D. S., Kruse, S. A., et al. (2015). Measuring the effects of aging and sex on regional brain stiffness with MR elastography in healthy older adults. *Neuroimage* 111, 59–64.

Barnhill, E., Hollis, L., Sack, I., Braun, J., Hoskins, P. R., Pankaj, P., et al. (2017). Nonlinear multiscale regularisation in MR elastography: towards fine feature mapping. *Med. Image Anal.* 35, 133–145. doi: 10.1016/j.media.2016.05.012

Bertalan, G., Boehm-Sturm, P., Schreyer, S., Morr, A. S., Steiner, B., Tzschatzsch, H., et al. (2019a). The influence of body temperature on tissue stiffness, blood perfusion, and water diffusion in the mouse brain. *Acta Biomater.* 96, 412–420. doi: 10.1016/j.actbio.2019.06.034

Bertalan, G., Guo, J., Tzschatzsch, H., Klein, C., Barnhill, E., Sack, I., et al. (2019b). Fast tomoelastography of the mouse brain by multifrequency single-shot MR elastography. *Magn. Reson. Med.* 81, 2676–2687. doi: 10.1002/mrm.27586

Bertalan, G., Klein, C., Schreyer, S., Steiner, B., Kreft, B., Tzschatzsch, H., et al. (2020). Biomechanical properties of the hypoxic and dying brain quantified by magnetic resonance elastography. *Acta Biomater.* 101, 395–402. doi: 10.1016/j.actbio.2019.11.011

Bilston, L. E. (2002). The effect of perfusion on soft tissue mechanical properties: a computational model. *Comput. Methods Biomech. Biomed. Eng.* 5, 283–290. doi: 10.1080/10255840290032658

Chatelin, S., Humbert-Claude, M., Garteiser, P., Ricobaraza, A., Vilgrain, V., Van Beers, B. E., et al. (2015). Cannabinoid receptor activation in the juvenile rat brain results in rapid biomechanical alterations: neurovascular mechanism as a putative confounding factor. *J. Cereb. Blood Flow Metab.* 36:954–964. doi: 10.1177/0271678x15606923

Donoho, D. L., Johnstone, I. M., Kerkyacharian, G., and Picard, D. (1995). Wavelet shrinkage: asymptopia? *J. R. Statist. Soc. Ser. B (Methodological)* 57, 301–337. doi: 10.1111/j.2517-6161.1995.tb02032.x

Eckberg, D. L. (1980). Parasympathetic cardiovascular control in human disease: a critical review of methods and results. *Am. J. Physiol.* 239, H581–H593.

Elisberg, E. I. (1963). Heart rate response to the valsalva maneuver as a test of circulatory integrity. *JAMA* 186, 200–205. doi: 10.1001/jama.1963.03710030040006

Ertl-Wagner, B. B., Lienemann, A., Reith, W., and Reiser, M. F. (2001). Demonstration of periventricular brain motion during a Valsalva maneuver: description of technique, evaluation in healthy volunteers and first results in hydrocephalic patients. *Eur. Radiol.* 11, 1998–2003.

Fehlner, A., Behrens, J. R., Streitberger, K. J., Papazoglou, S., Braun, J., Bellmann-Strobl, J., et al. (2016). Higher-resolution MR elastography reveals early mechanical signatures of neuroinflammation in patients with clinically isolated syndrome. *J. Magn. Reson. Imag.* 44, 51–58.

Gerischer, L. M., Fehlner, A., Kobe, T., Prehn, K., Antonenko, D., Grittner, U., et al. (2018). Combining viscoelasticity, diffusivity and volume of the hippocampus for the diagnosis of Alzheimer's disease based on magnetic resonance imaging. *Neuroimage Clin.* 18, 485–493.

Giulioni, M., Ursino, M., and Alvisi, C. (1988). Correlations among intracranial pulsatility, intracranial hemodynamics, and transcranial doppler wave form: literature review and hypothesis for future studies. *Neurosurgery* 22, 807–812. doi: 10.1227/00006123-198805000-00001

Greitz, D., Wirestam, R., Franck, A., Nordell, B., Thomsen, C. & Stahlberg, F. (1992). Pulsatile brain movement and associated hydrodynamics studied by magnetic resonance phase imaging. the monro-Kellie doctrine revisited. *Neuroradiology* 34, 370–380. doi: 10.1007/bf00596493

Guo, J., Bertalan, G., Meierhofer, D., Klein, C., Schreyer, S., Steiner, B., et al. (2019). Brain maturation is associated with increasing tissue stiffness and decreasing tissue fluidity. *Acta Biomater.* 99, 433–442. doi: 10.1016/j.actbio.2019.08.036

Guyton, A., and Hall, J. (2006). *Textbook of Medical Physiology*, 11th ed. Elsevier Inc., Amsterdam.

Hatt, A., Cheng, S., Tan, K., Sinkus, R., and Bilston, L. E. (2015). MR elastography can be used to measure brain stiffness changes as a result of altered cranial venous drainage during jugular compression. *AJNR Am. J. Neuroradiol.* 36, 1971–1977. doi: 10.3174/ajnr.a4361

Herthum, H., Dempsey, S. C. H., Samani, A., Schrank, F., Shahryari, M., Warmuth, C., et al. (2021). Superviscous properties of the in vivo brain at large scales. *Acta Biomater.* 121, 393–404. doi: 10.1016/j.actbio.2020.12.027

Hetzer, S., Birr, P., Fehlner, A., Hirsch, S., Dittmann, F., Barnhill, E., et al. (2018). Perfusion alters stiffness of deep gray matter. *J. Cereb. Blood Flow Metab.* 38, 116–125.

Hetzer, S., Dittmann, F., Bormann, K., Hirsch, S., Lipp, A., Wang, D. J., et al. (2019). Hypercapnia increases brain viscoelasticity. *J. Cereb. Blood Flow Metab.* 39, 2445–2455.

Hirsch, S., Braun, J., and Sack, I. (2017). *Magnetic Resonance Elastography: Physical Background and Medical Applications*. Wiley-VCH: Weinheim.

Hirsch, S., Guo, J., Reiter, R., Papazoglou, S., Kroencke, T., Braun, J., et al. (2014). MR elastography of the liver and the spleen using a piezoelectric driver, single-shot wave-field acquisition, and multifrequency dual parameter reconstruction. *Magn. Reson. Med.* 71, 267–277. doi: 10.1002/mrm.24674

Hiscox, L. V., Johnson, C. L., Barnhill, E., McGarry, M. D. J., Huston, J., van Beek, E. J. R., et al. (2016). Magnetic resonance elastography (MRE) of the human brain: technique, findings and clinical applications. *Phys. Med. Biol.* 61, R401–R437.

Ipek-Ugay, S., Tzschaetzsch, H., Fischer, T., Braun, J., and Sack, I. (2017). Physiological reduction of hepatic venous blood flow by *Valsalva maneuver* decreases liver stiffness. *J. Ultrasound Med.* 36, 1305–1311.

Jamin, Y., Boult, J. K. R., Li, J., Popov, S., Garteiser, P., Ulloa, J. L., et al. (2015). Exploring the biomechanical properties of brain malignancies and their pathologic determinants in vivo with magnetic resonance elastography. *Cancer Res.* 75, 1216–1224. doi: 10.1158/0008-5472.can-14-1997

Juge, L., Pong, A. C., Bongers, A., Sinkus, R., Bilston, L. E., and Cheng, S. (2016). Changes in rat brain tissue microstructure and stiffness during the development of experimental obstructive hydrocephalus. *PLoS One* 11:e0148652. doi: 10.1371/journal.pone.0148652

Klein, C., Hain, E. G., Braun, J., Riek, K., Mueller, S., Steiner, B., et al. (2014). Enhanced adult neurogenesis increases brain stiffness: in vivo magnetic resonance elastography in a mouse model of dopamine depletion. *PLoS One* 9:e92582. doi: 10.1371/journal.pone.0092582

Kreft, B., Tzschatzsch, H., Schrank, F., Bergs, J., Streitberger, K. J., Waldchen, S., et al. (2020). Time-Resolved response of cerebral stiffness to hypercapnia in humans. *Ultrasound Med. Biol.* 46, 936–943. doi: 10.1016/j.ultrasmedbio.2019.12.019

Lan, P. S., Glaser, K. J., Ehman, R. L., and Glover, G. H. (2020). Imaging brain function with simultaneous BOLD and viscoelasticity contrast: fMRI/fMRE. *Neuroimage* 211:116592. doi: 10.1016/j.neuroimage.2020.116592

Lilaj, L., Fischer, T., Guo, J., Braun, J., Sack, I., and Hirsch, S. (2020). Separation of fluid and solid shear wave fields and quantification of coupling density by magnetic resonance poroelastography. *Magn. Reson. Med.* 85, 1655–1668. doi: 10.1002/mrm.28507

Linninger, A. A., Tsakiris, C., Zhu, D. C., Xenos, M., Roycewicz, P., Danziger, Z., et al. (2005). Pulsatile cerebrospinal fluid dynamics in the human brain. *IEEE Trans. Biomed. Eng.* 52, 557–565. doi: 10.1109/tbme.2005.844021

Lipp, A., Skowronek, C., Fehlner, A., Streitberger, K. J., Braun, J., and Sack, I. (2018). Progressive supranuclear palsy and idiopathic Parkinson's disease are associated with local reduction of in vivo brain viscoelasticity. *Eur. Radiol.* 28, 3347–3354. doi: 10.1007/s00330-017-5269-y

Lipp, A., Trbojevic, R., Paul, F., Fehlner, A., Hirsch, S., Scheel, M., et al. (2013). Cerebral magnetic resonance elastography in supranuclear palsy and idiopathic Parkinson's disease. *Neuroimage Clin.* 3, 381–387. doi: 10.1016/j.nicl.2013.09.006

Looga, R. (1997). Reflex cardiovascular responses to lung inflation: a review. *Respir Physiol.* 109, 95–106. doi: 10.1016/s0034-5687(97)00049-2

Lustig, M., and Pauly, J. M. (2010). SPIRiT: Iterative self-consistent parallel imaging reconstruction from arbitrary k-space. *Magn. Reson. Med.* 64, 457–471. doi: 10.1002/mrm.22428

McGarry, M. D., Johnson, C. L., Sutton, B. P., Georgiadis, J. G., Van Houten, E. E., Pattison, A. J., et al. (2015). Suitability of poroelastic and viscoelastic mechanical models for high and low frequency MR elastography. *Med. Phys.* 42, 947–957. doi: 10.1118/1.4905048

Meyer, T., Tzschätzsch, H., Braun, J., Kalra, P., Kolipaka, A., and Sack, I. (2019). "Online platform for extendable server-based processing of magnetic resonance elastography data," in *Proceedings of the 27st Annual Meeting of ISMRM* (Montreal, QC, Canada), 3966.

Mousavi, S. R., Fehlner, A., Streitberger, K. J., Braun, J., Samani, A., and Sack, I. (2014). Measurement of in vivo cerebral volumetric strain induced by the *Valsalva maneuver*. *J. Biomech.* 47, 1652–1657. doi: 10.1016/j.jbiomech.2014.02.038

Munder, T., Pfeffer, A., Schreyer, S., Guo, J., Braun, J., Sack, I., et al. (2018). MR elastography detection of early viscoelastic response of the murine hippocampus to amyloid β accumulation and neuronal cell loss due to Alzheimer's disease. *J. Magn. Reson. Imag.* 47, 105–114. doi: 10.1002/jmri.25741

Murphy, M. C., Cogswell, P. M., Trzasko, J. D., Manduca, A., Senjem, M. L., Meyer, F. B., et al. (2020). Identification of normal pressure hydrocephalus by disease-specific patterns of brain stiffness and damping ratio. *Invest. Radiol.* 55, 200–208. doi: 10.1097/rli.0000000000000630

Murphy, M. C., Curran, G. L., Glaser, K. J., Rossman, P. J., Huston, J., 3rd, Poduslo, J. F., et al. (2012). Magnetic resonance elastography of the brain in a mouse model of Alzheimer's disease: initial results. *Magn. Reson. Imag.* 30, 535–539. doi: 10.1016/j.mri.2011.12.019

Murphy, M. C., Huston, J., IIIrd., Jack, C. R., Jr., Glaser, K. J., Manduca, A., et al. (2011). Decreased brain stiffness in Alzheimer's disease determined by magnetic resonance elastography. *J. Magn. Reson. Imag.* 34, 494–498. doi: 10.1002/jmri.22707

Murphy, M. C., Jones, D. T., Jack, C. R., Jr., Glaser, K. J., Senjem, M. L., et al. (2016). Regional brain stiffness changes across the Alzheimer's disease spectrum. *Neuroimage Clin.* 10, 283–290. doi: 10.1016/j.nicl.2015.12.007

Papazoglou, S., Hirsch, S., Braun, J., and Sack, I. (2012). Multifrequency inversion in magnetic resonance elastography. *Phys. Med. Biol.* 57, 2329–2346. doi: 10.1088/0031-9155/57/8/2329

Parker, K. J. (2014). A microchannel flow model for soft tissue elasticity. *Phys. Med. Biol.* 59, 4443–4457. doi: 10.1088/0031-9155/59/15/4443

Parker, K. J. (2017). Are rapid changes in brain elasticity possible? *Phys. Med. Biol.* 62, 7425–7439. doi: 10.1088/1361-6560/aa8380

Patz, S., Fovargue, D., Schregel, K., Nazari, N., Palotai, M., Barbone, P. E., et al. (2019). Imaging localized neuronal activity at fast time scales through biomechanics. *Sci. Adv.* 5:eaav3816. doi: 10.1126/sciadv.aav3816

Penny, W. D., Friston, K. J., Ashburner, J. T., Kiebel, S. J., and Nichols, T. E. (2011). *Statistical Parametric Mapping: the Analysis of Functional Brain Images*. Elsevier: Amsterdam.

Perrinez, P. R., Kennedy, F. E., Van Houten, E. E., Weaver, J. B., and Paulsen, K. D. (2009). Modeling of soft poroelastic tissue in time-harmonic MR elastography. *IEEE Trans. Biomed. Eng.* 56, 598–608. doi: 10.1109/tbme.2008.2009928

Prabhakar, H., Bithal, P. K., Suri, A., Rath, G. P., and Dash, H. H. (2007). Intracranial pressure changes during *Valsalva manoeuvre* in patients undergoing a neuroendoscopic procedure. *Minim. Invasive Neurosurg.* 50, 98–101. doi: 10.1055/s-2007-982505

Pstras, L., Thomaseth, K., Waniewski, J., Balzani, I., and Bellavere, F. (2016). The Valsalva manoeuvre: physiology and clinical examples. *Acta Physiol. (Oxf)* 217, 103–119. doi: 10.1111/apha.12639

Reiss-Zimmermann, M., Streitberger, K. J., Sack, I., Braun, J., Arlt, F., Fritzsch, D., et al. (2015). High resolution imaging of viscoelastic properties of intracranial tumours by multi-frequency magnetic resonance elastography. *Clin. Neuroradiol.* 25, 371–378. doi: 10.1007/s00062-014-0311-9

Riek, K., Millward, J. M., Hamann, I., Mueller, S., Pfueller, C. F., Paul, F., et al. (2012). Magnetic resonance elastography reveals altered brain viscoelasticity in experimental autoimmune encephalomyelitis. *Neuroimage Clin.* 1, 81–90. doi: 10.1016/j.nicl.2012.09.003

Rump, J., Klatt, D., Braun, J., Warmuth, C., and Sack, I. (2007). Fractional encoding of harmonic motions in MR elastography. *Magn. Reson. Med.* 57, 388–395. doi: 10.1002/mrm.21152

Sack, I., Beierbach, B., Wuerfel, J., Klatt, D., Hamhaber, U., Papazoglou, S., et al. (2009). The impact of aging and gender on brain viscoelasticity. *Neuroimage* 46, 652–657. doi: 10.1016/j.neuroimage.2009.02.040

Sack, I., Streitberger, K. J., Krefting, D., Paul, F., and Braun, J. (2011). The influence of physiological aging and atrophy on brain viscoelastic properties in humans. *PLos One* 6:e23451. doi: 10.1371/journal.pone.0023451

Schmid Daners, M., Knobloch, V., Soellinger, M., Boesiger, P., Seifert, B., Guzzella, L., et al. (2012). Age-specific characteristics and coupling of cerebral arterial inflow and cerebrospinal fluid dynamics. *PLoS One* 7:e37502. doi: 10.1371/journal.pone.0037502

Schrank, F., Warmuth, C., Gorner, S., Meyer, T., Tzschatzsch, H., Guo, J., et al. (2020a). Real-time MR elastography for viscoelasticity quantification in skeletal muscle during dynamic exercises. *Magn. Reson. Med.* 84, 103–114. doi: 10.1002/mrm.28095

Schrank, F., Warmuth, C., Tzschatzsch, H., Kreft, B., Hirsch, S., Braun, J., et al. (2020b). Cardiac-gated steady-state multifrequency magnetic resonance elastography of the brain: effect of cerebral arterial pulsation on brain viscoelasticity. *J. Cereb. Blood Flow Metab.* 40, 991–1001. doi: 10.1177/0271678x19850936

Schregel, K., Nazari, N., Nowicki, M. O., Palotai, M., Lawler, S. E., Sinkus, R., et al. (2018). Characterization of glioblastoma in an orthotopic mouse model with magnetic resonance elastography. *NMR Biomed.* 31:e3840. doi: 10.1002/nbm.3840

Schregel, K., Wuerfel, E., Garteiser, P., Gemeinhardt, I., Prozorovski, T., Aktas, O., et al. (2012). Demyelination reduces brain parenchymal stiffness quantified in vivo by magnetic resonance elastography. *Proc. Natl. Acad. Sci. U.S.A.* 109, 6650–6655. doi: 10.1073/pnas.1200151109

Selesnick, I. W., Baraniuk, R. G., and Kingsbury, N. G. (2005). The dual-tree complex wavelet transform. *IEEE Signal Process. Magazine* 22, 123–151.

Shahryari, M., Meyer, T., Warmuth, C., Herthum, H., Bertalan, G., Tzschätzsch, H., et al. (2020). Reduction of breathing artifacts in multifrequency magnetic resonance elastography of the abdomen. *Magn. Reson. Med.* 85:1962–1973. doi: 10.1002/mrm.28558

Simon, M., Guo, J., Papazoglou, S., Scholand-Engler, H., Erdmann, C., Melchert, U., et al. (2013). Non-invasive characterization of intracranial tumors by MR-Elastography. *N. J. Phys.* 15:085024. doi: 10.1088/1367-2630/15/8/085024

Smith, S. A., Salih, M. M., and Littler, W. A. (1987). Assessment of beat to beat changes in cardiac output during the *Valsalva manoeuvre* using electrical bioimpedance cardiography. *Clin. Sci. (Lond)* 72, 423–428. doi: 10.1042/cs0720423

Stone, D. J., Lyon, A. F., and Teirstein, A. S. (1965). A reappraisal of the circulatory effects of the *Valsalva maneuver*. *Am. J. Med.* 39, 923–933. doi: 10.1016/0002-9343(65)90114-2

Streitberger, K. J., Fehlner, A., Pache, F., Lacheta, A., Papazoglou, S., Bellmann-Strobl, J., et al. (2017). Multifrequency magnetic resonance elastography of the brain reveals tissue degeneration in neuromyelitis optica spectrum disorder. *Eur. Radiol.* 27, 2206–2215. doi: 10.1007/s00330-016-4561-6

Streitberger, K. J., Lilaj, L., Schrank, F., Braun, J., Hoffmann, K. T., Reiss-Zimmermann, M., et al. (2020). How tissue fluidity influences brain tumor progression. *Proc. Natl. Acad. Sci. U.S.A.* 117, 128–134. doi: 10.1073/pnas.1913511116

Streitberger, K. J., Reiss-Zimmermann, M., Freimann, F. B., Bayerl, S., Guo, J., Arlt, F., et al. (2014). High-resolution mechanical imaging of glioblastoma by multifrequency magnetic resonance elastography. *PLoS One* 9:e110588. doi: 10.1371/journal.pone.0110588

Streitberger, K. J., Sack, I., Krefting, D., Pfuller, C., Braun, J., Paul, F., et al. (2012). Brain viscoelasticity alteration in chronic-progressive multiple sclerosis. *PLoS One* 7:e29888. doi: 10.1371/journal.pone.0029888

Streitberger, K. J., Wiener, E., Hoffmann, J., Freimann, F. B., Klatt, D., Braun, J., et al. (2011). In vivo viscoelastic properties of the brain in normal pressure hydrocephalus. *NMR Biomed.* 24, 385–392.

Tully, B., and Ventikos, Y. (2011). Cerebral water transport using multiple-network poroelastic theory: application to normal pressure hydrocephalus. *J. Fluid Mechan.* 667, 188–215. doi: 10.1017/s0022112010004428

Tzschatzsch, H., Kreft, B., Schrank, F., Bergs, J., Braun, J. & Sack, I. (2018). In vivo time-harmonic ultrasound elastography of the human brain detects acute cerebral stiffness changes induced by intracranial pressure variations. *Sci. Rep.* 8:17888.

Wagshul, M. E., Chen, J. J., Egnor, M. R., McCormack, E. J., and Roche, P. E. (2006). Amplitude and phase of cerebrospinal fluid pulsations: experimental studies and review of the literature. *J. Neurosurg.* 104, 810–819. doi: 10.3171/jns.2006.104.5.810

Wagshul, M. E., Eide, P. K., and Madsen, J. R. (2011). The pulsating brain: a review of experimental and clinical studies of intracranial pulsatility. *Fluids Barriers CNS* 8:5.

Wang, J., Shan, Q., Liu, Y., Yang, H., Kuang, S., He, B., et al. (2019). 3D MR elastography of hepatocellular carcinomas as a potential biomarker for predicting tumor recurrence. *J. Magn. Reson. Imag.* 49, 719–730. doi: 10.1002/jmri.26250

Weickenmeier, J., Kurt, M., Ozkaya, E., de Rooij, R., Ovaert, T. C., Ehman, R. L., et al. (2018). Brain stiffens post mortem. *J. Mech. Behav. Biomed. Mater.* 84, 88–98. doi: 10.1016/j.jmbbm.2018.04.009

Wuerfel, J., Paul, F., Beierbach, B., Hamhaber, U., Klatt, D., Papazoglou, S., et al. (2010). MR-elastography reveals degradation of tissue integrity in multiple sclerosis. *Neuroimage* 49, 2520–2525. doi: 10.1016/j.neuroimage.2009.06.018

Yin, Z., Romano, A. J., Manduca, A., Ehman, R. L. and Huston, J. 3rd. (2018). Stiffness and beyond: what MR elastography can tell us about brain structure and function under physiologic and pathologic conditions. *Top Magn. Reson. Imag.* 27, 305–318. doi: 10.1097/rmr.0000000000000178

Conflict of Interest: JP was employed by company Siemens Healthcare GmbH, Erlangen, Germany.

The remaining authors declare that the research was conducted in the absence of any commercial or financial relationships that could be construed as a potential conflict of interest.

Publication 3: In vivo stiffness of multiple sclerosis lesions is similar to that of normal-appearing white matter

Herthum, H., Hetzer, S., Scheel, M., Shahryari, M., Braun, J., Paul, F. & Sack, I. In vivo stiffness of multiple sclerosis lesions is similar to that of normal-appearing white matter. Acta Biomater 138, 410-421 (2022). https://doi.org/10.1016/j.actbio.2021.10.038

Journal Data Filtered By: **Selected JCR Year: 2019** Selected Editions: SCIE,SSCI
Selected Categories: **"ENGINEERING, BIOMEDICAL"** Selected Category Scheme: WoS
Gesamtanzahl: 87 Journale

Rank	Full Journal Title	Total Cites	Journal Impact Factor	Eigenfactor Score
1	Nature Biomedical Engineering	3,143	18.952	0.014180
2	Annual Review of Biomedical Engineering	4,698	15.541	0.004880
3	MEDICAL IMAGE ANALYSIS	9,028	11.148	0.017100
4	BIOMATERIALS	108,070	10.317	0.089110
5	Bioactive Materials	859	8.724	0.001650
6	Biofabrication	4,311	8.213	0.007470
7	Advanced Healthcare Materials	11,883	7.367	0.027520
8	Acta Biomaterialia	39,268	7.242	0.050720
9	npj Regenerative Medicine	417	7.021	0.001630
10	IEEE TRANSACTIONS ON MEDICAL IMAGING	21,657	6.685	0.030060
11	Bioengineering & Translational Medicine	595	6.091	0.001660
12	Photoacoustics	715	5.870	0.001760
13	Tissue Engineering Part B-Reviews	3,603	5.724	0.004190
14	IEEE TRANSACTIONS ON BIOMEDICAL ENGINEERING	23,928	4.424	0.021150
15	ARTIFICIAL INTELLIGENCE IN MEDICINE	2,953	4.383	0.003370
16	Journal of Neural Engineering	7,240	4.141	0.011940
17	Bio-Design and Manufacturing	99	4.095	0.000180
18	IEEE Transactions on Biomedical Circuits and Systems	3,534	4.042	0.006530
19	COMPUTERIZED MEDICAL IMAGING AND GRAPHICS	2,656	3.750	0.002940
20	EUROPEAN CELLS & MATERIALS	3,088	3.741	0.003140

Herthum, H., Hetzer, S., Scheel, M., Shahryari, M., Braun, J., Paul, F. & Sack, I. In vivo stiffness of multiple sclerosis lesions is similar to that of normal-appearing white matter. *Acta Biomater* **138**, 410-421 (2022).

https://doi.org/10.1016/j.actbio.2021.10.038

Herthum, H., Hetzer, S., Scheel, M., Shahryari, M., Braun, J., Paul, F. & Sack, I. In vivo stiffness of multiple sclerosis lesions is similar to that of normal-appearing white matter. *Acta Biomater* **138**, 410-421 (2022).

https://doi.org/10.1016/j.actbio.2021.10.038

Herthum, H., Hetzer, S., Scheel, M., Shahryari, M., Braun, J., Paul, F. & Sack, I. In vivo stiffness of multiple sclerosis lesions is similar to that of normal-appearing white matter. *Acta Biomater* **138**, 410-421 (2022).

https://doi.org/10.1016/j.actbio.2021.10.038

Herthum, H., Hetzer, S., Scheel, M., Shahryari, M., Braun, J., Paul, F. & Sack, I. In vivo stiffness of multiple sclerosis lesions is similar to that of normal-appearing white matter. *Acta Biomater* **138**, 410-421 (2022).

https://doi.org/10.1016/j.actbio.2021.10.038

Herthum, H., Hetzer, S., Scheel, M., Shahryari, M., Braun, J., Paul, F. & Sack, I. In vivo stiffness of multiple sclerosis lesions is similar to that of normal-appearing white matter. *Acta Biomater* **138**, 410-421 (2022).

https://doi.org/10.1016/j.actbio.2021.10.038

Herthum, H., Hetzer, S., Scheel, M., Shahryari, M., Braun, J., Paul, F. & Sack, I. In vivo stiffness of multiple sclerosis lesions is similar to that of normal-appearing white matter. *Acta Biomater* **138**, 410-421 (2022).

https://doi.org/10.1016/j.actbio.2021.10.038

Herthum, H., Hetzer, S., Scheel, M., Shahryari, M., Braun, J., Paul, F. & Sack, I. In vivo stiffness of multiple sclerosis lesions is similar to that of normal-appearing white matter. *Acta Biomater* **138**, 410-421 (2022).

https://doi.org/10.1016/j.actbio.2021.10.038

Herthum, H., Hetzer, S., Scheel, M., Shahryari, M., Braun, J., Paul, F. & Sack, I. In vivo stiffness of multiple sclerosis lesions is similar to that of normal-appearing white matter. *Acta Biomater* **138**, 410-421 (2022).

https://doi.org/10.1016/j.actbio.2021.10.038

Herthum, H., Hetzer, S., Scheel, M., Shahryari, M., Braun, J., Paul, F. & Sack, I. In vivo stiffness of multiple sclerosis lesions is similar to that of normal-appearing white matter. *Acta Biomater* **138**, 410-421 (2022).

https://doi.org/10.1016/j.actbio.2021.10.038

Herthum, H., Hetzer, S., Scheel, M., Shahryari, M., Braun, J., Paul, F. & Sack, I. In vivo stiffness of multiple sclerosis lesions is similar to that of normal-appearing white matter. *Acta Biomater* **138**, 410-421 (2022).

https://doi.org/10.1016/j.actbio.2021.10.038

Herthum, H., Hetzer, S., Scheel, M., Shahryari, M., Braun, J., Paul, F. & Sack, I. In vivo stiffness of multiple sclerosis lesions is similar to that of normal-appearing white matter. *Acta Biomater* **138**, 410-421 (2022).

https://doi.org/10.1016/j.actbio.2021.10.038

Herthum, H., Hetzer, S., Scheel, M., Shahryari, M., Braun, J., Paul, F. & Sack, I. In vivo stiffness of multiple sclerosis lesions is similar to that of normal-appearing white matter. *Acta Biomater* **138**, 410-421 (2022).

https://doi.org/10.1016/j.actbio.2021.10.038

Curriculum vitae

Mein Lebenslauf wird aus datenschutzrechtlichen Gründen in der elektronischen Version meiner Arbeit nicht veröffentlicht

Mein Lebenslauf wird aus datenschutzrechtlichen Gründen in der elektronischen Version meiner Arbeit nicht veröffentlicht

List of publications

Original publications

Herthum H., Carrillo, H., Osses, A., Uribe, S., Sack, I. & Bertoglio, C. Multiple motion encoding in Phase-Contrast MRI: A general theory and application to elastography imaging. *Medical Image Analysis*, (2022). https://doi.org/10.1016/j.media.2022.102416

Journal impact factor: 8.545 (JCR 2020)

Morr, A. S., **Herthum H.**, Schrank, F., Görner, S., Anders, M. S., Lerchbaumer, M., Müller, H.-P., Fischer, T., Jenderka, K.-V., Hansen, H. H. G., Janmey, P. A., Braun, J., Sack, I. & Tzschatzsch, H. Liquid-Liver Phantom: Mimicking the Viscoelastic Dispersion of Human Liver for Ultrasound- and MRI-Based Elastography. *Investigative Radiology*, (2022). https://doi.org/10.1097/RLI.0000000000000862

Journal impact factor: 6.016 (JCR 2020)

Herthum, H., Hetzer, S., Scheel, M., Shahryari, M., Braun, J., Paul, F. & Sack, I. In vivo stiffness of multiple sclerosis lesions is similar to that of normal-appearing white matter. *Acta Biomater* **138**, 410-421 (2022). https://doi.org/10.1016/j.actbio.2021.10.038

Journal impact factor: 8.947 (JCR 2020)

Jordan, J. E. L., Bertalan, G., Meyer, T., Tzschatzsch, H., Gauert, A., Brame, L., **Herthum, H.**, Safraou, Y., Schroder, L., Braun, J., Hagemann A. I. H. & Sack, I. Microscopic multifrequency MR elastography for mapping viscoelasticity in zebrafish. *Magn Reson Med* **87**, 1435-1445 (2022). https://doi.org/10.1002/mrm.29066

Journal impact factor: 4.668 (JCR 2020)

Lilaj, L., **Herthum, H.**, Meyer, T., Shahryari, M., Bertalan, G., Caiazzo, A., Braun, J., Fischer, T., Hirsch, S. & Sack, I. Inversion-recovery MR elastography of the human brain

for improved stiffness quantification near fluid-solid boundaries. *Magn Reson Med* **86**, 2552-2561 (2021). https://doi.org/10.1002/mrm.28898

Journal impact factor: 4.668 (JCR 2020)

Herthum, H., Shahryari, M., Tzschatzsch, H., Schrank, F., Warmuth, C., Gorner, S., Hetzer, S., Neubauer, H., Pfeuffer, J., Braun, J. & Sack, I. Real-Time Multifrequency MR Elastography of the Human Brain Reveals Rapid Changes in Viscoelasticity in Response to the Valsalva Maneuver. *Front Bioeng Biotechnol* **9**, 666456 (2021). https://doi.org/10.3389/fbioe.2021.666456

Journal impact factor: 5.890 (JCR 2020)

Herthum, H., Dempsey, S. C. H., Samani, A., Schrank, F., Shahryari, M., Warmuth, C., Tzschatzsch, H., Braun, J. & Sack, I. Superviscous properties of the in vivo brain at large scales. *Acta Biomater* **121**, 393-404 (2021). https://doi.org/10.1016/j.actbio.2020.12.027

Journal impact factor: 8.947 (JCR 2020)

Shahryari, M., Meyer, T., Warmuth, C., **Herthum, H.**, Bertalan, G., Tzschatzsch, H., Stencel, L., Lukas, S., Lilaj, L., Braun, J. & Sack, I. Reduction of breathing artifacts in multifrequency magnetic resonance elastography of the abdomen. *Magn Reson Med* **85**, 1962-1973 (2021). https://doi.org/10.1002/mrm.28558

Journal impact factor: 4.668 (JCR 2020)

Acknowledgement

I would like to thank Prof. Ingolf Sack, head of the MRE research group at Charité – Universitätsmedizin Berlin, for supervising my doctoral studies. He contributed significantly to all my research projects, conceived the basic ideas and helped design the final manuscripts. He also provided the necessary funding and supported me from the beginning. His constructive feedback and great motivation were invaluable to my scientific success, and I was able to learn much from our fruitful discussions. Furthermore, I would like to thank for being part of the CRC *"Matrix in Vision"* and for having had the opportunity to conduct my research within the graduate school *BIOQIC* at Charité Universitätsmedizin Berlin. Special thanks to Dr. Judith Bergs as coordinator of *BIOQIC*.

Likewise, I am grateful to Dr. Jürgen Braun for the very pleasant collaboration. He provided me with critical suggestions in all my experiments and always took the time to answer my questions and to advise me in my decisions. Moreover, I would like to thank Dr. Heiko Tzschätzsch and Dr. Carsten Warmuth for their tremendous scientific advice and patient teaching regarding viscoelastic theory and MRI physics, respectively.

Overall, I had a great time in the MRE group at Charité and the daily work was very enjoyable with lively communication and enormous support between all members. Therefore, I would like to thank Anna-Sophie Morr, Bernhard Kreft, Felix Schrank, Gergely Bertalan, Heiko Tzschätzsch, Jakob Jordan, Jing Guo, Joachim Snellings, Karolina Garczynska, Ledia Lilaj, Mahsa Salimi Majd, Matthias Anders, Mehrgan Shahryari, Steffen Görner, Tom Meyer, Yang Yang and Yasmine Safraou. Moreover, many thanks to the external collaborators Stefan Hetzer, Michael Scheel, Cristóbal Bertoglio, Abbas Samani, Stephan Marticorena Garcia, Cynthia Kraut and Susan Pikol for their important contributions and the inspiring conversations. Furthermore, I would like to express my sincere thanks to Ms. Bettina Herwig for her help with the English-language revision of the manuscript.

Finally, I am truly grateful to my family and friends for their support and encouragement during my doctoral studies. Without all the great moments and experiences besides my scientific work, this would not have been possible. Thank you all very much for the amazing years in Berlin and elsewhere.